LUND UNIVERSITY

Ultrafast ytterbium-based laser sources and diagnostics for efficient high-order harmonic generation

Raab, Ann-Kathrin

2024

Document Version:
Publisher's PDF, also known as Version of record

Ultrafast ytterbium-based laser sources and diagnostics for efficient high-order harmonic generation

ANN-KATHRIN RAAB
DEPARTMENT OF PHYSICS | FACULTY OF ENGINEERING, LTH | LUND UNIVERSITY

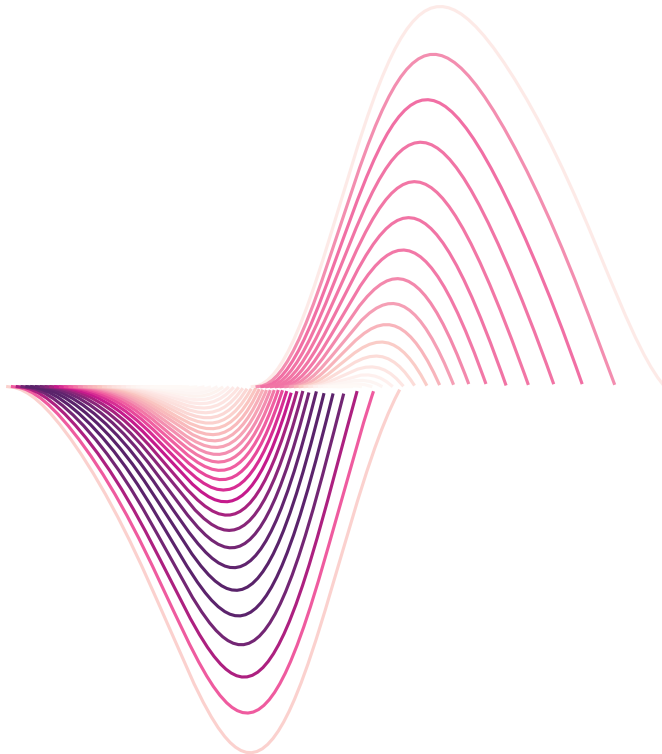

Printed by Media-Tryck, Lund 2024 NORDIC SWAN ECOLABEL 3041 0903

LUND UNIVERSITY

Faculty of Engineering, LTH
Department of Physics

Lund Reports on Atomic Physics, LRAP 606 (2024)
ISBN 978-91-8104-259-7
ISSN 0281-2762

Ultrafast ytterbium-based laser sources and diagnostics for efficient high-order harmonic generation

Ultrafast ytterbium-based laser sources and diagnostics for efficient high-order harmonic generation

by Ann-Kathrin Raab

LUND
UNIVERSITY

Thesis for the degree of PhD in Physics
Thesis advisors: Prof. Anne L'Huillier, Dr. Cord Arnold, Dr. Anne-Lise Viotti
Faculty opponent: Prof. Nirit Dudovich

To be presented, with the permission of the Faculty of Engineering, LTH of Lund University,
for public criticism in Rydberg lecture hall at the Department of Physics
on Friday, the 6th of December 2024 at 09:15.

Organization
LUND UNIVERSITY

Department of Physics
Box 124
SE–221 00 LUND
Sweden

Document name
DOCTORAL DISSERTATION

Date of disputation
2024-12-06

Sponsoring organization

Author(s)
Ann-Kathrin Raab

Title and subtitle
Ultrafast ytterbium-based laser sources and diagnostics for efficient high-order harmonic generation

Abstract
High-order harmonic generation (HHG) supplies extreme ultraviolet (XUV) radiation with attosecond pulse duration for a wide variety of applications from fundamental research to industry. As HHG is a very inefficient process, enhancing the XUV flux is of great interest. Hereby, either the HHG process itself or the laser which is the primary driver of HHG can be optimized.

Currently, the technology is shifting from Titanium:Sapphire (Ti:Sa) to Ytterbium-based (Yb) laser systems as the latter are able to supply much higher average powers, benefiting the XUV flux. However, Yb amplifiers deliver pulse durations much longer than those of Ti:Sa systems.

A significant part of this thesis is dedicated to post-compression of pulses to shorter durations with multi-pass cells (MPCs) demonstrating high efficiencies and scalability to the desired peak power regime. A compact and cost-effective experimental setup that uses thin glass plates as the nonlinear medium compresses 300 fs long pulses from an Yb amplifier with a peak power of 370 MW down to 31 fs. Output peak-powers of > 2.5 GW with a transmission of 87 % and a repetition rate of 200 kHz were achieved, demonstrating a promising perspective for MPCs as HHG drivers.

To accurately judge the quality of ultrashort laser pulses a lot of emphasis was placed on pulse characterization methods, as knowing the exact generation conditions for HHG benefits the understanding of the HHG optimization possibilities immensely. This thesis includes the results from two novel methods developed within the scope of this research work: retrieval of a time-dependent polarization state with the dispersion scan method as well as single-shot carrier-envelope phase measurements via optical Fourier transform.

Optimizing the yield of HHG in a specific XUV spectral range can also be done by tuning the trajectories of the electrons during the HHG process. By combining a turn-key Yb laser with its second harmonic in a waveform synthesizer built for maximum pulse parameter control, two-color HHG was investigated with the emphasis on finding the optimum laser field parameters, consisting of the relative color ratio and phase, to enhance the XUV flux for a specific harmonic order. A simple law based on electron trajectories is derived and experimentally verified, relating the laser field parameters to the yield enhancement of a single harmonic order.

Key words
ultrafast optics, post-compression, pulse characterization, high-order harmonic generation

Classification system and/or index terms (if any)

Supplementary bibliographical information

Language
English

ISSN and key title
0281-2762

ISBN
978-91-8104-259-7 (print)
978-91-8104-260-3 (pdf)

Recipient's notes

Number of pages
197

Price

Security classification

Signature _____ Date 2024-10-11

Ultrafast ytterbium-based laser sources and diagnostics for efficient high-order harmonic generation

by Ann-Kathrin Raab

LUND
UNIVERSITY

A doctoral thesis at a university in Sweden takes either the form of a single, cohesive research study (monograph) or a summary of research papers (compilation thesis), which the doctoral student has written alone or together with one or several other author(s).

In the latter case the thesis consists of two parts. An introductory text puts the research work into context and summarizes the main points of the papers. Then, the research publications themselves are reproduced, together with a description of the individual contributions of the authors. The research papers may either have been already published or are manuscripts at various stages (in press, submitted, or in draft).

Cover illustration front: Dispersion dependent spectral broadening in a bulk multi-pass cell.

Cover illustration back: Electron trajectories in the semi-classical three-step model for a two-color laser driver.

Funding information: The thesis work was financially supported by the Swedish Research Council, the European Research Council, infrastructure support by LTH, the Crafoord Foundation, and the Knut and Alice Wallenberg Foundation.

Faculty of Engineering, LTH, Department of Physics

ISBN: 978-91-8104-259-7 (print)
ISBN: 978-91-8104-260-3 (pdf)
ISSN: 0281-2762
Lund Reports on Atomic Physics, LRAP 606 (2024)

Printed in Sweden by Media-Tryck, Lund University, Lund 2024

'Weird' is part of the job.
- Captain Kathryn Janeway, Star Trek Voyager

Abstract

High-order harmonic generation (HHG) supplies extreme ultraviolet (XUV) radiation with attosecond pulse duration for a wide variety of applications from fundamental research to industry. As HHG is a very inefficient process, enhancing the XUV flux is of great interest. Hereby, either the HHG process itself or the laser which is the primary driver of HHG can be optimized.

Currently, the technology is shifting from Titanium:Sapphire (Ti:Sa) to Ytterbium-based (Yb) laser systems as the latter are able to supply much higher average powers, benefiting the XUV flux. However, Yb amplifiers deliver pulse durations much longer than those of Ti:Sa systems.

A significant part of this thesis is dedicated to post-compression of pulses to shorter durations with multi-pass cells (MPCs) demonstrating high efficiencies and scalability to the desired peak power regime. A compact and cost-effective experimental setup that uses thin glass plates as the nonlinear medium compresses 300 fs long pulses from an Yb amplifier with a peak power of 370 MW down to 31 fs. Output peak-powers of $> 2.5\,\mathrm{GW}$ with a transmission of $87\,\%$ and a repetition rate of $200\,\mathrm{kHz}$ were achieved, demonstrating a promising perspective for MPCs as HHG drivers.

To accurately judge the quality of ultrashort laser pulses a lot of emphasis was placed on pulse characterization methods, as knowing the exact generation conditions for HHG benefits the understanding of the HHG optimization possibilities immensely. This thesis includes the results from two novel methods developed within the scope of this research work: retrieval of a time-dependent polarization state with the dispersion scan method as well as single-shot carrier-envelope phase measurements via optical Fourier transform.

Optimizing the yield of HHG in a specific XUV spectral range can also be done by tuning the trajectories of the electrons during the HHG process. By combining a turn-key Yb laser with its second harmonic in a waveform synthesizer built for maximum pulse parameter control, two-color HHG was investigated with the emphasis on finding the optimum laser field parameters, consisting of the relative color ratio and phase, to enhance the XUV flux for a specific harmonic order. A simple law based on electron trajectories is derived and experimentally verified, relating the laser field parameters to the yield enhancement of a single harmonic order.

Popular Science Summary

Looking at things that no one was able to see before has always been exciting. For the big things, the world was glued to the TVs in awe when first images of the moon landing were broadcasted and pictures taken by telescopes from far away planets, stars, and even galaxies inspired not only a whole science fiction genre, but also made us wonder what else is out there and if we really understand our universe. The universe is incredibly large and slow to our human standards, but since time travel and the famous Warp Drive have not yet been invented, we have to wait for some of the answers to the mysteries of our existence. Maybe a few billion years.

So does this mean that understanding small and fast things is easier? Absolutely not. With our eyes, we can observe a single hair and judge by its damage whether it is time to go to the hairdresser. For everything thinner than hair, we rely on optical microscopes, with those we can observe objects on the picometer scale (0.000000000001 meters. That is extremely small.). On the time scale, our eyes are even weaker. We could not even judge without the tools of early photography whether a horse has all four legs in the air while galloping or not. Today, high-speed cameras allow us to capture flying bullets. But even with the best electronics we cannot measure things faster than a few tens of picoseconds (0.000000000001 seconds, which is extremely short).

But why do we want to look at even smaller and faster things? First of all, because why not. Exploring the limits of knowledge is exciting in itself. Second, it is actually useful and important for further technical and medical advances. Imagine a world where we could watch a movie of a chemical reaction. Not just the end products but looking at the process of how molecules break apart or change their structure or lose one or more electrons. It would certainly be a very short movie in the order of femtoseconds (0.000000000000001 seconds). If we can observe and understand every aspect of it, we might be able to control it at some point, with huge potential benefits for treating diseases or battling climate change. Of course we are not there yet, we can look at molecules, but we are very far away from understanding them.

So how do we look at those ultrashort events, if building a camera does not work so easily? If a camera shutter is not fast enough to not smear out the dynamic events of interest, we simply reduce the exposure time by making the camera flash very short. This works very well with lasers. A laser is light, just as it comes from the sun, but with a few very important differences. Both emit waves, but the laser sends them in only one direction, and not everywhere, which makes it much more intense. Also, it usually consists of very specific colors, which are waves of different wavelengths. If we can control those different wavelengths and how they behave relative to each other

(we call this a "spectral phase"), we can shape a laser light pulse as we like.

After treating the laser light to its desired shape, it is also very important to be able to characterize it. We work with lasers that range from a wavelength of 300 nm to 1100 nm, translating this wavelength to an oscillation period gives a few femtoseconds, so if we want to fully measure this electric field in time, we need the precision to do so. So now that we know how our laser light looks like, we can use it. In my case I do not look at molecules, but I shoot the laser pulse into a cloud of atoms to generate light pulses that are even shorter, with a length of a few hundred attoseconds (0.000000000000001 seconds.)! This process is widely known as high-harmonic generation. Those attosecond pulses are not only short, but their wavelength is also very very small, which makes it super interesting to investigate structures in the few nanometer length scale, for example computer chips.

To generate attosecond pulses with high harmonic generation, lasers based on a material called Titanium:Sapphire were often used in the past. Even though they emit beautifully short laser pulses they are very expensive to operate. Today, laboratories are beginning to switch to lasers based on another material: Ytterbium. While these lasers are much cheaper and more powerful, the emitted pulses are much longer.

In summary, my work is located right in-between laser development and applications. I used a Ytterbium laser and shortened its light pulses and performed research on the art of characterizing those electric fields. Using the knowledge I gained from there, I moved on to high-harmonic generation, with the goal to generate as powerful high harmonics as possible.

Populärvetenskaplig sammanfattning

Att se saker som ingen tidigare har kunnat se har alltid varit spännande. När det gäller stora saker, klistrade världen sig framför TV-apparaterna i förundran när de första bilderna av månlandningen sändes, och bilder tagna av teleskop från avlägsna planeter, stjärnor och till och med galaxer inspirerade inte bara en hel science fiction-genre, utan fick oss också att undra vad mer som finns där ute och om vi verkligen förstår vårt universum. Universum är otroligt stort och långsamt enligt våra mänskliga mått, men eftersom tidsresor och den berömda Warp Drive ännu inte har uppfunnits, måste vi vänta på några av svaren på våra existentiella mysterier. Kanske flera miljarder år.

Så, betyder det att det är lättare att förstå små och snabba saker? Absolut inte. Med våra ögon kan vi observera ett enda hårstrå och avgöra utifrån dess skick om det är dags att gå till frisören. För allt som är tunnare än ett hårstrå är vi beroende av mikroskop, och med dem kan vi observera objekt på picometerskala (0,000000000001 meter. Det är extremt litet). På tidsskalan är våra ögon ännu svagare. Vi kunde inte ens avgöra, utan de tidiga fotografiverktygen, om en häst hade alla fyra benen i luften medan den galopperade eller inte. Idag tillåter höghastighetskameror oss att fånga flygande kulor på bild. Men även med den bästa elektroniken kan vi inte mäta saker snabbare än några tiotal picosekunder (0,000000000001 sekunder, vilket är extremt kort).

Men varför vill vi titta på ännu mindre och snabbare saker? För det första, varför inte? Att utforska kunskapens gränser är spännande i sig. För det andra är det faktiskt användbart och viktigt för ytterligare tekniska och medicinska framsteg. Tänk dig en värld där vi kunde se en film av en kemisk reaktion. Inte bara slutprodukterna, utan att titta på processen hur molekyler bryts sönder eller ändrar sin struktur eller förlorar en eller flera elektroner. Det skulle säkert vara en väldigt kort film, i storleksordningen femtosekunder (0,000000000000001 sekunder). Om vi kan observera och förstå varje aspekt av det, så kan vi kanske kontrollera det vid något tillfälle. Det skulle ge enorma fördelar för behandling av sjukdomar eller bekämpning av klimatförändringar. Idag kan vi titta på filmer av molekyler, men vi är långt ifrån att förstå dem.

Så hur tittar vi på dessa ultrakorta händelser, om det inte är så enkelt att bygga en kamera? Om en kameraslutare inte är tillräckligt snabb för att inte sudda ut de dynamiska händelserna av intresse, förkortar vi helt enkelt exponeringstiden genom att göra kamerans blixt väldigt kort. Detta fungerar mycket bra med lasrar. En laser är ljus, precis som det som kommer från solen, men med några mycket viktiga skillnader. Båda sänder ut vågor, men lasern skickar dem i bara en riktning, och inte överallt, vilket gör den mycket mer intensiv. Dessutom består den vanligtvis av mycket specifika färger, som är vågor med olika våglängder. Om vi kan kontrollera dessa olika

våglängder och hur de beter sig i förhållande till varandra (vi kallar detta spektral faskontroll"), kan vi forma en laserljuspuls som vi vill.

Efter att ha behandlat laserljuset till sin önskade form är det också mycket viktigt att kunna karaktärisera den. Vi arbetar med lasrar som har våglängd från 300 nm till 1100 nm. Om man omvandlar dessa våglängder till en svängningsperiod får man några femtosekunder. Om vi vill mäta tiden för detta elektriska fält , behöver vi precision för att göra det. När vi vet hur vårt laserljus ser ut, kan vi använda det. I mitt fall tittar jag inte på molekyler, utan jag skjuter laserpulsen in i ett moln av atomer för att generera ljuspulser som är ännu kortare, med en längd på några hundra attosekunder (0,000000000000001 sekunder)! Denna process är allmänt känd som hög övertons generering. Dessa attosekundpulser är inte bara korta, utan deras våglängd är också mycket liten, vilket gör dem superanvändbara för att undersöka strukturer på några nanometer storlek, till exempel datorkretsar.

För att generera attosekundpulser med hög övertons generering användes ofta lasrar baserade på ett material som heter Titan:Safir. Även om de avger fantastiskt korta laserpulser är de mycket dyra att använda. Idag börjar laboratorier övergå till lasrar baserade på ett annat material: Ytterbium. Även om dessa lasrar är mycket billigare och kraftfullare, är de avsända pulserna mycket längre.

Sammanfattningsvis befinner sig mitt arbete mitt emellan laserutveckling och tillämpningar. Jag använde en Ytterbium-laser och förkortade dess ljuspulser och gjorde även ytterligare forskning på konsten att karaktärisera dessa elektriska fält. Med den kunskap jag fick därifrån gick jag vidare till hög-harmonisk generering, där mitt huvudmål är att hitta ett recept för att få så starka övertoner som möjligt.

List of publications

This thesis is based on the following publications, referred to by their Roman numerals:

I **Multi-gigawatt peak power post-compression in a bulk multi-pass cell at a high repetition rate**
A.-K. Raab, M. Seidel, C. Guo, I. Sytcevich, G. Arisholm, A. L'Huillier, C. L. Arnold, and A.-L. Viotti
Optics Letters, 2022, 47 (19), pp. 5084-5087

II **Measurement of ultrashort laser pulses with a time-dependent polarization state using the d-scan technique**
D. Diaz Rivas, **A.-K. Raab**, C. Guo, A.-L. Viotti, I. Sytcevich, A. L'Huillier, and C. L. Arnold
Journal of Physics: Photonics, 2024, 6 015003

III **Single-shot, high-repetition rate carrier-envelope-phase detection of ultrashort laser pulses**
C. Guo, M. Miranda, **A.-K. Raab**, A.-L. Viotti, P. T. Guerreiro, R. Romero, H. Crespo, A. L'Huillier, and C. L. Arnold
Optics Letters, 2023, 48 (20), pp. 5431-5434

IV **Highly versatile, two-color setup for high-order harmonic generation using spatial light modulators**
A.-K. Raab, M. Schmoll, E. R. Simpson, M. Redon, Y. Fang, C. Guo, A.-L.Viotti, C. L. Arnold, A. L'Huillier, and J. Mauritsson
Review of Scientific Instruments, 2024, 95 (7): 073002

V **XUV yield optimization of two-color high-order harmonic generation in gases**
A.-K. Raab, M. Redon, S. Roscam Abbing, Y. Fang, C. Guo, P. Smorenburg, J. Mauritsson, A.-L. Viotti, A. L'Huillier, and C. L. Arnold
submitted, 2024

VI **Compact, folded multi-pass cells for energy scaling of post-compression**

A. Schönberg, S. Rajhans, E. Escoto, N. Khodakovskiy, V. Hariton, K. Põder, B. Farace, **A.-K. Raab**, S. Westerberg, M. Merdanov, A.-L. Viotti, C. L. Arnold, W. P. Leemans, I. Hartl, and C. M. Heyl
submitted, 2024

All papers are reproduced with permission of their respective publishers.

Contents

Part I

Thesis

Chapter 1

Introduction

1.1 High-order harmonic generation and its applications

When studying the ionization of noble gases with powerful lasers during the late 1980s, researchers did not only find the expected electrons but also, to their great surprise, many odd-order high harmonics of the driving laser frequency [1]. The intensities of these high-order harmonics in the extreme-ultraviolet (XUV) spectral region are comparable, defying the beliefs of the expected physics at that time. It was suggested very quickly afterwards that the resulting very broad spectrum, centered in the XUV, could be used to generate pulses with attosecond duration (1×10^{-18} s) [2]. Many years and many advances in theoretical understanding and laser development later, the first experimental observations of attosecond pulses by high-order harmonic generation (HHG) were shown [3, 4].

Physics with attosecond resolution, which is the time scale on which electrons move, enabled many fascinating studies. But not only the temporal aspects are interesting. Due to its short wavelength, HHG can be used to study the spatial properties of structures within the same length scale. Since modern HHG systems can be very compact and fit on a single laboratory table, this became a very interesting opportunity for industrial applications, e.g. in the semiconductor industry [5, 6].

Still, HHG is a very inefficient process, compared to the laser powers that are required to generate it, on the order of 10^{-5} to 10^{-7} [7]. It can be intuitively explained by the semi-classical three-step model [8], sketched in Fig. 1.1. An intense laser pulse can enable electrons to tunnel into the continuum (step 1). The strong electric field of the laser further accelerates the electron away from its parent atom (step 2). When the electric field changes its sign, the electron is accelerated back to the atom where

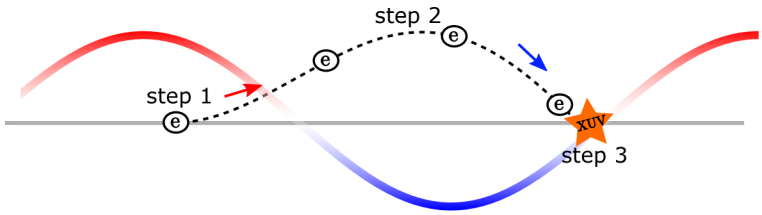

Figure 1.1: Illustration of the semi-classical three-step model for one electron. The trajectory the electron takes is illustrated by the dashed line, the electric field is displayed in red (positive) and blue (negative).

it may eventually recombine (step 3), converting its acquired kinetic energy into an XUV photon. The understanding and manipulation of the HHG process itself is inevitable intertwined with laser development and characterization, as lasers are the primary drivers of HHG.

The maximum XUV photon energy that can be reached with HHG increases quadratically with the central wavelength of the laser being used because an electron has more time to acquire kinetic energy [9]. However, because of the longer time in the continuum, the probability of return is significantly lower due to the spread of the electron wave packet, therefore greatly reducing the efficiency of the whole process further [10]. During the last decade, this has sparked a large interest in the development of high repetition-rate long-wavelength systems that also deliver high average power [11].

Another route to increase the XUV yield is manipulating the electron trajectories during step 2 of the three-step model. This can be done by changing the shape of the electric field, for instance, by combining different frequencies. HHG with a fundamental and its third harmonic together was first demonstrated in 1994, where Watanabe et al. observed a large increase in harmonic yield compared to only using the fundamental [12]. In fact, it was predicted that the optimum electric field shape to maximize the HHG yield can be achieved by such a multi-color synthesis [13]. HHG with multiple colors can be used not only for enhancing the flux but also to learn more about the process itself. For example, by having precise control over the amplitude and phase of the different colors, the exact dynamics of birth and recollision of the electrons could be resolved and investigated [14–17].

1.2 Motivation of this thesis

The workhorse for many HHG studies has been the Titanium:Sapphire (Ti:Sa) laser [18] due to its short pulse duration towards the few electric field cycle regime and high peak power. However, amplifying the output of a Ti:Sa oscillator to reach the laser intensities that are needed is a very inefficient process. Due to the large difference

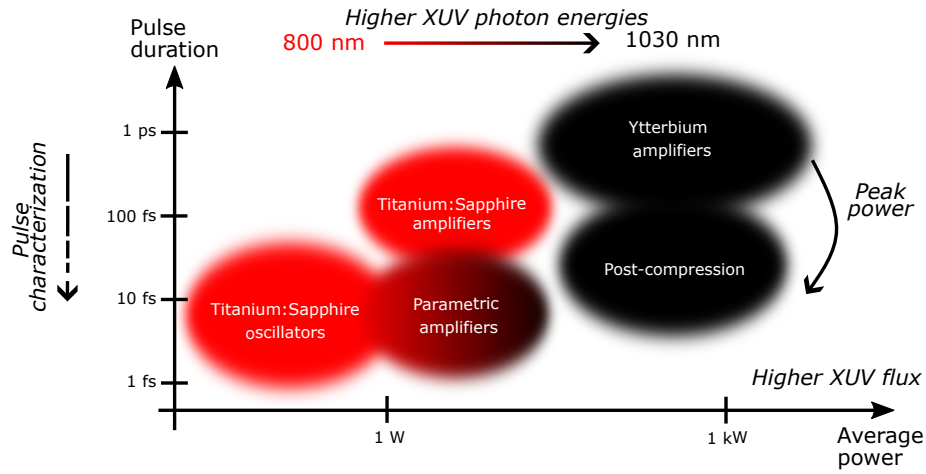

Figure 1.2: Current laser technologies for high-harmonic generation in terms of average power and pulse duration.

between pump and laser photon energy, the so-called quantum defect, almost half of the energy that is used to pump the laser is dissipated as heat. Amplifying at high repetition rates is therefore hardly possible.

An alternative to Ti:Sa lasers are Ytterbium-based systems [19]. Naturally, Ytterbium (Yb) amplifiers have rather long pulse durations (few hundreds of fs to ps) because of their narrow gain bandwidth. However, the quantum defect is minimal, enabling amplification at high repetition rates. This makes them also suitable as a pump for optical parametric amplification [20] where no energy is stored in the medium, so amplification can be conducted without any heating. Another benefit of Yb is the long life time in the upper laser level compared to Ti:Sa (ms instead of µs), allowing pumping with efficient, continuous-wave diodes, bringing down the costs for an amplifier system significantly.

To achieve short pulses with an Yb amplifier, without significant losses, these pulses have to be post-compressed in a separate step. Post-compression methods [21], such as multi-pass cells (MPCs) [22], are very versatile with respect to the required average power throughput and output pulse duration, giving great flexibility for the desired application. Especially because of their cost and power efficiency compared to the well-established Ti:Sa systems, Yb-driven HHG sources have the potential to become the new laboratory standard for a wide variety of applications.

All of these developments in laser technology add coherently to the motivation of this thesis:

- Higher average powers, thus higher repetition rates can be translated to a higher flux in XUV which benefits the statistics of experiments.
- The versatility of post-compression schemes gives power scalability to reach the optimum conditions for specific HHG targets [23, 24].
- Yb-based lasers operate in the near-infrared at $1030\,\mathrm{nm}$ compared to Ti:Sa sources at $800\,\mathrm{nm}$, benefiting the maximum energy that can be reached with HHG due to its λ^2 energy cutoff scaling [8]
- Longer pulses from Yb systems are sometimes extremely beneficial from a practical, experimental point of view: their narrow frequency bandwidth allows to built waveform synthesizers with a large level of flexibility and parameter control.
- Pulse characterization research, especially towards shorter pulses and single-shot capabilities also at high repetition rates, increases the insights into the laser development process and helps to better describe the HHG generation conditions.

An overview of the developments in laser technology in connection with HHG research is shown in Fig. 1.2.

1.3 Outline

This thesis covers the investigation of MPCs as a post-compression method for Yb lasers, research on ultrashort laser pulse characterization methods and HHG using two laser colors, summarizing the results of the six attached publications.

In Chapter 2, an introduction to the most important concepts of ultrafast optics that are relevant for this thesis work is given. This small overview covers the relation between the spectral and temporal electric field representation as well as polarization. The properties of laser beams and pulses and their interaction with optical elements are introduced, including spatial abberations and spatio-temporal couplings. In the end, the origin of some nonlinear effects will be described, which includes second-harmonic generation, spectral broadening, and self-focusing in a Kerr medium, and the basics of high-order harmonic generation.

Chapter 3 focuses on the aspect of laser technology. A more detailed comparison between Ti:Sa and Yb-based lasers is given. Afterwards, the concept of post-compression is introduced before the method of MPCs is discussed in detail. In **Paper I** we developed an MPC using only standard components, compressing $300\,\mathrm{fs}$ pulses from an

Yb rod amplifier to 31 fs with $> 87\,\%$ efficiency, pushing MPCs using only bulk as broadening medium into the multi-gigawatt regime. This chapter introduces the design choices behind the experimental setup in this publication and motivates the importance of post-compression research and MPCs, the latter being a relatively young research field. Energy scaling of MPCs is briefly discussed in the context of **Paper VI**.

For any experiment, especially towards HHG, knowledge of the laser parameters is essential to ensure a correct result interpretation. Chapter 4 introduces the pulse characterization methods we used throughout all publications. This includes beam quality (M^2), pulse duration measurements (frequency resolved optical gating and dispersion-scan), time-dependent polarization characterization (polarization dispersion-scan), spatio-temporal couplings (spatially-resolved Fourier transform spectrometry) and single-shot carrier envelope phase detection (via optical Fourier transform). A focus is placed on the independent pulse characterization research projects, which are discussed in detail in **Papers II** (time dependent polarization) and **III** (single shot carrier-envelope phase detection).

Chapter 5 focuses on the enhancement of XUV flux with HHG using a two-color waveform synthesizer (**Paper IV**). The experimental results are discussed, where the optimum parameters for a two-color laser field are determined and demonstrated to optimize the flux for a specific harmonic order. These results are discussed extensively in **Paper V**.

Finally, a summary and outlook of this thesis work is given in Chapter 6.

Chapter 2

Introduction to ultrafast optics and high-order harmonic generation

In this chapter, an introduction is given to the most important concepts of ultrafast optics and HHG used within this thesis. For ultrafast optics, the formalism was inspired by [25] and [26].

2.1 The electric field in time and frequency domain

A monochromatic electromagnetic wave is characterized by a frequency f or angular frequency $\omega = 2\pi f$, with a wavelength corresponding to $\lambda = v/f$, where v is the wave velocity in the medium. In vacuum, $v = c$. A pulse consists of many frequencies, with its central frequency ω_0 called the *carrier*. Often it is useful to describe the electric field of a pulse in a complex form in the spectral domain:

$$\tilde{\mathbf{E}}(\omega) = |\tilde{\mathbf{E}}(\omega)|e^{-i\phi(\omega)} \tag{2.1}$$

where $\phi(\omega)$ is the so-called *spectral phase*. The time and frequency descriptions are directly linked by a *Fourier transform*:

$$\tilde{\mathbf{E}}(\omega) = \int_{-\infty}^{+\infty} \mathbf{E}(\mathbf{t})e^{-i\omega t}dt \tag{2.2}$$

$$\mathbf{E}(\mathbf{t}) = \frac{1}{2\pi}\int_{-\infty}^{+\infty} \tilde{\mathbf{E}}(\omega)e^{i\omega t}d\omega \tag{2.3}$$

The so-called *time-bandwidth product limit* indicates that the product of the full width at half maximum (FWHM) of the pulse duration Δt and spectral bandwidth $\Delta\omega$

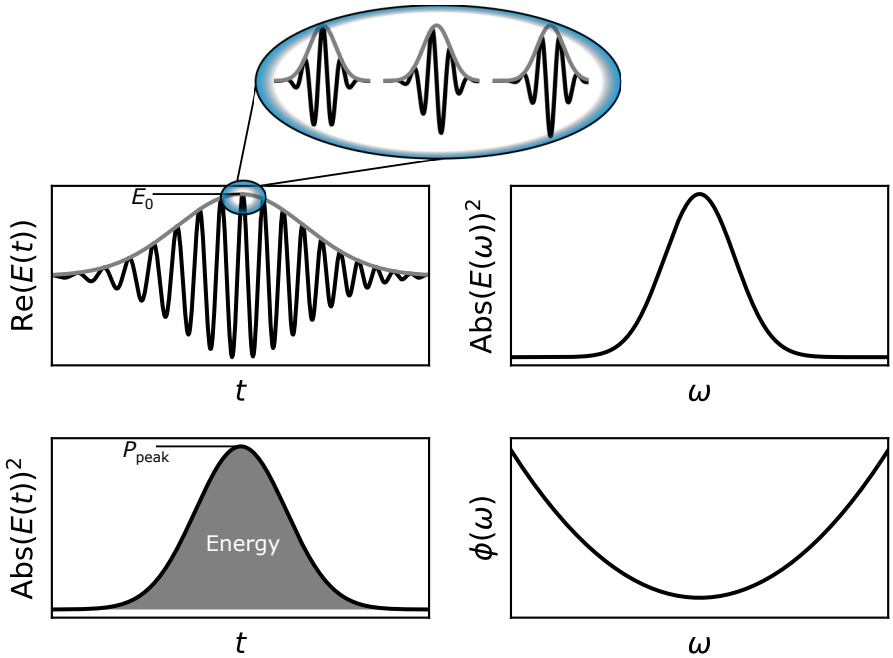

Figure 2.1: Illustration of the electric field in time (left) and frequency (right) in its most relevant representations. The carrier-envelope phase, where the difference between carrier (black) and envelope (grey) is 0 (left), $\pi/2$ (middle) and π (right) is shown as an inset on the top.

must be larger than a constant,

$$\Delta t \Delta \omega \geq \text{const.} \tag{2.4}$$

As a result, it means that the shorter the pulse is, the larger the spectral bandwidth has to be. When the time-bandwidth product equals the constant, the pulse is as short as it can physically be at its *Fourier-transform-limit* (FTL). Different pulse shapes correspond to different constants.

The most commonly used representations of these equations are displayed in Fig. 2.1. In the upper left, the real part of $\tilde{\mathbf{E}}(\mathbf{t})$ is shown in black, with its maximum value E_0. The *envelope* is drawn in gray. The maxima of the carrier oscillation and the envelope do not necessarily align. This offset is described by the *carrier-envelope phase-offset* (CEP). For very short pulses, where only a few oscillations of the electric field are contained under the envelope, the CEP can shape the electric field significantly. An example of different CEPs is illustrated in the inset at the top in Fig. 2.1.

The absolute squared value of $\tilde{\mathbf{E}}(\mathbf{t})$ is proportional to the optical power. If this curve is normalized by the area with the energy contained in such a pulse (gray area), the maximum value is read as the peak power P_{peak}, shown on the lower left of Fig. 2.1.

The only representation which is directly, and easily accessible in an experiment by using an optical spectrometer is the spectral intensity $I(\omega) = |\tilde{\mathbf{E}}(\omega)|^2$, is displayed on the upper right.

The measurement of the spectral phase $\phi(\omega)$, shown in the bottom right, requires more complicated schemes discussed in Chapter 4. The spectral phase can be expanded as a Taylor series arround the carrier ω_0:

$$\phi(\omega) = \phi_0 + \underbrace{\frac{d\phi}{d\omega}}_{\text{GD}}(\omega - \omega_0) + \frac{1}{2}\underbrace{\frac{d^2\phi}{d\omega^2}}_{\text{GDD}}(\omega - \omega_0)^2 + \frac{1}{6}\underbrace{\frac{d^3\phi}{d\omega^3}}_{\text{TOD}}(\omega - \omega_0)^3 + \dots \quad (2.5)$$

The effect of the individual components, highlighted under the separate terms in Eq. (2.5), can be understood very intuitively. An overview of these effects on very short (top row) and longer (bottom row) pulses is illustrated in Fig. 2.2. In the leftmost column, the pulses are displayed in the frequency domain, with a broad spectrum for short pulses in time (top) and a narrower bandwidth for long pulses (bot-

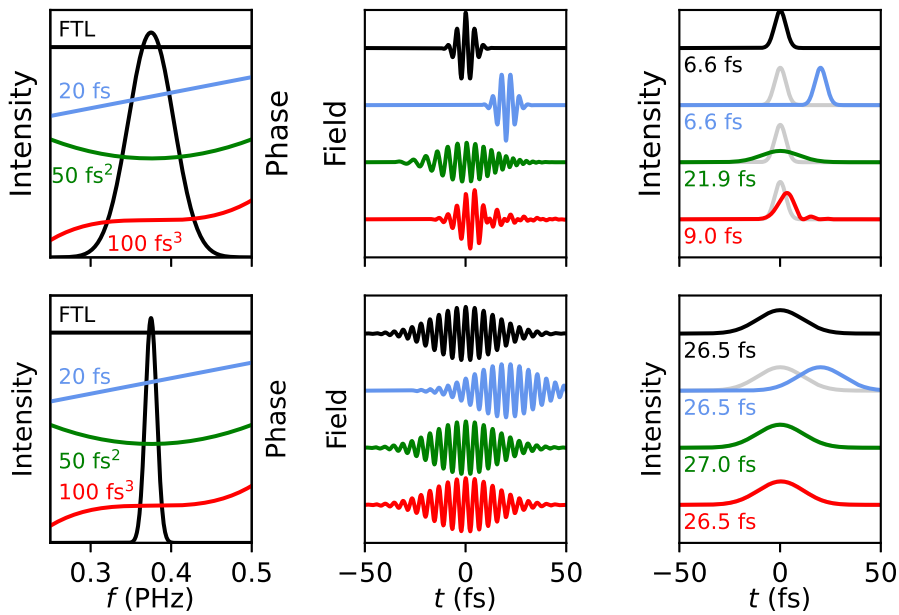

Figure 2.2: Influence of adding the same spectral phase terms on a short (upper row) and long (lower row) Fourier-limited pulse, for GD $= 20\,\text{fs}$ (blue), GDD $= 50\,\text{fs}^2$ (green) and TOD $= 100\,\text{fs}^3$ (red). The spectrum with the phase components are on the left, the electric fields in time in the middle and the intensity profiles on the right. The Fourier-limited solution (black) is superimposed in grey to highlight the changes. The numbers on the right tell the pulse length (FWHM).

tom). The spectral phase components that are applied are identical for both pulses and highlighted as colored lines on top of the spectrum.

The Fourier-tranforms to the time domain are displayed in the middle column for the electric field and on the right for the intensity. A constant phase (black) describes the FTL. In this case, the peak of the carrier is also aligned with the peak of the envelope. A linear phase, also known as the group delay (GD, blue), moves the envelope in time. The intensity is not changed, as illustrated to the right in direct comparison to the FTL (gray). However, it can have an effect on the CEP. In this example, it introduced a phase shift of π (top middle, blue). The same CEP change is also present for the longer pulse at the bottom, but due to its length it is barely noticeable.

The second derivative of the spectral phase, also known as group delay dispersion (GDD), describes the so-called *chirp*, given in the unit of fs^2 which stretches a Fourier-limited pulse in time. This is illustrated in green. Very short pulses are very susceptible to chirp because of their large bandwidth. In the example in Fig. 2.2 the same amount of GDD stretches the short pulse by more than a factor of three, thus drastically reducing its peak power, while the long pulse is hardly affected. Third-order dispersion (TOD), given in fs^3, gives rise to a side pulse, illustrated in red in Fig. 2.2, degrading the temporal contrast. Such a side pulse can be detrimental for some applications, i.e. photoionization [27].

2.2 Propagation in a material

If an electromagnetic wave propagates in a material, it interacts with the electrons of the atoms, displacing them, and thus forming oscillating *dipoles*. To describe the magnitude of dipole moments formed in the medium over a unit volume, the polarization density P is used, defined by

$$\tilde{\mathbf{P}} = \epsilon_0 \chi \tilde{\mathbf{E}} \,. \tag{2.6}$$

It depends on the vacuum permittivity ϵ_0 and the proportionality constant χ called *susceptibility*. χ encodes the effort needed to form a dipole, described by the *refractive index* n of the material. These constants are related by

$$n = \sqrt{1+\chi} = \frac{c}{v} \tag{2.7}$$

which also encodes the change in velocity of E within the medium. With the *wavenumber* $k = n2\pi/\lambda$ the electric field can now be described in time and space (along the propagation direction z):

$$\mathbf{E}(\mathbf{t}) = |\mathbf{E}(\mathbf{t})| e^{i\omega t - ikz} \tag{2.8}$$

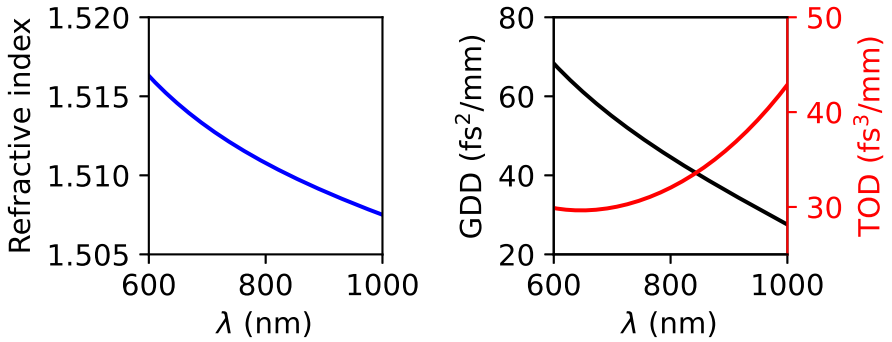

Figure 2.3: Wavelength-dependent refractive index n (left) and its effect on GDD and TOD (right) for BK-7 glass.

If n is wavelength-dependent, the material is called *dispersive*, and the spectral phase that is added to $\tilde{\mathbf{E}}(\omega)$ upon propagation reads

$$\phi_{\text{material}}(\omega) = kn(\omega)z\,. \tag{2.9}$$

Analogue to Eq. (2.5), this phase term can be decomposed into its orders, which are often given in terms of a unit length of the material. An example is illustrated in Fig. 2.3 for BK-7, a commonly used glass in optics. On the left, its refractive index is plotted with respect to the wavelength. On the right, the corresponding values for GDD and TOD are displayed, per length of material.

2.3 Polarization

Polarization describes the course of the electric field vector $\tilde{\mathbf{E}}(r,t)$, perpendicular to its propagation direction z. The electric field of a monochromatic wave travelling along the z direction can be written as

$$\tilde{\mathbf{E}}(r,t) = \tilde{\mathbf{E}}(r)e^{i(\omega t-kz)} = (E_x\hat{x} + E_y\hat{y})e^{i(\omega t-kz)} \tag{2.10}$$

$$= (|E_x|\hat{x} + e^{i\varphi}|E_y|\hat{y})e^{i(\omega t-kz)} \tag{2.11}$$

The phase φ encodes the phase-offset between the x- and y-components. A few examples are shown in Fig. 2.4 for a monochromatic wave travelling along the z direction, with E_x and E_y projected onto the respective plane. Linear polarization, with the field oscillating along the direction of $\tilde{\mathbf{E}}$ is presented for the two most common cases: $|E_y| = 0$ (left) horizontally, and $|E_x| = 0$ (middle left) vertically polarized light. If $\varphi = \pi/4$ and $|E_x| = |E_y|$ the electric field is circularly polarized (middle right).

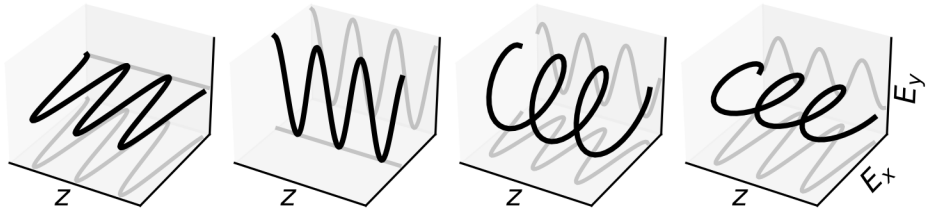

Figure 2.4: Graphic representation of Eq. (2.10) with examples of horizontal (left), vertical (middle left), circular (middle right) and elliptical (right) polarization of a monochromatic wave. The x and y components are projected onto their respective plane (gray).

If these conditions are not met the polarization state can in general be described as elliptical (right).

It is often useful to capture the polarization in the *Jones* formalism. The Jones-vector $\mathbf{J}$ indicates the polarization state as

$$\mathbf{J} = \begin{bmatrix} |E_x| \\ |E_y|e^{i\varphi} \end{bmatrix} \tag{2.12}$$

The interaction with elements that alter the polarization state can be described by Jones-matrices $\mathbf{M_j}$, so that $\mathbf{J}_{\text{new}} = \mathbf{M_j}\mathbf{J}_{\text{old}}$. Jones matrices often represent specific polarization components, such as polarization selecting elements like polarizers or polarization-altering elements such as waveplates. The latter require a material that changes φ, which can be achieved by experiencing a different refractive index along different crystallographic axes, an effect known as *birefringence*. The term *optical axis* refers to the crystal direction along which the polarization of the light is not affected. If such a material has a thickness d, the phase delay $\Delta\varphi$ that is accumulated when passing through not along the optical axis is

$$\Delta\varphi = \frac{2\pi d \Delta n}{\lambda} \tag{2.13}$$

where Δn is the difference in refractive index for the x and y component of the electric field. For $\Delta\varphi = \pi$ it is a half-wave plate, rotating linear polarisation by $90°$, for $\Delta\varphi = \pi/2$ it is a quarter-wave plate turning linear polarization to circular and vice versa.

In the context of ultra-short pulses it is required to express Eq. (2.12) in a frequency-resolved manner due to the effect of dispersion.

An example of a birefringent material is Quartz, illustrated in Fig. 2.5, with two different refractive indices n_o (ordinary, dashed) and n_e (extraordinary, solid) shown, together with their absolute difference Δn in red. The ordinary index is perpendicular to the optical axis, the extraordinary is parallel.

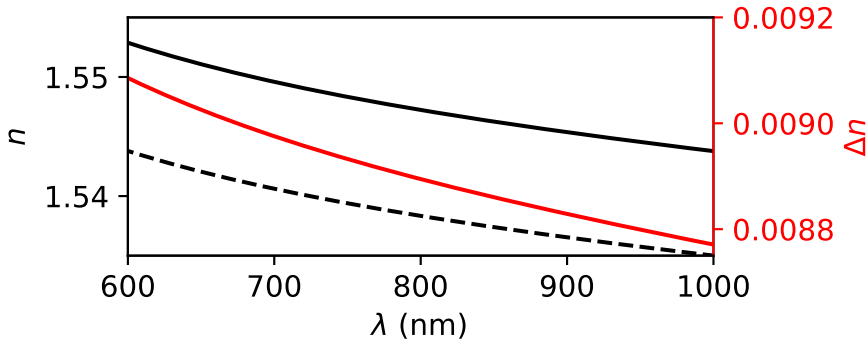

Figure 2.5: Refractive index n for Quartz for the ordinary axis (dashed) and extraordinary axis (solid). The difference Δn is shown on the right axis in red.

These optical components are usually designed for one specific wavelength, by choosing d so that Eq. (2.13) satisfies the desired condition. For an ultra-short pulse with a broad spectrum interacting with such an element, this can lead to time-dependent variations of the polarization state. To illustrate the effects, a perfectly linearly, horizontally polarized pulse is displayed in the middle in Fig. 2.6. This pulse now passes through a half-waveplate that is designed for $\lambda = 800\,\mathrm{nm}$, while its whole spectrum is spanning the range displayed in Fig. 2.5. The result is a pulse that is perfectly linearly polarized in the center, while towards the pulse edges there is still a significant contribution of the electric field along the x axis (right).

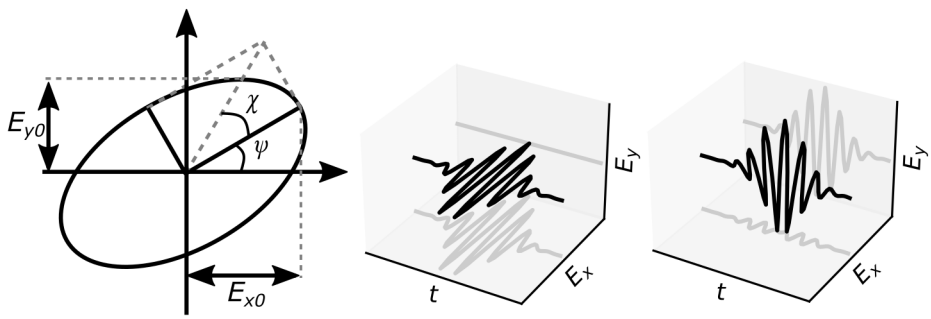

Figure 2.6: Polarization ellipse (left). Example of an electric field of an ultrashort laser pulse in perfect horizontal, linear polarization (middle) and after passing through a zero-order half-wave plate designed for the pulse's central wavelength (right).

For such complicated and time-dependent polarization states, it is convenient to introduce the polarization ellipse, illustrated in Fig. 2.6 on the left, defined by the angles χ and ψ. χ describes the angle of ellipticity, which is the amplitude ratio of its major

and minor components. If $\chi = 0$, the ellipse turns into a line, which encodes linear polarization, with $0° \leq \psi \leq 90°$ indicating its oscillation direction. For $\chi = \pm 45°$ the light is right-hand $(+)$ or left-hand $(-)$ circularly polarized.

2.4 Gaussian beams

Laser beams are within the paraxial approximation described by Gaussian beam theory, with an amplitude of

$$A(r,z) = A_0 \frac{w_0}{w(z)} e^{\frac{-r^2}{w(z)^2}} e^{-ikz + ik\frac{r^2}{2R(z)} - i\psi(z)} \tag{2.14}$$

and an intensity of

$$I(r,z) = \frac{2P}{\pi w(z)^2} e^{-\frac{2r^2}{w(z)^2}} \tag{2.15}$$

where P is the optical power and $w(z)$ the beam radius at $1/e^2$ of its intensity along its propagation direction z and radial coordinate r. Equation (2.15) is visualized in Fig. 2.7. The grey line follows $w(z)$, defined by

$$w(z) = w_0 \sqrt{1 + (z/z_R)^2}\,. \tag{2.16}$$

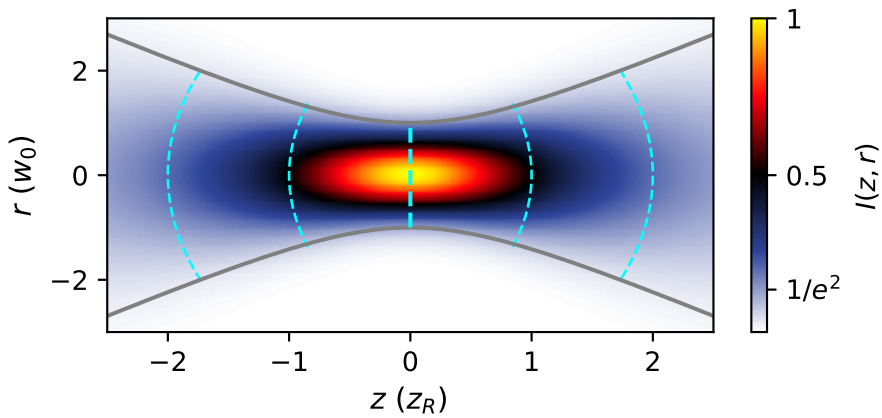

Figure 2.7: Intensity profile for a Gaussian beam following the absolute squared value of Eq. (2.15) (color). The grey lines outline $w(z)$ (see Eq. (2.16)). The wavefront curvature R is illustrated by the cyan, dashed lines (see Eq. (2.18)).

It depends on the beam radius w_0 at the geometrical focus $z = 0$ and its Rayleigh length z_R, equal to

$$z_R = \frac{\pi w_0^2}{\lambda} \,. \tag{2.17}$$

The radius of curvature R of a Gaussian beam is

$$R(z) = z \left(1 + (z_R/z)^2\right) \,, \tag{2.18}$$

indicated by the blue dashed lines in Fig. 2.7. The electric field undergoes a phase-shift when passing through the geometrical focus called the Gouy phase shift $\psi(z)$:

$$\psi(z) = \arctan\left(\frac{z}{z_R}\right) \tag{2.19}$$

It is often useful to describe a Gaussian beam by its complex beam parameter $q(z)$, with

$$\frac{1}{q(z)} = \frac{1}{R(z)} - \frac{i\lambda}{\pi n w(z)^2} \,. \tag{2.20}$$

Equation (2.20) can be rearranged to

$$q(z) = z + \frac{i\pi n w_0^2}{\lambda} = z + i z_R \,. \tag{2.21}$$

To describe how the q parameter changes when interacting with an optical element, such as a mirror, a focusing lens, or a refractive medium, $ABCD$ matrices are introduced. They originate from geometrical optics and act on a vector, consisting of position x relative to a propagation axis z, and angle θ:

$$\begin{bmatrix} x_2 \\ \theta_2 \end{bmatrix} = \begin{bmatrix} A & B \\ C & D \end{bmatrix} \begin{bmatrix} x_1 \\ \theta_1 \end{bmatrix} \tag{2.22}$$

Adapting this formalism to Gaussian beams, the evolution of the q parameter reads

$$q_2 = \frac{Aq_1 + B}{Cq_1 + D} \,. \tag{2.23}$$

An overview of $ABCD$ matrices of common optical elements is given in Table 2.1. To describe a more complicated system made out of many elements, these matrices can be multiplied by each other.

Table 2.1: Examples of a few important $ABCD$ matrices.

Optical element	$ABCD$ matrix
Free space propagation with distance d	$\begin{bmatrix} 1 & d \\ 0 & 1 \end{bmatrix}$
Refraction at a flat interface from n_1 to n_2	$\begin{bmatrix} 1 & 0 \\ 0 & n_1/n_2 \end{bmatrix}$
Reflection from a curved mirror with curvature R	$\begin{bmatrix} 1 & 0 \\ -2/R & 1 \end{bmatrix}$
Transmission through a thin lens with focal length f	$\begin{bmatrix} 1 & 0 \\ -1/f & 1 \end{bmatrix}$

2.5 Spatial aberrations

In an ideal case, the wavefront $\phi(r, \theta)$ of a Gaussian beam (see Eq. (2.14)) is flat in the focus or approximately parabolic withing the paraxial approximation, corresponding to a curvature of R (see Eq. (2.18)). However, in practice, interactions with optical elements such as lenses or mirrors often distort the wavefront. To better describe this wavefront, $\phi(r, \theta)$ can be decomposed into an orthogonal basis. For an optical wavefront, the most common method is the *Zernike-decomposition* [28], where the Zernike polynomials, in radial coordinates, are defined as

$$Z_n^l(r,\theta) \propto \sum_{k=0}^{(n-|l|)/2} \frac{(-1)^k (n-k)!}{k!\left(\frac{n+|l|}{2}-k\right)!\left(\frac{n-|l|}{2}-k\right)!} r^{n-2k} \begin{cases} \cdot \cos(l\theta) & (l \geq 0) \\ \cdot \sin(|l|\theta) & (l < 0) \end{cases} \tag{2.24}$$

with $|l| \leq n$ and n and l being both odd or even. The spatial phase then takes the form of

$$\phi(r,\theta) = \sum_{n,l} C_n^l Z_n^l(r,\theta) \tag{2.25}$$

where C_n^l is the Zernike amplitude.

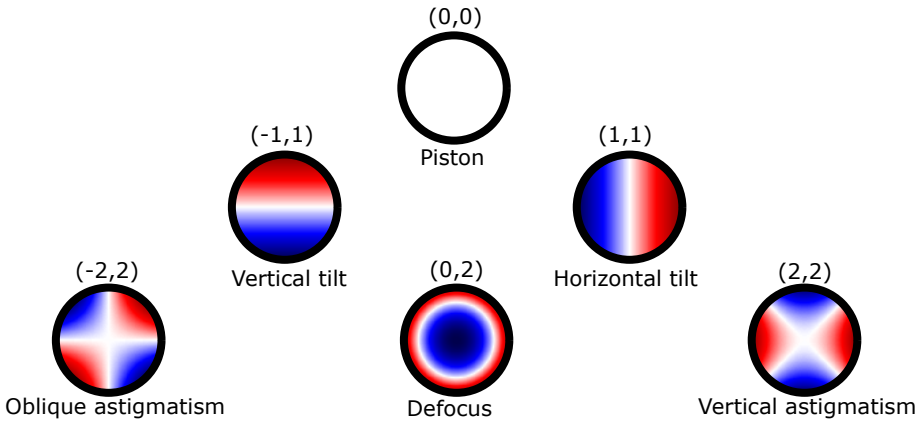

Figure 2.8: Example of the first six Zernike polynomials with indices (n, l) according to Eq. (??).

The first few examples of $Z_n^l(r, \theta)$ are illustrated in Fig. 2.8, with their corresponding names. The effects of those wavefront abberations in the near-field become only visible in the far-field. To reach the far-field computationally, a Fresnell-Kirchhoff diffraction integral needs to be performed [29], which however in the Fraunhofer approximation becomes a Fourier transformation. In practice, this can be achieved by focusing the beam down, illustrated in Fig. 2.9. A wavefront tilt, which can be decomposed into vertical and horizontal components, will result in a direction-corresponding shift of the focus position within the focal plane. More complicated components will move or distort the focal plane. An example is shown at the bottom of Fig. 2.9 where an arbitrary combination of different Zernike polynomials significantly distorts the beam profile in the focus, changing its shape and thus lowering the maximum peak intensity that can be achieved significantly.

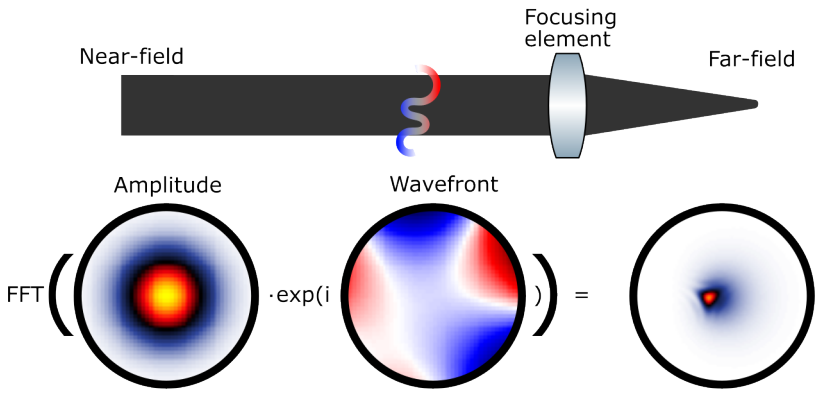

Figure 2.9: Relation between near-field (left) and far-field (right) of a laser beam profile, related by a Fourier transformation.

2.6 Spatio-temporal couplings

For laser pulses, it is often assumed that each color shares the same spatial wavefront, or that the description of the electric field $E(r, \omega)$ depending on its frequency and spatial coordinates can be fully separated into

$$E(r, \omega) = E(r) \cdot E(\omega) \,. \tag{2.26}$$

If Eq. 2.26 is not valid, the laser pulse is subjected to *spatio-temporal couplings* (STC) [30, 31]. STCs can be described in different domains, all related by a Fourier transformation along different axes. In Fig. 2.10 an overview is given for the relation between spatial coordinate x, angular component k, time t and frequency f for the example of an ultrashort pulse that has traveled through a BK-7 glass prism separating the different colors angularly.

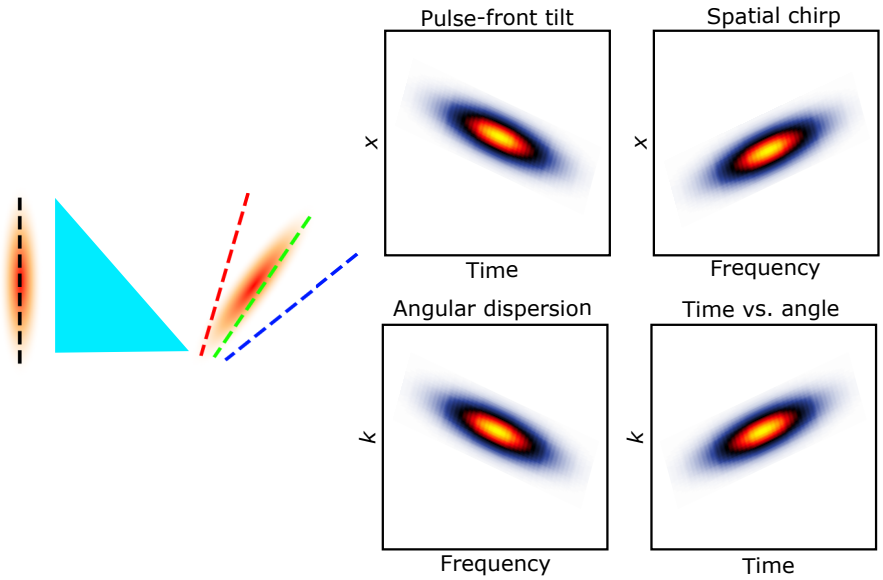

Figure 2.10: Illustration of spatio-temporal couplings in the different domains, for an ultrashort pulse after passing through a BK-7 prism (leftmost) for $E(t, x)$ (top left), $E(f, x)$ (top right), $E(f, k)$ (bottom left) and $E(t, k)$ (bottom right). The wavefront is represented by the dashed lines. This figure is inspired by [30].

The top part of the beam propagates through less material than the bottom part, applying a spatially-dependent spectral phase. In addition, as BK-7 glass is a dispersive material with a higher refractive index for the shorter wavelengths (blue) than for the longer wavelengths (red), see Fig. 2.3, different frequencies experience a different propagation angle after the prism, which is illustrated by the dashed lines indicating the wavefront. In terms of intensity, when the beam is focused down, this will cause a

different focus position for different colors, called the spatial chirp (top right). In the time domain, this is equivalent to a pulse-front tilt (top left), meaning that pulse front and phase front are not parallel to each other anymore. In the angular domain, different colors travel at different angles (bottom left). Less common is the time vs. angle description (bottom right).

2.7 Nonlinear optics

The relation between polarizability P and E is linear, see Eq. 2.6, if E is small. For stronger electric fields the relation becomes nonlinear and can be expressed in a Taylor expansion:

$$P = \epsilon_0 \left(\chi^{(1)} E + \chi^{(2)} E^2 + \chi^{(3)} E^3 + \dots \right) \tag{2.27}$$

Which of these terms are relevant depends on the material properties and most importantly on the inversion symmetry. A material with inversion symmetry fulfills the condition that when all spatial coordinates are inverted ($(x, y, z) \rightarrow (-x, -y, -z)$) it is still the same material. If $E \rightarrow -E$, P must transform in the same way with Eq. (2.27) still being fullfilled. This means that all even-order terms have to be zero due to their quadratic, quartic etc. dependency on E. In summary, centrosymmetric materials, such as fused silica glass or noble gases, can only exhibit odd-order effects. For noncentrosymmetric materials this restriction is lifted, allowing all of the terms in Eq. (2.27) to be considered. Since the strength of the contributing terms is proportional to the order, in a perturbative approximation, the second-order nonlinear term usually dominates. In the following, a few relevant examples for second- and third-order nonlinear effects are given.

2.7.1 Three-wave mixing

When light with frequencies ω_1 and ω_2 enters a noncentrosymmetric medium such as beta-barium-borate (BBO), its polarizability is proportional to E^2:

$$P(\omega_1, \omega_2) \propto \left(E_1 \exp(i\omega_1 t - ik_1 z) + E_2 \exp(i\omega_2 t - ik_2 z) \right)^2 \tag{2.28}$$

resulting in fields oscillating with the frequencies $2\omega_1$, $2\omega_2$, $\omega_1 - \omega_2$ and $\omega_1 + \omega_2$. These terms are commonly known as second-harmonic generation (SHG), difference frequency generation (DFG) and sum frequency generation (SFG). The efficiency of the generation of new frequencies (ω_3) depends on the so-called phase-matching condition, where the sum of the wavevectors $\tilde{\mathbf{k}}$ must add up, taken into account the

wavelength specific refractive index n of the material:

$$n(\omega_1)\tilde{\mathbf{k}}_\mathbf{1} + n(\omega_2)\tilde{\mathbf{k}}_\mathbf{2} = n(\omega_3)\tilde{\mathbf{k}}_\mathbf{3}\,. \tag{2.29}$$

For collinear second-harmonic generation, which was first discovered in 1961 [32], where $k_1 = k_2 = k$ and $k_3 = 2k$, this condition becomes

$$n(\omega) = n(2\omega)\,. \tag{2.30}$$

This condition can only be fulfilled in a birefringent crystal exhibiting different refractive indices depending on the crystal axis, which by definition cannot be centrosymmetric. For a uniaxial crystal, assuming propagation along one principal axis of the crystal, the angular dependence (with respect to the other, perpendicular principal axis) of the refractive index can be described by the ellipse equation

$$\frac{1}{n^2(\theta)} = \frac{\cos^2\theta}{n_0^2} + \frac{\sin^2\theta}{n_e^2}\,. \tag{2.31}$$

In practice, crystals are cut with a specific angle θ (phase-matching angle), to fulfill the condition in Eq. (2.31) and achieve phase-matching at a given wavelength. As ultrashort pulses have a broad spectrum, the *phase-matching bandwidth* Δf is an important quantity as θ varies with f. It can be described by [25]

$$\Delta f = \frac{c}{2L\Delta N_g} \tag{2.32}$$

where $N_g = n - \lambda_0 \frac{dn}{d\lambda}$ is the group refractive index and L is the crystal length. The overall SHG efficiency η depends on

$$\eta \propto L^2 I^2 \mathrm{sinc}^2\left(\frac{\Delta k L}{2}\right) \tag{2.33}$$

where I is the intensity and Δk is the wavevector mismatch. Equation (2.32) hereby describes the width of the sinc function in Eq. (2.33).

2.7.2 Optical Kerr effect

In centrosymmetric media the optical Kerr effect dominates at high electric field intensities. It originates from the intensity-dependent refractive index n, which is related to the nonlinear refractive index n_2:

$$n(I) = n_0 + n_2 I \tag{2.34}$$

This has several consequences. In the temporal domain, a short pulse has a varying intensity over time, illustrated in the top left Fig. 2.11, consequently exhibiting a

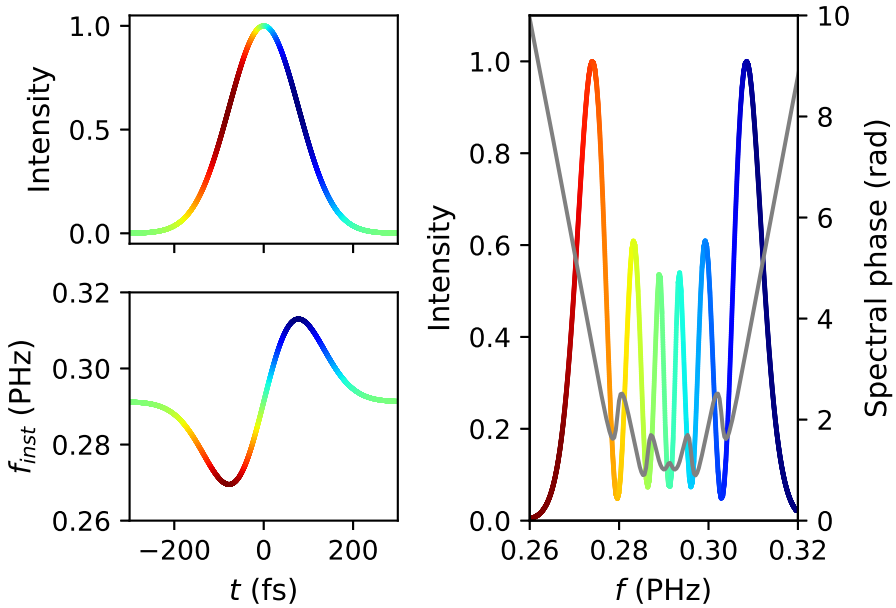

Figure 2.11: Illustration of self-phase modulation. The temporal intensity profile is shown (top left) and the instantaneous frequency according to Eq.(2.35) (bottom left). The result of the spectral broadening is presented on the right in terms of spectral intensity (colored) and spectral phase (grey).

time-varying refractive index and thus causing a time-dependent phase and therefore the addition of new instantaneous frequencies ω_{inst}. This effect is used to spectrally broaden a pulse. n_2 is a material constant, and together with the information of the thickness (z) of the material, the new frequencies can be calculated as

$$\omega_{\text{inst}}(t,z) = \frac{d\phi}{dt} = \omega_0 - \frac{\omega_0}{c} n_2 \frac{dI(t,z)}{dt} z \tag{2.35}$$

shown in the bottom left of Fig. 2.11, with a resulting spectrum displaying a characteristic modulation on the right. This effect is known as *self-phase modulation*, which was first discovered in liquids [32] in 1961 before being investigated in solid materials [33]. The color-coding in time represents which part of the pulse is responsible for which frequency. ω_{inst} depends on the time derivative of the intensity, or slope of the intensity profile, with the leading edge responsible for the lower frequencies (red) and the trailing edge (blue) for the higher frequencies. The phase change in time is also directly related to a quadratic spectral phase term, shown in grey in Fig. 2.11 to the right, introducing a significant amount of GDD.

There can also be an intensity-dependent profile in the transverse spatial direction. Assuming a Gaussian intensity beam profile, which can be approximated by a parabola,

a material with thickness d, a beam width w and a peak power P, acts as a lens with the inverse focal length

$$\frac{1}{f_{\text{Kerr}}} = \frac{8n_2 d}{\pi w^4} P\,. \tag{2.36}$$

This is known as *self-focusing* [34]. When the peak power of a laser exceeds the critical power P_{crit} of the material,

$$P_{\text{crit}} = \frac{\alpha \lambda^2}{4 n_0 n_2} \tag{2.37}$$

with $\alpha = 1.8$ for a Gaussian beam, self-focusing can lead to a beam collapse.

Self-focusing and spectral broadening go inevitably together, as one is the effect in the spatial domain and the other in the temporal domain. A useful quantity is the B-integral, which describes how much non-linear phase is accumulated in a system, assuming the on-axis intensity $I(z)$:

$$B = \frac{2\pi}{\lambda} \int n_2 I(z) dz \tag{2.38}$$

2.8 High-order harmonic generation in gases

2.8.1 The three-step model

High-order harmonic generation is a nonlinear effect that does not follow the perturbative expansion of Eq. (2.27). It can be described in an intuitive picture called the semi-classical three-step model [8], illustrated in Fig. 2.12. When a very strong electric field interacts with an atom, its potential can be distorted, so the electron may be freed into the continuum by tunneling. The second step describes its acceleration in the continuum, where the electron accumulates kinetic energy. When the electric

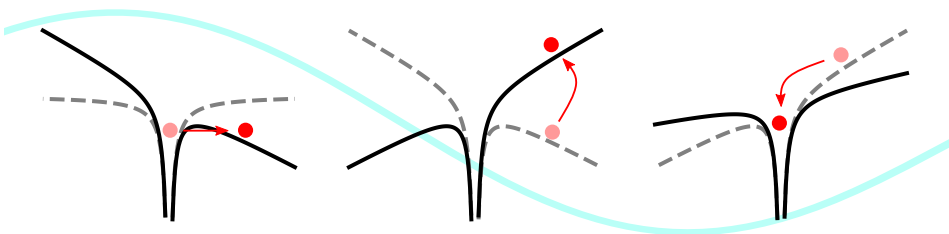

Figure 2.12: Illustration of the three-step model. Due to a strong electric field the potential is bent, allowing an electron to tunnel into the continuum (left). The electron is further accelerated (middle) before it might recombine (right) when the electric field changes its sign. The electric field is superimposed in the background.

field changes its sign, the electron is accelerated back to its parent atom, where it then eventually recombines. The excess kinetic energy is then emitted as a photon.

The calculation of the trajectories that the electron takes while being accelerated by a field following $E_0 \cos(\omega t)$ is done by solving the equation of motion

$$\frac{d^2x}{dt^2} = -\frac{eE_0}{m_e}\cos(\omega t) \tag{2.39}$$

for different times of ionization, where m_e is the electron mass and e the electron charge. Figure 2.13 shows all possible electron trajectories. The trajectories are colored, corresponding to their kinetic energy upon return (top). Non-returning trajectories are shown in black. The kinetic energy can be expressed as a function of the ponderomotive potential U_p, which is the cycle-averaged energy of a free electron in an electromagnetic field, defined by

$$U_p = \frac{e^2}{4m_e} \cdot \frac{E_0^2}{\omega^2}. \tag{2.40}$$

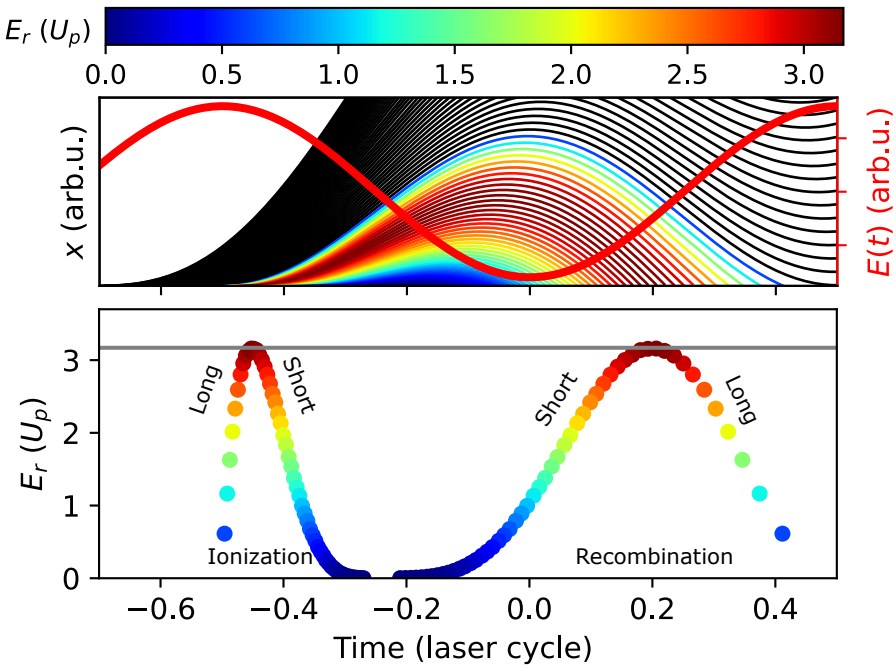

Figure 2.13: Trajectories calculated by solving Eq. (2.39) (top). Colored trajectories are the ones returning to the atom, with the color corresponding to their return energy, black trajectories do not return. The electric field is represented on the right axis in red. The return energies are plotted separately below, against ionization time (left) and recombination time (right). The cutoff of $3.17U_p$ is marked by the horizontal grey line.

The maximum kinetic energy an electron can acquire upon recombination is $3.17U_p$, taking into account the ionization potential I_p of the gas being used. Thus, the maximum photon energy that is emitted is

$$E_{\max} = I_p + 3.17U_p, \tag{2.41}$$

known as the "cutoff-law" [8]. In the bottom of Fig. 2.13, the return energies of the trajectories are plotted against both their time of ionization and their time of return. Often it is discriminated between "long" and "short" trajectories depending on their return time. This process is repeated every half-cycle of the electric field, giving rise to interference in the spectral domain and resulting in a comb of odd-order harmonics in the XUV regime.

A characteristic HHG spectrum is shown in Fig. 2.14 with the perturbation regime including the exponential decay of intensity for the very low-order harmonics, the plateau in the center with approximately constant intensity and the cut-off harmonics to the right.

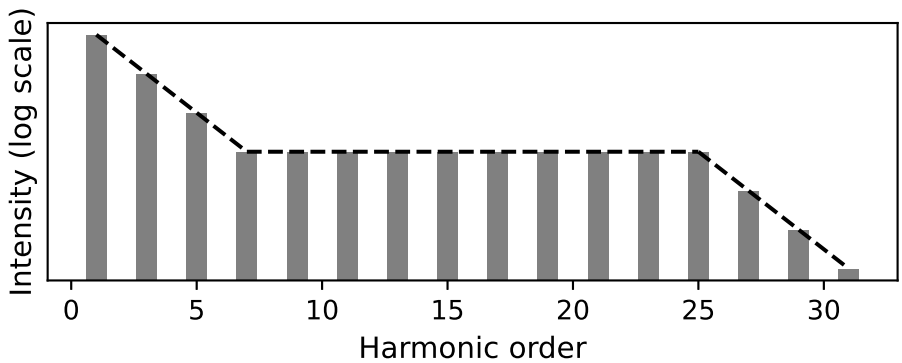

Figure 2.14: Typical HHG spectrum, featuring the perturbative regime at low harmonic orders, the plateau at medium orders and the cutoff at high orders.

2.8.2 Generation of attosecond pulses

The phase relation between the different harmonic orders is fixed by the return time of the electrons, as electrons with different kinetic energies return at different times, emitting the XUV photons with a delay relative to each other. Following the same principles as discussed in Sec. 2.1, this phase relation of the different colors determines if a short pulse can be generated.

In Fig. 2.15 an example is shown for several odd-order harmonics (colored) added together coherently (black). On the left, the different frequencies have a constant

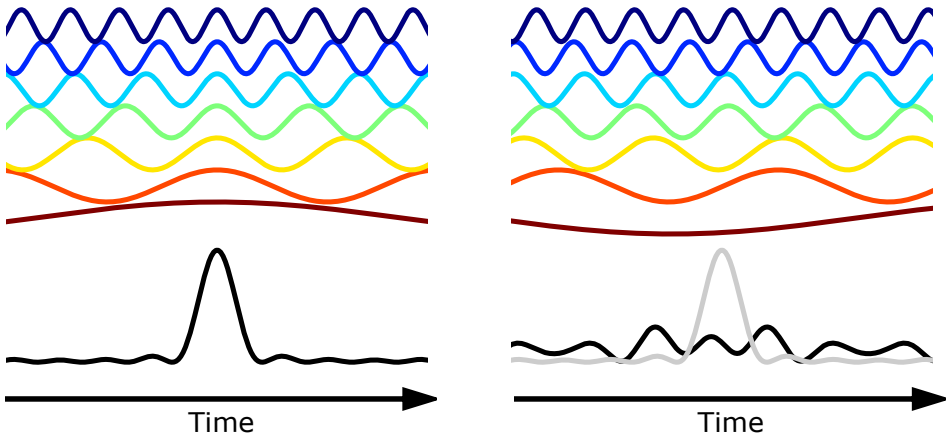

Figure 2.15: Waves with a respective frequency difference of 2ω added together, for a linear phase relation (left) and for a random phase relation (right).

phase relation adding up to a well-defined short pulse with roughly the duration of the central wavelength period (green/blue). On the right, the phase relation is random, resulting in intensity fluctuations without a short pulse. Since the central wavelength of the high-order harmonic plateau, see Fig. 2.14, is in the XUV range, its oscillation period, which defines the shortest possible pulse duration, equals several hundreds of attoseconds. If only short trajectories are selected, the slope of return energy vs. the return time, often referred to by its derivative, the *attochirp*, is approximately linear [35]. By pushing the HHG spectrum very far into the XUV, pulses of 43 as [36] and 53 as [37] were demonstrated in 2017.

If the laser pulses used for HHG are several cycles long, an attosecond pulse is emitted at every half-cycle, resulting in an *attosecond pulse train* [4]. If the electric field only contains one half-cycle with significant field strength for HHG, the HHG spectrum will be continuous without distinct harmonics [3].

2.8.3 Scaling and optimization

HHG is governed by a few scaling laws primarily determining the range and intensity of the resulting spectrum. From Eq. (2.40) and (2.41) it follows directly that the maximum photon energy that can be achieved, the cutoff, is linearly dependent on the intensity I of the driving laser and quadratically on the wavelength. These laws follow the simple mechanics of Newton, as the electron acquires more kinetic energy when exposed to a higher electric field, and also has more time to acquire kinetic energy when the time in the continuum is longer with longer driving wavelengths [9, 23]. However, generation efficiency suffers greatly when using longer wavelengths.

Different experiments demonstrated a decrease in conversion efficiency from λ^{-5} to λ^{-7}, originating mainly from the reduced probability of recombination due to the longer excursion time in the continuum as the electron wave-packet spreads spatially with time, referred to as *quantum diffusion* [11]. At wavelengths above $\approx 3\,\mu m$ the magnetic field B which is perpendicular to E and acts on the electrons with velocity v through the Lorenz force of $v \times B$, cannot be neglected anymore [38]. B displaces the returning electron with respect to its parent atom and therefore reduces the probability of recombination.

The intensity of the driving laser cannot be increased indefinitely, as a too high degree of ionization, leading to plasma generation, will result in the depletion of the XUV photons [39].

All of the above considerations refer to the interaction between an electric field and one atom, called *single-atom response*. In reality, billions of atoms interact with the laser at the same time. The relation of the harmonic emission of each atom must be taken into account, known as *phase-matching* [23, 24]. Along the propagation axis, the phase-mismatch Δk between the generated harmonic field and the laser induced polarization is described by

$$\Delta k = \Delta k_{\text{atom}} + \Delta k_{\text{free electrons}} + \Delta k_{\text{focusing}} + \Delta k_{\text{intensity}} \,. \tag{2.42}$$

The different contributions in Eq. (2.42) consist of the dispersion in a neutral medium Δk_{atom}, the presence of additional free electrons $\Delta k_{\text{free electrons}}$, the influence of the focusing geometry $\Delta k_{\text{focusing}}$ and the intensity $\Delta k_{\text{intensity}}$, also called dipole response.

Using Eqs. (2.41) and (2.42), the spectral and temporal properties of HHG can be optimized by tuning the generation conditions through the driving field and the gas target.

2.8.4 Two-color laser driver

In the following, the conventions and variables used throughout this thesis as well as in **Paper IV** and **V** are introduced in the context of HHG employing a two-color laser driver. In these works, the two colors refer to a fundamental (ω) and its second harmonic (2ω). To define the ratio of the two colors with respect to the total intensity of the combined colors I_{tot}, R is introduced as

$$R = \frac{I_{2\omega}}{I_{2\omega} + I_{\omega}} = \frac{I_{2\omega}}{I_{\text{tot}}} \,. \tag{2.43}$$

R defines the fraction of the intensity of the second harmonic I_{SH} to the total intensity. The resulting, time-dependent electric field can then be written as

$$E(t) = \sqrt{\frac{1}{c\epsilon_0}} \left(\sqrt{(1-R)I_{\mathrm{tot}}} \cos(\omega t) + \sqrt{RI_{\mathrm{tot}}} \cos(2\omega t + \phi) \right) \tag{2.44}$$

where ϕ is the phase offset between the two colors. An illustration of Eq. (2.43) and (2.44) is shown in Fig. 2.16, with the total electric field on the top (black) and its fundamental (red, middle) and second-harmonic contributions (green, bottom).

Applying the three-step model, the right part of Eq. (2.39) can be replaced with Eq. (2.44) and solved numerically, completely analogous to how the trajectories in Fig. 2.13 were obtained.

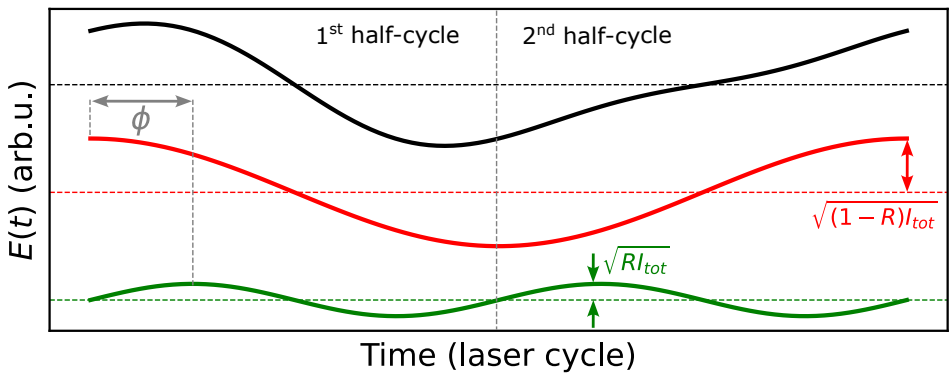

Figure 2.16: Two-color laser field (top, black) consisting of a fundamental with frequency ω (middle, red) and its second harmonic 2ω (bottom, green).

Examples of varying R and ϕ including the resulting electron trajectories and the distribution of return energies E_r vs. their return time T_R are shown in Fig. 2.17.

To the left, the $R = 0$ case is shown for two contributing electric field half-cycles. This situation is equivalent to what is presented for only one half-cycle in Fig. 2.13. Even though the electrons get emitted in opposite transversal direction if $E(t)$ changes sign, the distribution of electrons that do return remains identical, which is the essence of centro-symmetry and the reason for only odd-order harmonics. The gray line in the last row indicates the cutoff according to Eq. 2.41. For $R = 0.2$, I_{tot} remains the same, with a reduced fundamental contribution at ω (red) to compensate for the added second harmonic at 2ω (green). The trajectory distribution, except for the sign difference, now looks very different. In the first half-cycle, for $\phi = \pi/2$ (middle column), E_r is decreased since $|E(t)|$ close to the times of return has a flatter slope than for $R = 0$. However, for the second half-cyle, this effect is reversed with a much faster change of $E(t)$ towards the times of return. Comparing E_r in units of

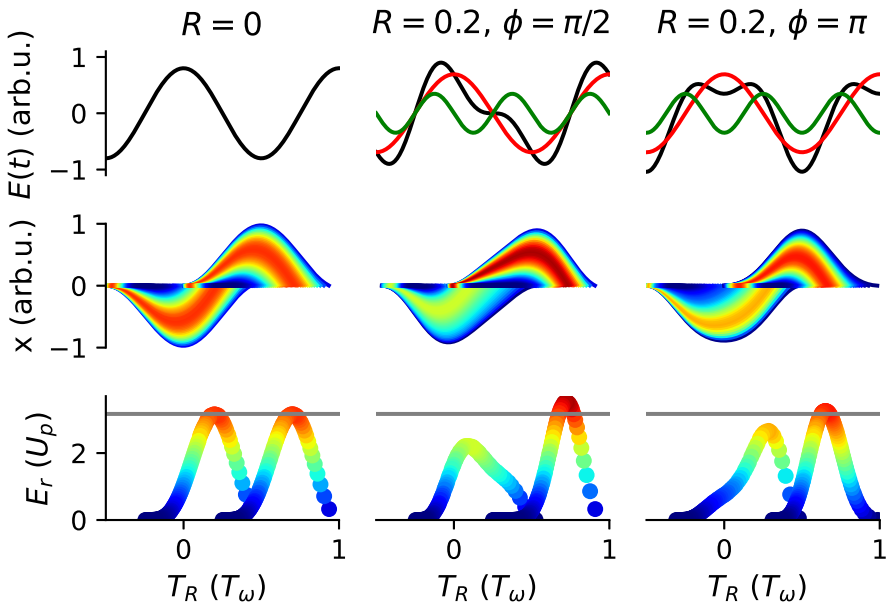

Figure 2.17: Examples for $E(t)$ (top row), trajectories (middle row) and distribution of E_r vs. return time T_R (bottom row) for $R = 0$ (left column), $(R, \phi) = (0.2, \pi/2)$ (middle column) and $(R, \phi) = (0.2, \pi)$ (right column). All three examples were calculated with an identical value for I_{tot}. The grey line indicates the single-color cutoff. Adapted from **Paper IV**.

U_p for $R = 0$, see Eq. 2.40, this leads to an extension of the cutoff. For $\phi = \pi$ (right column), where the peaks of $|E(t)|$ overlap for the second half-cycle, the cutoff reduction in the first half-cycle and the cutoff extension in the second one is still present, just not as dominant.

The effect of this so-called *symmetry break* in the half-cycle contributions for $R \neq 0$ results not only in odd-order, but also in even-order additional harmonic orders. The different distributions for E_r in the last row of Fig. 2.17 strongly indicate a change in spatial, spectral and temporal properties depending on R and ϕ.

Chapter 3

Laser technology for high-harmonic generation

This chapter first provides a comprehensive introduction to the principles behind ultrafast high-power lasers, with a focus on the technology shift from Ti:Sa to Yb and its implications for HHG. Then, post-compression of Yb sources is discussed, presenting an experimental setup and the results of **Paper I**.

3.1 Ultrafast high-power lasers

3.1.1 Basics of lasers

Absorption, spontaneous and stimulated emission are fundamental processes in the interaction between light and matter [40], sketched in Fig. 3.1. If the energy of a photon matches the difference of two levels in an atom, it might be absorbed, lifting an electron from a ground state to an excited state (left). When this electron falls to a lower level, the difference in the energetic states is freed in the form of a photon with the same energy (middle). This process occurs spontaneously, usually after a lifetime τ of the upper state. The emission can also be triggered by a photon with the same energy which will result in the emitted photon having the same direction, energy and polarization (right). These processes are crucial to the working principle of a *laser*, an abbreviation for *Light Amplification by Stimulated Emission of Radiation*, which was successfully demonstrated in 1960 for the first time [41].

For a laser to work, more atoms have to be in the excited state than in the ground

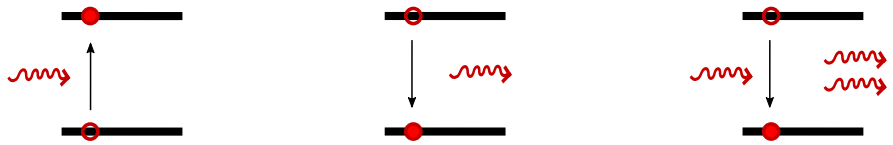

Figure 3.1: The process of absorption (left), spontaneous emission (middle) and stimulated emission (right) illustrated schematically.

state. To obtain this, energy needs to be pumped into the system. This condition, commonly referred to as population inversion, cannot occur in a two-level system, as sketched in Fig. 3.2 (left). Such a system can only be pumped by the same energy as the desired emission transition, which will lead to equal populations in the ground and excited state and thus to no amplification. A minimum of three levels is required, as shown in the middle and right of Fig. 3.2. Hereby, a pump with energy higher than that of the transition of interest is absorbed in the medium. The electrons quickly move to a lower, intermediate state via a nonradiative decay, with this energy difference dissipated as heat. As the intermediate state has usually a long lifetime in comparison to the uppermost state, electrons can accumulate quickly. If these atoms are placed in a resonator, which consists of highly reflective mirrors facing each other, amplification can occur if stimulated emission (gain) surpasses the losses of this resonator. The lower level of the lasing transition does not have to be the ground state, as shown in Fig. 3.2 to the right where a four-level system is presented schematically, with an additional nonradiative decay from the second intermediate state to the ground state.

A laser gain medium can consist of atoms, molecules, liquids, or solids. The two most important properties of a gain medium are its bandwidth, which is the width of the laser levels, defining the achievable pulse duration, and the quantum defect, which is the difference between the pump energy and the laser energy, which is usually transferred into heat.

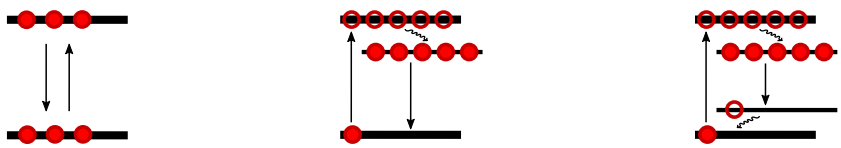

Figure 3.2: Illustration of a two-level system (left), a three-level system (middle) and a four-level system (right).

3.1.2 High power amplification schemes

For high powers, the standard laser amplification scheme described in Sec. 3.1.1 can lead to a few issues. If the peak intensity is too large, the first imminent problem is material destruction, both for the laser medium and for subsequent optics after

amplification. This can be circumvented by applying a large quadratic phase to the pulses, thus stretching the pulse in time to significantly lower the peak intensity before amplification. *Chirped pulse amplification* (CPA) [42] was awarded the Nobel Prize in Physics in 2018 and enabled crucial laser developments for HHG.

For large average powers, the laser gain medium will heat up due to the quantum defect, which is the difference between pump and laser wavelength, causing material deformation and in general instabilities in the optical system due to thermal lensing. Optical parametric amplification (OPA), first proposed in 1962 [43] and experimentally demonstrated in 1965 [44] utilizes virtual energy levels in a nonlinear medium, such as BBO, where the energy of the pump is split into an idler and a signal due to energy conservation. The main advantage of OPA compared to CPA is that the energy difference between the pump and the signal is emitted radiatively without heating involved. Another advantage is the tuning capability in terms of signal wavelength and bandwidth. If operated collinearly, the phase-matching condition, see Sec. 2.7.1, can be changed by varying the crystal angle, to support a signal with varying central wavelength. By operating an OPA noncollinearly (NOPA), due to the additional degree of freedom, the bandwidth, determining the minimum possible pulse duration, can be altered as well [45]. CPA and OPA can also be combined to OPCPA where the signal and pump pulses are chirped, to accommodate high pulse energies [20]. However, since OPA is a nonlinear effect, it is very inefficient. The key differences of CPA and OPA in terms of energy schematics are illustrated in Fig. 3.3.

Figure 3.3: Comparison between chirped pulse amplification (left) with a pump ω_p (green), the quantum defect (black) and signal ω_s (red) and optical parametric amplification (right) with an additional idler frequency ω_i (blue).

3.1.3 From Titanium:Sapphire to Ytterbium-doped systems

Ti:Sa laser systems gained wide popularity in the field of ultrafast science after their invention in 1986 [18], as very short pulses could be generated due the high gain bandwidth of the medium. With the invention of CPA, these laser systems are able to supply pulse energies from several mJ at a few kHz to several J at a few Hz [46].

The absorption and emission spectra of a Ti:Sa laser are shown on the left in Fig. 3.4, including schematics of the relevant energy levels. The central wavelength is often around 800 nm at its peak of the emission cross-section (red), with the most efficient pumping around 500 nm (green). The large emission bandwidth between

600 nm to 1100 nm can support pulse durations down to a few fs [47]. Despite the short pulse duration, Ti:Sa systems are far from ideal: The large spacing between the intermediate levels and the uppermost and ground states gives rise to a very large quantum defect of almost 50 %, leading to a lot of heat inside the material, preventing amplification at high repetition rates above several tens of kHz. In addition, the life-time of the upper intermediate levels is relatively short on the order of µs, which makes pumping with cost-efficient, continuous light sources such as diodes not very effective.

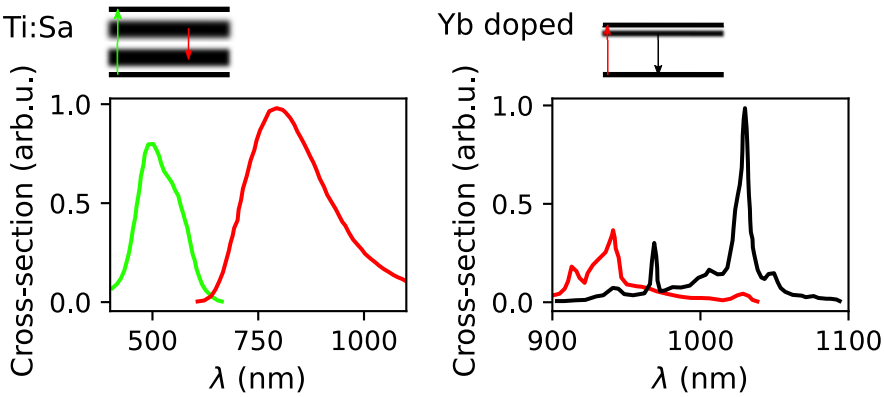

Figure 3.4: Absorption and emission cross-sections for a Ti:Sa (left) [48] and Yb-doped (right) [49] laser medium.

An alternative is Yb-based light sources. The characteristics for Yb-doped glass is shown in Fig. 3.4 on the right. Its gain bandwidth is much narrower than that of Ti:Sa with a peak of the emission cross-section at 1030 nm (black). However, the quantum defect is minimal as the absorption is most efficient around 930 nm (red). As a consequence, Yb sources are often employed in high-repetition rate amplifiers. Due to the longer upper lifetime on the order of ms, efficient pumping is also possible with continuous sources, bringing down the effective operating costs significantly. Yb-based amplifiers can also be used as a pump for high-repetition rate OPCPAs that are based on Ti:Sa to circumvent the limitations of Ti:Sa-only based CPA systems [47]. They can also serve as pump and seed via multiple frequency conversion steps to generate short pulses in the mid-infrared at 2 µm [50]. Yb-doped gain media themselves are very versatile regarding general laser architecture, as the amplifier can be built, e.g. based on a fiber [51], slab [52], thin-disk [53] or rod-type [54], supplying up to hundreds of mJ pulse energy and kW average power pulses at tens to hundreds of kHz [19]. Therefore, the community of ultrafast science is progressively replacing Ti:Sa lasers by Yb-doped systems.

Table 3.1: Overview of the laser systems used in this thesis.

system	rod-type	OPCPA	Pharos	Amphos
front-end	Ti:Sa	Ti:Sa	Yb	Yb
amplifier	Yb rod-type	Yb-pumped NOPA	Yb solid	Yb slab
λ (nm)	1030	800	1030	1030
E (µJ)	170	15	700	8400
t (fs)	300	6	180	1000
f_{rep} (kHz)	200	200	10	1
location	MHz-lab	MHz-lab	d-lab	DESY
Paper	**I**	**II, III**	**IV, V**	**VI**

3.1.4 Ultrashort pulses for HHG

The pulse duration of Yb-doped amplified systems are usually in the few hundreds of fs to ps range [19]. Generating HHG with such "long" pulses is possible, as the three-step model suggests that only peak intensity and central wavelength determine tunnel ionization and electron acceleration (see Sec. 2.8.1). However, efficiently compressing these pulses to shorter durations can enable higher peak intensities, enabling higher XUV energies in return. In addition, shorter pulses will lead to a higher HHG efficiency as fewer half-cycles contribute to the overall degree of ionization.

From an application point of view, HHG with short pulses also has a number of advantages. Due to a lower number of contributing electric field cycles and therefore less interference, the spectral width of the individual high harmonics becomes larger, allowing multiple energy levels to be excited at once. In the extreme case, where only one cycle contributes, isolated attosecond pulses with a continuous XUV spectrum can be generated, which is beneficial for some applications to probe the attosecond dynamics in atoms and molecules [3, 55].

Reducing the pulse duration of Yb-based systems efficiently to still benefit from the advantages of simultaneous high peak power and high repetition rate has therefore become an active research subject, called *post-compression*.

3.1.5 Laser systems used in the scope of this thesis

In Table 3.1 an overview of the laser systems used within the thesis work and the related publications is given, in terms of front-end, amplifier system and pulse parameters (central wavelength λ, pulse energy E, pulse duration t, repetition rate f_{rep}). The first three laser systems are located in Lund at the high-power laser facility, in the high-repetition-rate "MHz-lab" and in the development-lab (d-lab). The last system is located at the Deutsches Elektronen-Synchrotron (DESY) in Hamburg, Germany.

3.2 Post-compression using bulk multi-pass cells

In this section an overview of the principles behind post-compression is given before focusing on one experimental implementation, i.e. bulk multi-pass cells, which is the subject of **Paper I** and **Paper VI**.

3.2.1 Introduction to post-compression

Post-compression is a technique often employed to shorten the duration of laser pulses after they have been amplified [21]. The basic principle is illustrated in Fig. 3.5.

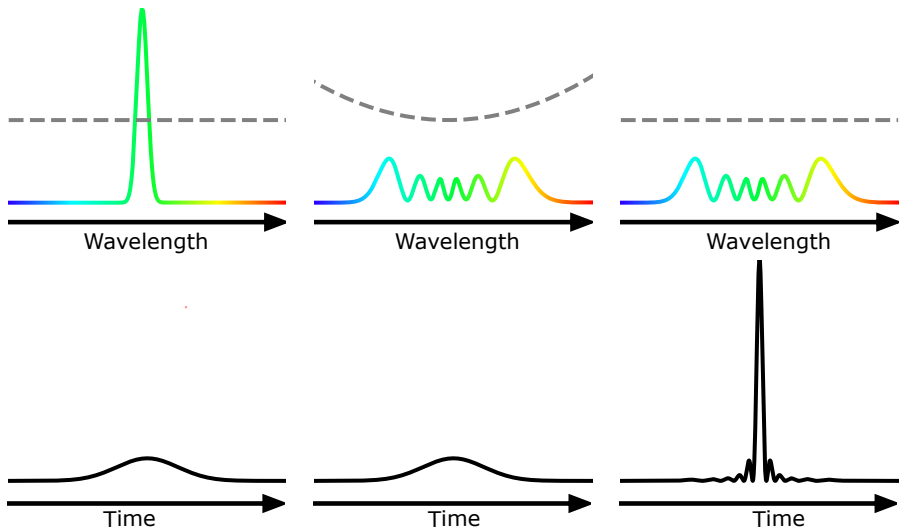

Figure 3.5: Illustration of post-compression. The spectrum gets broadened from left to the middle due to self-phase modulation, a short pulse (right) is reached if the chirp is removed.

It starts with a pulse that is narrow in spectrum (top left) and long in time (bottom left), typically with a flat spectral phase, as illustrated by the dashed line on the upper left. After sending the laser into a Kerr-medium, such as a nobel gas or bulk material, often multiple times depending on the scheme being used, the spectrum gets broadened due to self-phase modulation, leading to a dominant quadratic spectral phase term (top middle). The spectral phase can be removed to compress the pulse in time as close to its Fourier transform limit as possible, as illustrated on the right of Fig. 3.5, resulting in a significant increase in peak power.

3.2.2 Overview of methods

Many different methods exist for spectral broadening, comprehensively reviewed in [21]. In this section, the most important and established ones are presented with their advantages and drawbacks, before discussing methods for dispersion management after spectral broadening.

Waveguides

A well-established technique is based on guiding systems, such as fibers with a solid core [56] or gas-filled hollow-core [57], in which propagation below the critical power for self-focusing (see Eq. (2.37)) introduces self-phase modulation in the fiber. Such waveguides were historically implemented already for Ti:Sa systems to reach shorter pulse durations towards the few-cycle limit [58]. Due to their mode-preserving properties, the spatial beam quality in the output beam is exceptional [59]. However, this makes waveguide-based post-compression systems extremely alignment sensitive. Scaling waveguides to their desired peak and average powers can be done easily by the mode-size, length and gas pressure. Ti:Sa [60] as well as Yb-based lasers [61] with several tens of mJ reaching TW of peak powers after compression were successfully demonstrated, with the drawback of having very large experimental setups spanning lengths of several meters.

Free-space optics

A quasi-waveguide can also be created using free-space optics, utilizing self-focusing which is the byproduct of spectral broadening. In multi-plate compression schemes a beam is focused just before thin glass plates which then refocus the diverging beam to create a self-guiding effect in a series of plates [62]. This principle is illustrated in Fig. 3.6 on the left. With this approach, compression of an Yb-based laser down to the single-cycle could be demonstrated [63]. However, energy scaling using this technique is limited as it is based on bulk material where beam collapse and damage thresholds become an issue, as the peak power has to exceed the critical power of the material by > 100 times to introduce such a strong self-focusing. In addition, spatial chirp can accumulate as the plates are introduced at the Brewster angle to minimize reflection losses [64]. As the peak power has to be very large, the B-integral (see Eq. (2.38)) and thus the spectral broadening per plate will be as well.

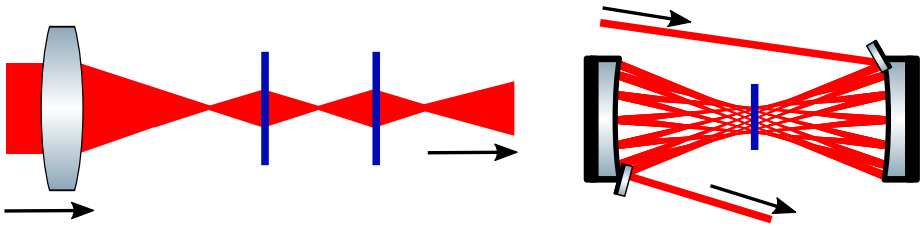

Figure 3.6: Beam guiding of multi-plate compression (left) vs. multi-pass cells (right).

To relax the B-integral accumulation, multi-pass cells (MPCs) were introduced for the first time in 2016 for post-compression purposes [65]. The concept of MPCs itself is not new. Arranging mirrors in a way so that a laser beam passes many times between them to enhance the path length in a compact manner was originally suggested for spectroscopy purposes in 1942 to increase the amount of absorption [66]. Herriott et al. discovered a clever configuration with two curved mirrors where the beam on the mirrors traces a circular pattern [67], which became the basis for the majority of post-compression MPCs. The beam is focused repeatedly between the two mirrors, thus the B-integral per pass can be much smaller than in the multi-plate regime to achieve the same final broadening. The concept of an MPC is illustrated in Fig. 3.6 on the right. For input peak powers of up to several tens of MW, bulk in the form of one or several glass plates can be the medium of choice for the Kerr-effect to occur. Above these values, where unwanted self-focusing and optical damage become a limiting factor, MPCs filled with a gas and operated below the critical power can be advantageously uesd [68, 69]. Similarly to waveguides, MPCs scale proportionally in size to the laser parameters used. For example, a 10 m long gas-filled MPC for compression of an Yb thin-disk laser with pulse energies of 200 mJ was demonstrated in 2023 [70]. The greatest advantages lie in power efficiency (up to 96 % transmission [71]), the robustness to pointing instabilities and the possibility to accumulate a large total B-integral [72, 73]. Often built from standard optical components, the MPC geometry as well as the nonlinear media can be easily adjusted for the desired parameter space, as reviewed by Viotti et al. as well as Hanna et al. [22, 74]. A large drawback is the limitation in achieving few-cycle pulses efficiently, as the reflectivity of the mirrors decreases proportionally with their supported bandwidth, which can lead to reduced transmission values if a large number of mirror bounces is required.

Dispersion management

The schemes mentioned above are commonly used only for the spectral broadening aspect of post-compression. To achieve the actual compression, the positive dispersion caused by self-phase modulation has to be removed accordingly to achieve a flat

spectral phase. Introducing negative dispersion practically means that the red, longer wavelength part of the spectrum travels a further distance than the blue, shorter wavelength part. The two most common methods for achieving this in a laboratory are illustrated in Fig. 3.7. On the left, dispersive multi-layer mirrors are shown schematically. The coating layers are designed in such a way that longer wavelengths penetrate the coating deeper than shorter ones before being reflected [75]. Chirped mirrors usually have a high reflectivity $> 99.5\,\%$ but are designed for a specific central wavelength, bandwidth, and a fixed amount of negative GDD per bounce.

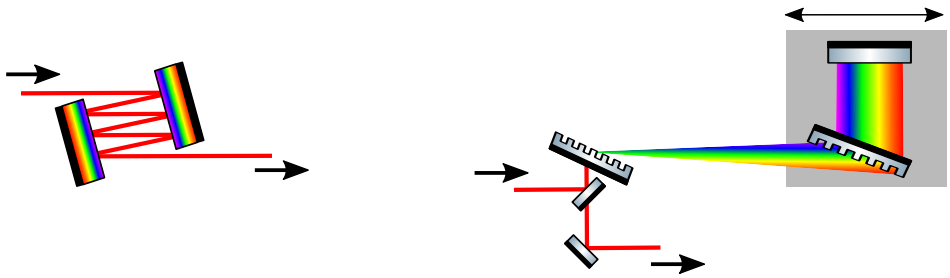

Figure 3.7: Practical dispersion removal with chirped mirrors (left) and a grating compressor (right).

A more flexible but also much more alignment sensitive solution is a grating compressor [76], with a possible implementation shown to the right in Fig. 3.7. The beam is dispersed in wavelength by the first grating, is then transmitted through the second grating and reflected back by a retro-reflector, sending all colors back on an identical path but vertically offset to the input beam to undo the spatial chirp. The amount of negative GDD that is introduced can be tuned by changing the distance between the gratings, enabling a continuous tuning of the second-order spectral phase.

For a few post-compression schemes, broadening and dispersion management can be combined into one step, called self-compression. For example, this can be achieved by working in the anomalous dispersion regime where propagating through material introduces a negative GDD [77], or by employing dispersive mirrors inside an MPC [78]. It can also happen in the nonlinear medium itself, due to complex nonlinear dynamics during ionization, shown in hollow-core fibers [79] as well as in filamentation [80].

Most commonly employed post-compression solutions

The most common pulse parameters covered by MPCs and fibers in terms of output peak power, average power, pulse energy, and pulse duration are shown in Fig. 3.8.

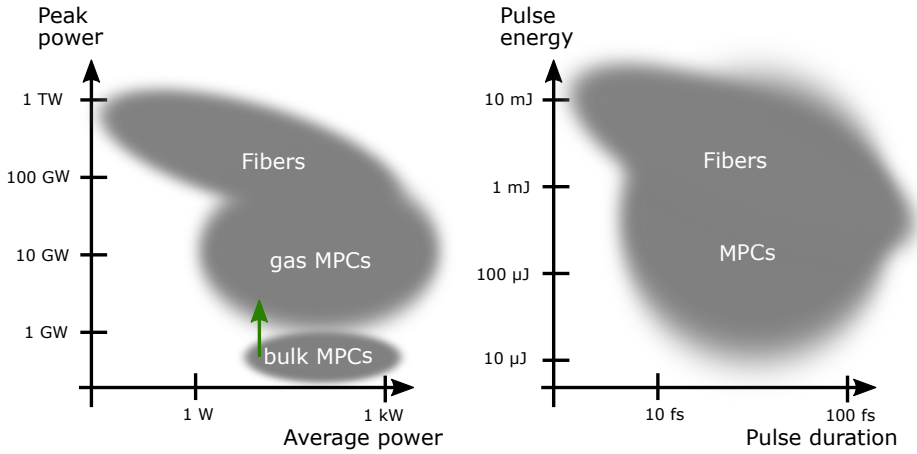

Figure 3.8: Most commonly used parameter space for post-compression schemes. The green arrow represents the research efforts presented in this thesis. Illustration adapted from [21] and [22].

This figure presents the general trend, given by practical limits, such as availability due to establishment of the method, setup size, and costs. The green arrow represents the direction of current research discussed in this thesis. Bulk MPCs have the large advantage of cost efficiency and footprint compared to gas MPCs as they do not require expensive vacuum installations. The goal of **Paper I** is to push this technology to the GW peak power regime where mostly gas MPCs are employed to this date. In general, MPCs offer a great scaling potential, which will be further explored in the next section.

3.2.3 Multi-pass cells

In the following, an introduction to the concepts necessary for the design of MPCs is given.

Geometrical design

The properties of a multi-pass cell regarding beam caustics and stability follow the same principles as a resonator, or cavity. When a beam with the complex beam parameter q_{in} enters a cavity and performs one round trip, the beam should have the exact same focus size and position as well as wavefront curvature described by q_{out} as before. Any resonator desgin can be described by a roundtrip-ABCD-matrix, with

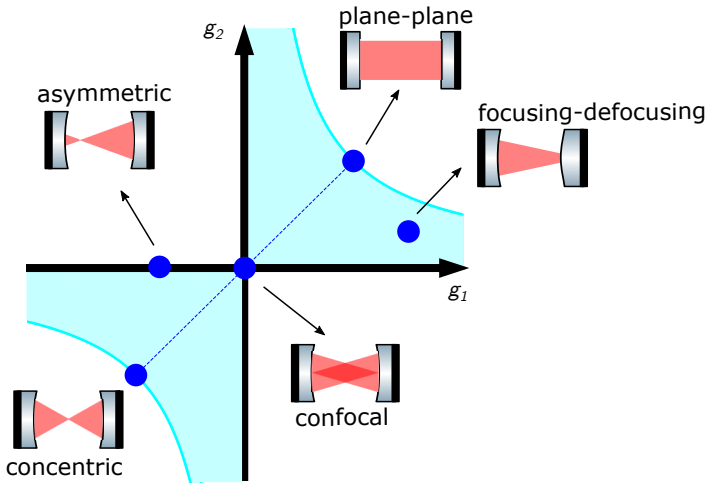

Figure 3.9: Stability landscape of different resonators. All resonators in the light blue shaded area are stable. The dashed dark blue line represents resonators where the radii of curvature are identical. Herriott-cells typically lie on the lower half of the dashed line.

the self-replication criterion

$$q_{\text{out}} = \frac{Aq_{\text{in}} + B}{Cq_{\text{in}} + D} = q_{\text{in}} \,. \tag{3.1}$$

To describe the beam at any point in the resonator, this equation can be solved for q_{in}, the so-called *eigenmode*.

For a standing wave cavity, described by two mirrors with curvatures R_1 and R_2 separated by a distance L, it is helpful to introduce the stability parameters g_1 and g_2 as

$$g_1 = 1 - \frac{L}{R_1} \,, \tag{3.2}$$

$$g_2 = 1 - \frac{L}{R_2} \,, \tag{3.3}$$

to describe Eq. (3.1) in a much simpler fashion, with the so-called stability criterion:

$$0 \leq g_1 g_2 \leq 1 \,. \tag{3.4}$$

A visual representation of Eq. (3.4) is given in Fig. 3.9. The light blue shaded area covers all stable configurations of standing-wave resonators. A few special cases are high-

lighted with dark blue dots. Along the dashed dark blue line, where $R_1 = R_2 = R$ the most commonly used designs for resonators are found.

A Herriott-cell is a special case of a multi-pass cell, where the beam bounces back and forth along a circular pattern performing a number of N roundtrips [67]. For each round-trip, the beam moves further in the circle by an angle ξ, described by the Herriott equation

$$\xi = \frac{2\pi k}{N}, \text{where } k = 1, \ldots, N-1\,. \tag{3.5}$$

In practice, the angular advance of ξ per pass from one mirror to the other corresponds to the Gouy phase shift (see Eq. (2.19)) that the beam undergoes, which depends on the refocusing properties of the MPC. The stability criterion in Eq. (3.4) can be further expressed as

$$0 \leq L \leq 2R\,, \tag{3.6}$$

which is represented in Fig. 3.9 by the lower part of the dashed line with its extreme cases of a concentric resonator on the lower end, where $R = L/2$, and a confocal resonator ($R = L$) in the center of the figure. An example close to the concentric case is shown in Fig. 3.10, which highlights the regular pattern from the side (top) and on the mirrors (bottom).

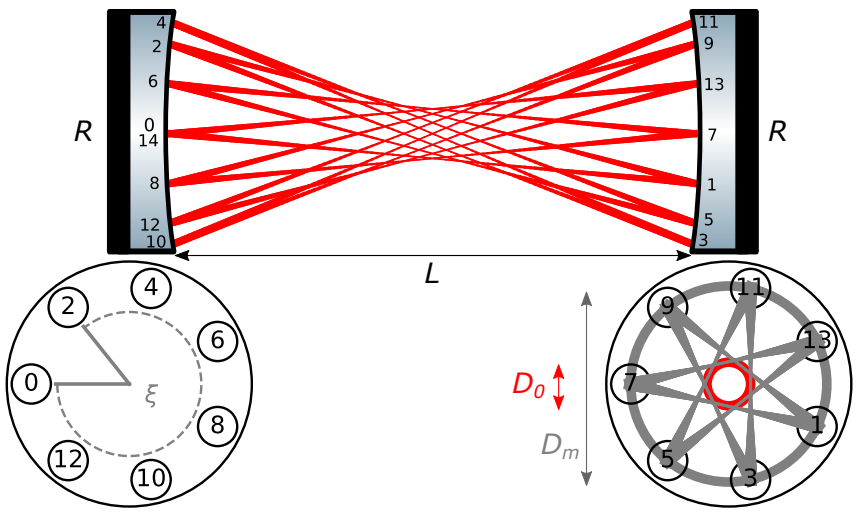

Figure 3.10: Side-view of a standard MPC (top), built from two mirrors with $R_1 = R_2 = R$, separated by the distance L. The numbers on the mirrors indicate the indices of the passes. On the mirrors, the laser beam has the width w_m, in the focus w_0. Mirror-view of a standard MPC (bottom). The phase advance ξ is illustrated on the left by the angle between two consecutive spots on the same mirror. The other geometrical properties of the beam pattern inside the MPC are illustrated on the right with the corresponding beam pattern projected on it, with the diameter of the pattern ring on the mirror D_m and the minimum diameter the pattern forms in the middle of the MPC, D_0, marked in red.

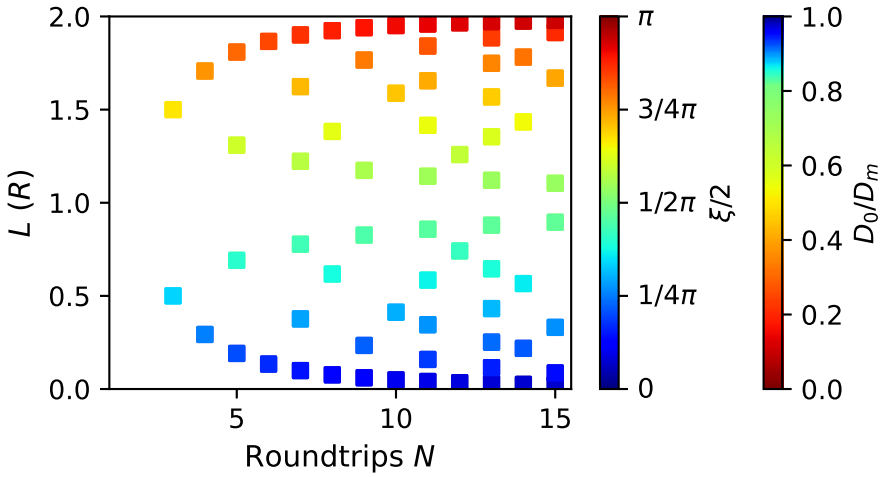

Figure 3.11: Possibilities for the quantized solutions depending on the number of roundtrips N and the mirror distance L in units of R. The color of the solutions corresponds to both the phase advance to the next mirror $\xi/2$ and to the relation between inner and outer pattern diameter D_0/D_m.

The numbers on the mirrors correspond to the indices of the bounces for $N = 7$ roundtrips. The view on both mirrors is shown in the bottom of Fig. 3.10, highlighting the angular advance ξ on the left. On the right, the red pattern shown on the top in Fig. 3.10 is projected onto the mirror (grey). Except for the beam properties with its smallest beam size w_0 in the focus and largest beam size w_m on the mirror, the diameter of the pattern itself can be another property of interest. The outer diameter D_m, which is the pattern on the mirror, can be freely chosen, only limited by the mirror size and separation of the spots on the mirror. The inner diameter D_0, indicated in red on the bottom right of Fig. 3.10, scales with D_m according to a factor determined by the geometry of the cavity.

The possible solutions to the Herriott equation Eq. (3.5) are quantized, and are shown in Fig. 3.11 for a fixed radius of curvature. Each cell with length L has a unique number of roundtrips for which Eq. (3.5) is fulfilled. This figure only shows the solutions up to $N = 15$. For $L \to 2R$ values the phase advance for one roundtrip approaches a full circle. In practice, this means that the beam goes from the one side of the first mirror to the almost opposite side of the second mirror.

For $L \to 0$ there is barely any phase advance with the beam going straight to the opposite mirror with only a very small angle. The consequence is an inverse relationship between the well-correlated L and ξ and the diameter of the entire pattern in the focus D_0, as indicated by the second colorbar in Fig. 3.11.

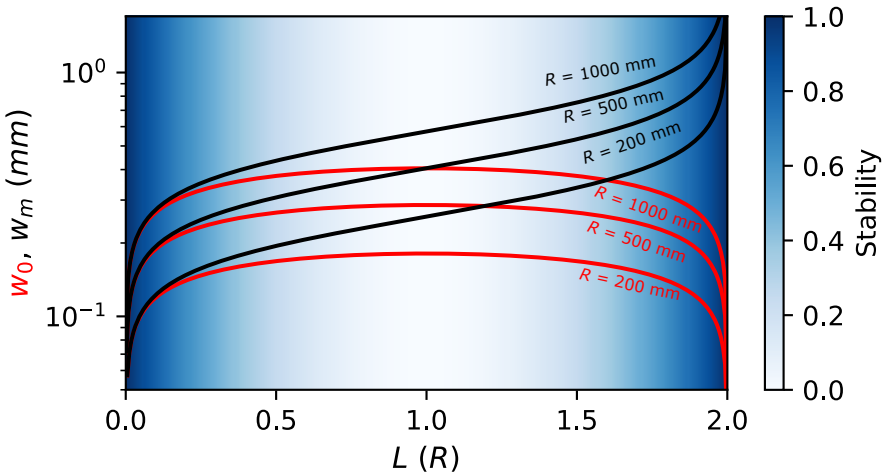

Figure 3.12: Evolution of the beamsize on the mirror w_m (black) and in the focus w_0 (red) for different mirror curvatures. The stability $g_1 g_2$ scales independently of the chosen R and is shown in the background colormap.

The beam sizes on the mirrors w_m and in the focus w_0 also depend heavily on the geometry chosen. By finding the eigenmode q depending on R and L and propagating q to the center of the cell and mirrors [26], w_0 and w_m can be obtain. They can be expressed as

$$w_m = \sqrt{\frac{\lambda}{\pi}\sqrt{\frac{LR}{2} - \frac{L^2}{4}}} \tag{3.7}$$

and

$$w_0 = \sqrt{\frac{\lambda R}{\pi}\sqrt{\frac{L}{2R - L}}}\,. \tag{3.8}$$

For a few values of R and a wavelength of $\lambda = 1030\,\mathrm{nm}$, the beam radii w are plotted in Fig. 3.12 following equations (3.8) (red) and (3.7) (black). The stability value, $g_1 g_2$ according to Eq. (3.4) is shown in the background color. The longer the cell ($L \to 2R$), the more w_0 and w_m deviate from each other.

Any MPC must be operated with the peak fluence F_{peak} below the mirror damage threshold, with

$$F_{\mathrm{peak}} = \frac{2E}{\pi w_m^2}\,. \tag{3.9}$$

For this reason, designs towards $L \to 2R$ are often chosen.

Nonlinearities in MPCs and mode-matching

To achieve spectral broadening, a Kerr medium has to be inserted into the MPC for self-phase modulation to occur. Typically, either plates of bulk glass, such as fused silica are used, or the MPC is built inside a chamber that can be filled with gas, such as argon or neon. Both possibilities are illustrated on the top in Fig. 3.13. The nonlinearlity in a gas MPC (left) can be tuned by pressure p and the gas species, defining n_2. In a bulk MPC (right) the nonlinearity is affected by the material, thickness, and location in the cell as well as by the number of inserted plates. On the right in Fig. 3.13 a symmetric configuration of two plates with thickness d and spacing L_{plate} is presented.

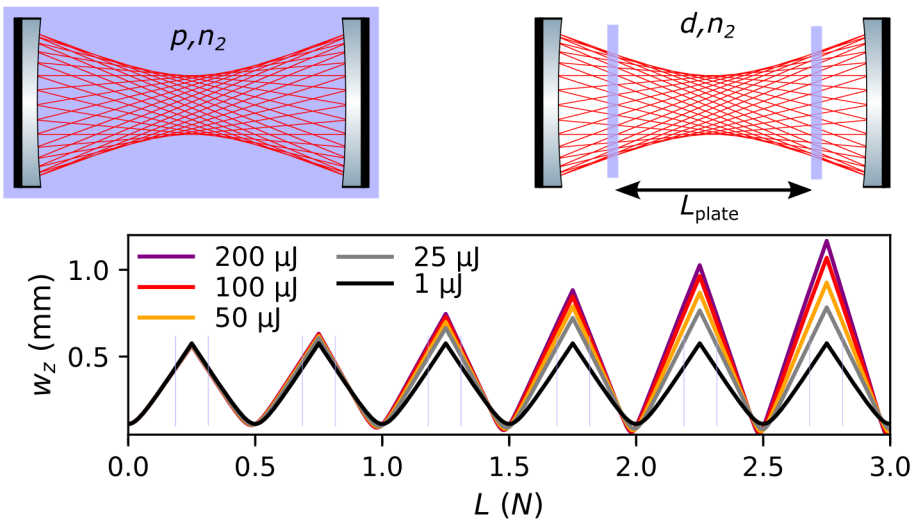

Figure 3.13: Kerr media in MPCs, a gas with pressure p and nonlinear index n_2 (top left) and bulk plates, with thickness d, nonlinear index n_2 and spacing L_{plate} (top right). Change of beam size in a bulk MPC for different pulse energies (bottom).

The main difference between gas and bulk lies on the order of magnitude of n_2. For a gas, n_2 is pressure dependent [81] but usually in the order of $10^{-19}\,\text{cm}^2/\text{W}$ for argon and neon, while for bulk, n_2 is a material constant and four orders of magnitude stronger in the case of the material most widely used, fused silica, with $n_2 = 2.8 \times 10^{-16}\,\text{cm}^2/\text{W}$ at $\lambda = 1030\,\text{nm}$ [22]. As gas MPCs are filled homogeneously, operation beyond the critical power for self-focusing is not possible, as immediate beam collapse would occur. Bulk MPCs have the advantage to be operated far beyond the critical power ($\approx 4\,\text{MW}$ for fused silica [82]) as the plates can be significantly thinner than the length required for beam collapse [34].

To operate an MPC, the input beam must be matched to the eigenmode of the cavity. Usually, this is done with a lens or a mirror telescope, by calculating the expected focus size from Eq. (3.7). However, the equations governing the beam sizes inside an MPC (Eq. (3.7) and (3.8)) are only valid in the absence of self-focusing nonlinearities.

As spectral broadening and self-focusing go hand in hand, taking these effects into account when matching the input beam to the eigenmode of the cavity might be necessary. For MPCs that are homogeneously filled with gas, as shown in the top left of Fig. 3.13 this effect is often negligible [74, 83], as they are always operated below the critical power (see Eq. (2.37)) to avoid beam collapse. Thus, the gas pressure p can easily be adapted to accommodate this limitation. For bulk MPCs, the peak power can exceed the critical power as d is chosen to be small enough for an actual beam collapse to not occur. However, it may modify the eigenmode of the cavity as the thin plates act as lenses, according to Eq. (2.36) [74].

In the bottom of Fig. 3.13, the radius of the beam w_z is plotted for several roundtrips with a symmetric fused silica plate configuration, as shown in Fig. 3.13 to the right, with $d = 1\,\mathrm{mm}$, $L_{\mathrm{plate}} = 230\,\mathrm{mm}$, $L = 385\,\mathrm{mm}$ and $R = 200\,\mathrm{mm}$ for Gaussian pulses with a pulse duration of $180\,\mathrm{fs}$. The beam size was calculated using the $ABCD$-matrix formalism (see Sec. 2.4), treating the plates as lenses with intensity-dependent focal length, applying Eq. (2.36). At low energies (black), the cavity behaves perfectly linearly. However, as the pulse energy increases, the lensing effect of the fused silica plates becomes more and more significant, leading to small changes in focus position and size in the first roundtrip that quickly escalate in subsequent roundtrips. In the worst case, this can lead to a focal spot on the mirrors, causing damage. For this reason, the mode-matching needs to be adapted to the new, energy-dependent eigenmode of the MPC.

Nonlinear mode-matching itself is challenging experimentally, as the alignment of the optics is usually conducted at low powers where self-focusing does not play a role. Careful calculations of the beam size and position at low powers for an optimally mode-matched nonlinear cavity have to be carried out [73].

Input peak power scaling of bulk MPCs

Bulk MPCs are traditionally operated at peak powers up to tens of MW (see Fig. 3.8) due to concerns of self-focusing and optical damage. Thanks to the numerous advantages compared to gas MPCs, including simplicity and cost- and space-efficiency, investigating the scalability of bulk MPCs towards higher peak powers is of great interest to the community.

In the first bulk MPC compression experiments, one or two thick fused silica plates on the order of $d \approx 10\,\mathrm{mm}$ are introduced in the center of the cell [84–89]. Soon after, concerns about beam quality were raised when exceeding the critical power for fused silica multiple times, leading to plate-positioning significantly away from the geometrical focus [77, 90]. In addition, exceeding P/P_{crit} by a factor > 50, small scale self-focusing and multi-filament breakup can occur [34]. For this supercritical self-focusing regime, Seidel et al. demonstrated in 2022 that using multiple thin plates instead of larger thick plates, distributed throughout the cell, allows cleaner compression and excellent spatio-spectral homogenity [91]. This result led to further investigations of the input peak power limits for bulk MPCs.

Experimental bulk setup towards the multi-gigawatt peak power regime

Following the reasoning of Seidel et al., that multiple thin bulk plates distributed throughout the cavity will allow for clean broadening compared to a single thicker plate to achieve the same nonlinearity [91], an experimental setup was designed, presented in **Paper I** and Fig. 3.14.

This setup is used to post-compress the output of an Yb rod-type amplifier with a pulse length of 300 fs and a peak power of 370 MW, at a central wavelength of $1030\,\mathrm{nm}$ and a repetition rate of 200 kHz. With these pulse parameters, shown at the top of Fig. 3.14, MPCs are usually operated with gas, see Fig. 3.8.

This input beam is mode-matched via a lens telescope into a cell, illustrated in the middle of Fig. 3.14. With a length of $L = 500\,\mathrm{mm}$ and a mirror curvature of $R = 300\,\mathrm{mm}$ this cavity is rather close to the center of the stability regime (see Fig. 3.12), where the difference between focus size w_0 and mirror beam size w_m is not very large, avoiding ionization in the center of the cavity while still staying below the damage threshold of the mirrors. Two thick fused silica plates with a thickness of $d = 1\,\mathrm{mm}$ are separated by $L_{\mathrm{plate}} = 15\,\mathrm{cm}$ broaden the spectrum during $N = 15$ roundtrips to a Fourier transform limit of 30 fs. Two pairs of chirped mirrors compensate the quadratic spectral phase curvature, resulting in output pulses of 31 fs at a peak power of 2.5 GW with a total power transmission of $> 87\,\%$. The spectral and temporal characteristics of the output pulses are shown in the bottom of Fig. 3.14. The reached peak power is significantly lower than the Fourier-limited peak power of 4 GW due to a pre-pulse located 1 ps before the main pulse.

At the date of publication, this work constituted the highest input and output peak power used in bulk, with $P/P_{\mathrm{crit}} > 80$. Previous works operate in a lower, but similar regime, with input values of 240 MW [89] and 280 MW [77], exceeding the critical power of fused silica by a factor of 55 and 65, respectively. While a good temporal

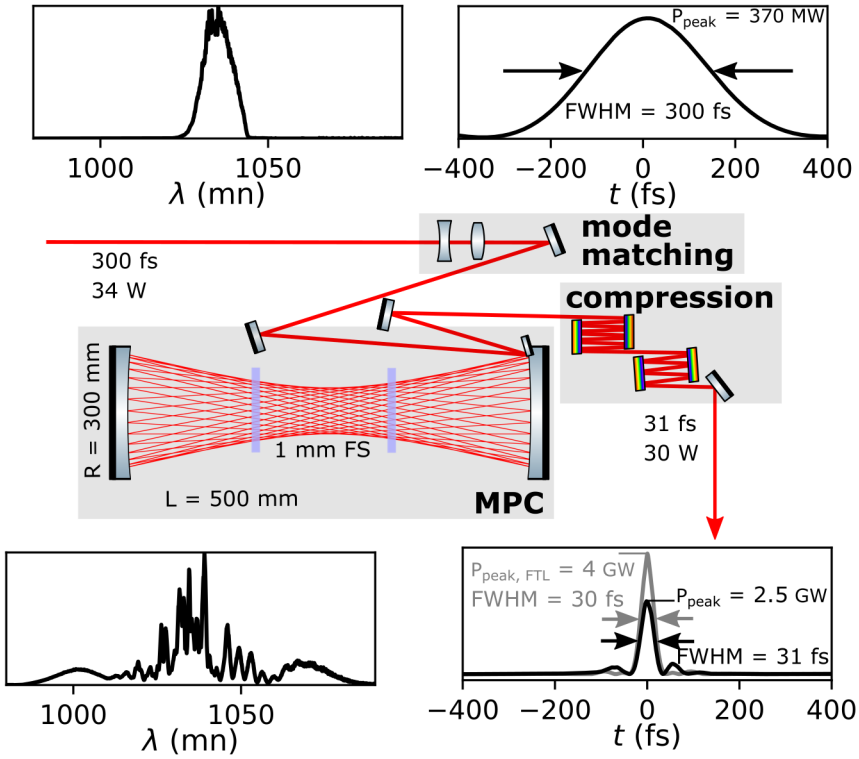

Figure 3.14: Experimental setup (middle) to broaden and compress 300 fs pulses (top) to 31 fs (bottom).

contrast is proven in both cases, a full spatio-temporal characterization was missing, which would indicate if operating a bulk MPC > 50 times above the material's critical power leads to a degradation in pulse and beam quality [34, 74].

For this reason in **Paper I**, a full spatio-temporal characterization is performed, showing no signs of significant beam degradation. The results are shown and discussed further in Chapter 4. Later works demonstrated that even with larger input pulse peak powers > 1 GW a good beam quality can be maintained [92, 93]. Thus, as long as MPCs are operated below damage threshold of optical components, the geometry is chosen to avoid high beam intensities in the center due to ionization, and the plate thickness is significantly shorter than the beam collapse length, efficient and simple bulk MPCs can be employed.

Alternative MPC geometries for output peak power scaling

For applications, scaling the output peak power of an Yb system using MPCs is of major interest. This can be achieved by either shorter pulses or higher output pulse energies. Reducing the pulse duration is possible down to the single-cycle duration, which is the technical limit. Sub-2-cycle pulses were demonstrated after a two-stage MPC setup, using an Yb fiber amplifier with a duration of 260 fs. The transmission was only 60 % due to the decreased reflectivity of the mirrors supporting the required spectral bandwidth [94]. When scaling the pulse energy into the MPC, the peak fluence on the mirrors (see Eq. (3.9)) must stay below the damage threshold of the optics. Often a configuration close to the confocal point ($L = 2R$) is chosen, as the beam on the mirrors is large (see Fig. 3.12). On the other hand, one wants to avoid a too small beam in the center of the cell, as unwanted ionization can occur. Of course, a larger radius of curvature can be chosen for the mirrors, scaling not only the beam sizes, but also the overall length of the setup, which was demonstrated for a 10 m long setup for 200 mJ pulses [70]. However, this is often not a practical solution.

For bulk MPCs, ionization at high peak powers can be tackled by evacuating the volume between the plates. The plates hereby serve as the windows of a small piece of vacuum tube. This is realized in a setup similar to the one presented in **Paper I** and Fig. 3.14. Currently, this is ongoing work with results published soon [95].

A different approach is to use an MPC with a virtual focus outside the cavity, which can be achieved by a geometry that lies on the upper-right side of the stability map in Fig. 3.9. To maintain a relatively large beam throughout the cell, a concave-convex mirror configuration can be used, as shown on the left in Fig. 3.15. Already suggested in 2017 [96] and first demonstrated in a proof-of-principle experiment [97] and shown for up 2 mJ pulses later in 2023 [98], this scheme was shown to work very well, also in direct comparison with an equivalent concave-concave mirror configuration in bulk [97].

Figure 3.15: Examples for power scaling, with a concave-convex setup (left) and beam folding (right).

Another approach is beam folding in a bowtie-like configuration, which was first sug-

gested in 2022 [99] and experimentally demonstrated in **Paper VI** for $8\,\mathrm{mJ}$ pulses. Hereby a geometry with $L/R < 1$ is chosen, approaching the plane-plane configuration in Fig. 3.9 along the dashed line, with only a small beam size difference between the focus and the mirror. The beam is close to a collimated beam. Two large plane mirrors fold the beam 9 times, reducing its original length from $L = 9\,\mathrm{m}$ to a compact setup length of $0.5\,\mathrm{m}$. This setup is schematically illustrated on the right in Fig. 3.15. For $N = 11$, this setup has a total of 550 reflections on mirrors which raises questions about maintaining the beam quality and large power throughput. In this thesis, we show that such a setup does not degrade the beam quality significantly, as further discussed in Chapter 4.

Perspectives for HHG

Yb lasers combined with MPCs are a very promising driver for HHG as they allow for high peak power pulses even at high repetition rates. Many applications benefit from this due to favorable statistics, such as photoelectron spectroscopy [100], coincidence detection [101] or XUV imaging for fundamental research [102] and industrial applications [5], drastically shortening measurement times, improving stability and reproducibility.

As the nonlinearity inside an MPC can be easily adjusted to the desired output pulse duration, MPCs also provide a flexible driver for HHG research itself, for example, to determine the best laser parameters for HHG [24].

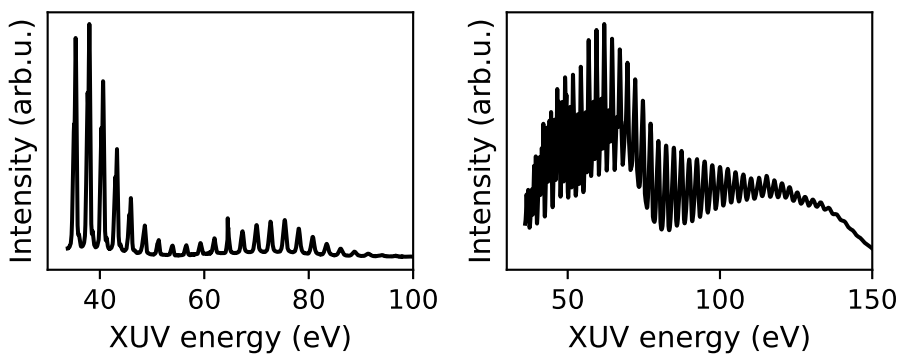

Figure 3.16: High-order harmonics in argon (left) and neon (right) with the MPC output pulse shown in Fig. 3.14 as a driver, using the generation chamber described in [101].

As a proof-of-principle experiment, the MPC output pulses delivered at a repetition rate of 200 kHz and presented in Fig. 3.14 were used in combination with the HHG

setup presented in [101]. The results are shown in Fig. 3.16, for generation in an argon (left) and neon (right) gas target, which consists of a jet from a nozzle with a diameter of 42 µm. The power after the MPC, which is 30 W, is reduced to 7 W as the focusing geometry in this chamber is fixed to an off-axis parabola with $f = 50\,\mathrm{mm}$. Higher powers would lead to a too large degree of ionization in the gas, causing XUV depletion.

Chapter 4

Characterization of ultrashort laser pulses

Proper characterization of ultrashort laser pulses is pivotal in ultrafast science. In this chapter, the most important characterization methods that were employed throughout the research leading to this thesis and the attached publications are introduced, including spatial, temporal, and spatio-temporal diagnostics. Special emphasis is put on two independent pulse characterization projects, for measuring the time-dependent polarization state of a pulse (**Paper II**) and for single-shot CEP detection via optical Fourier transform (**Paper III**).

4.1 Spatial beam quality

To assess the performance of a laser system, it is essential to describe the spatial beam quality. In this section, conventions for beam size measurements, the M^2 method and waveform retrievals are introduced.

Often, a laser beam is assumed to be Gaussian, following the equations described in Sec. 2.4. The size of the beam then refers to the distance where w reaches $1/e^2$ of its peak intensity value. For more complex beams that are not perfectly Gaussian, fitting Eq. (2.15) to extract the $1/e^2$ width is no longer a suitable measurement. Therefore the 4σ width is introduced, referring to the second-order statistical moment of a distribution [103]. In the x direction, it is defined as

$$4\sigma = 4\sqrt{\frac{\int_{-\infty}^{\infty}\int_{-\infty}^{\infty} I(x,y)(x-\bar{x})^2 dx\,dy}{\int_{-\infty}^{\infty}\int_{-\infty}^{\infty} I(x,y) dx\,dy}} \tag{4.1}$$

with $\bar{x}$ being the center of mass in the same dimension.

To determine the degree of variation from a perfect Gaussian beam, the M^2 parameter can be used [104]. The M^2 is a scalar value, extending Eq. (2.16) to account for deviations in $w(z)$. Hereby, $w(z)$ is not referring to the $1/e^2$ radius, but to the 2σ value (see Eq. (4.1)):

$$w(z)^2 = w_0^2 + \left(M^2\right)^2 \left(\frac{\lambda}{\pi w_0}\right)^2 (z - z_0)^2 \,. \tag{4.2}$$

Experimentally, a laser beam is focused by a lens or mirror and its beam profile is acquired at different distances z, where z_0 refers to the geometrical focus, sketched in the bottom of Fig. 4.1.

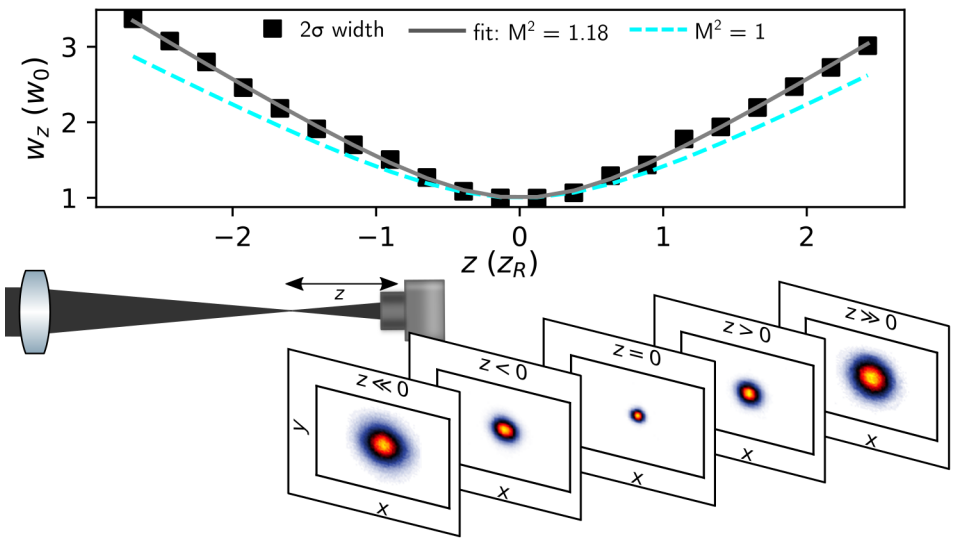

Figure 4.1: Experimental setup to measure the M^2 value of a laser beam (bottom) with an exemplary measurement result (top) from the bulk MPC in Fig. 3.14. The same setup can also be used to acquire data to perform wavefront retrieval.

Equation 4.2 can then be fitted (grey) to the experimentally-determined second order moments (black squares), with M^2, w_0 and z_0 as fit parameters.

Although the value M^2 is often used as the sole measure of beam quality, its interpretation must be carefully considered, especially for $M^2 > 1.5$ due to its high sensitivity to outliers.

If an M^2 measurement is evaluated for different axes perpendicular to the propagation, simple aberrations, such as astigmatism, can be diagnosed, e.g., if the beam

along x and y focuses at different z positions. To retrieve more complicated wavefront aberrations, computational methods are needed.

The most famous example is the Gerchberg-Saxton algorithm, demonstrated in 1972 [105]. It relies on intensity measurements in two different planes, traditionally far-field and near-field. As a camera image in the focus can sometimes only consist of few illuminated pixels, preventing resolution of details, modified versions were introduced later where the measurement planes are before ($z \ll 0$) and after ($z \gg 0$) the geometrical focus [106]. The principle of the algorithm remains the same, independent of the planes chosen.

The first image measured at $z \ll 0$ is used to estimate the spatial amplitude. The spatial phase is guessed at the beginning. This beam is numerically propagated through the geometrical focus to the other plane at $z \gg 0$. The calculated amplitude is replaced by the square root of the intensity measured in the second image at this position. After propagation back to $z \ll 0$ this step is repeated until the measured and calculated intensities are identical in both planes. The calculated phase can then be decomposed into its Zernike coefficients. This method was used to achieve a wavefront correction for a heavily aberrated beam with an SLM, shown in Fig. 5.2, presented also in **Paper IV**.

4.2 Pulse duration

Measuring the pulse duration of ultrashort laser pulses shorter than $\approx 10\,\mathrm{ps}$ is challenging due to the extremely short timescales involved. Traditional electronic devices and oscilloscopes lack the temporal resolution to accurately measure such brief events. Autocorrelation was one of the first techniques introduced, where the correlation of a pulse with itself is measured by observing the strength of a nonlinearity, such as SHG, depending on the time delay between a pulse and a (self-) reference [107]. However, this technique only provides an estimation of the duration as it is unable to measure the spectral phase of the pulse, and thus is not able to tell if a pulse is perfectly compressed. To achieve a *complete* characterization, today a large variety of methods exist, with the most prominent being frequency-resolved optical gating (FROG) [108], dispersion-scan (d-scan) [109] and spectral phase interferometry for direct electric-field reconstruction (SPIDER) [110].

This section focuses on FROG and d-scan, as these methods have been employed for all the publications of this thesis.

4.2.1 FROG

In Fig. 4.2 a typical experimental setup for a scanning second harmonic FROG is shown.

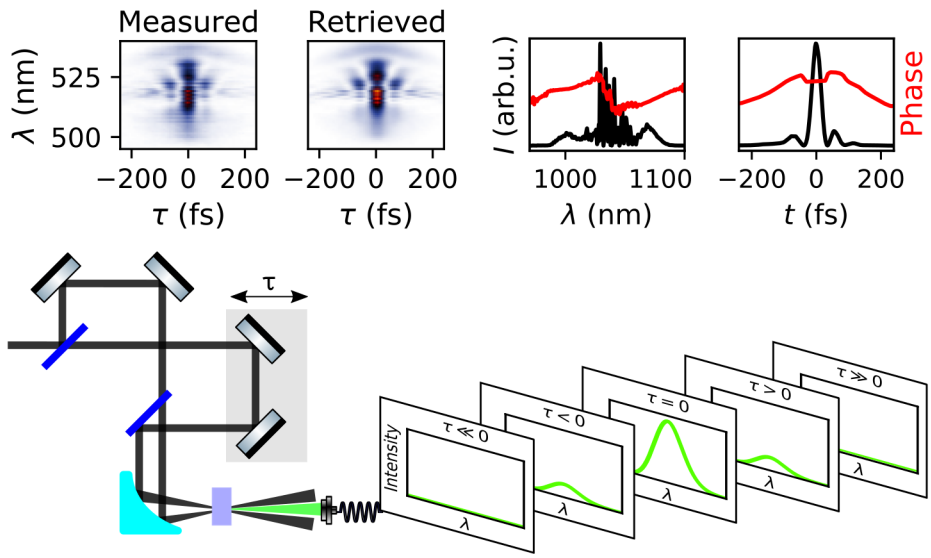

Figure 4.2: FROG setup with beam splitters (dark blue), an off-axis parabola (cyan) and an SHG crystal (purple) (bottom) and an example of a FROG trace, experimental and retrieved (top).

It consists of an interferometer, where in one arm the delay τ can be varied with fs precision. After recombination, both pulses are focused non-collinearly in a second harmonic crystal, such as BBO. If spatial and temporal overlap is achieved, not only the second harmonic of the fundamental will be generated but also the sum frequency. This will lead to a beam emitted along the central axis, which can be selected spatially. The spectrum of the sum frequency is recorded with a spectrometer while scanning the delay. The result is called a FROG trace, as shown in the top left of Fig. 4.2. The intensity is proportional to

$$I_{\mathrm{FROG}} \propto \left| \int_{-\infty}^{\infty} E(t)E(t-\tau)\exp(-i\omega t)dt \right|^2 . \tag{4.3}$$

The spectral phase, together with the fundamental spectrum, fully describes the pulse in the temporal domain. To retrieve this spectral phase the FROG trace is simulated by guessing values for the phase, and the traces are compared to the experiment iteratively until the error between the two is minimized. An example of a FROG measurement is shown in the top of Fig. 4.2. This measurement was conducted to characterize the output pulses of the MPC presented in **Paper I**.

The resolution and quality of a FROG measurement depend mainly on the resolution and scan range of the translation stage that is used to vary the delay τ. From the shape of the trace an intuitive understanding of the contributing orders to the spectral phase terms (see Eq. (2.5)) is possible. In Fig. 4.3, a simulation of FROG traces is shown for a Fourier limited pulse (left), for a GDD value of $50\,\mathrm{fs}^2$ (middle) and a TOD value of $400\,\mathrm{fs}^3$ (right). Since adding GDD stretches the pulse in time, the trace also becomes broader. TOD produces a shoulder in the pulse (see also Fig. 2.2), causing the FROG trace to fan out towards the spectral edges. It is important to notice that an SHG FROG is not sensitive to the sign of the phase terms.

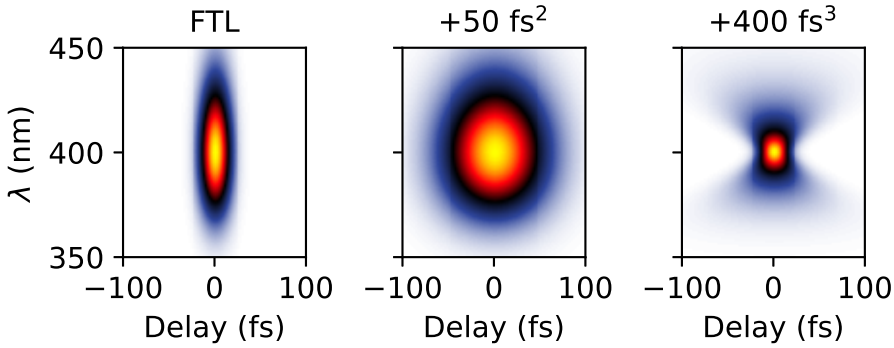

Figure 4.3: Simulated FROG traces for a Fourier-limited pulse (left), a second-order dispersed (middle) and a third-order dispersed (right) pulse.

4.2.2 d-scan

The d-scan technique consists of studying a nonlinear signal (e.g. SHG) as a function of dispersion [109, 111, 112]. Changing the dispersion can be done by e.g. inserting a material adding a term $\exp(i\phi)$ corresponding to a total material thickness Δx. A possible experimental realization for a scanning d-scan is shown in Fig. 4.4. The added positive dispersion from a wedge pair, needed for varying the dispersion, has to be pre-compensated. Here, we use a set of chirped mirrors. The spectrum of the generated second harmonic is recorded and retrieved (top of Fig. 4.4) by minimizing the error between the experiment and the calculation according to

$$I_{\text{d-scan}} \propto \left| \int_{-\infty}^{\infty} \left(\int_{-\infty}^{\infty} E(\omega) \exp(i\phi) \exp(i\omega t) d\omega \right)^2 dt \right|^2 . \tag{4.4}$$

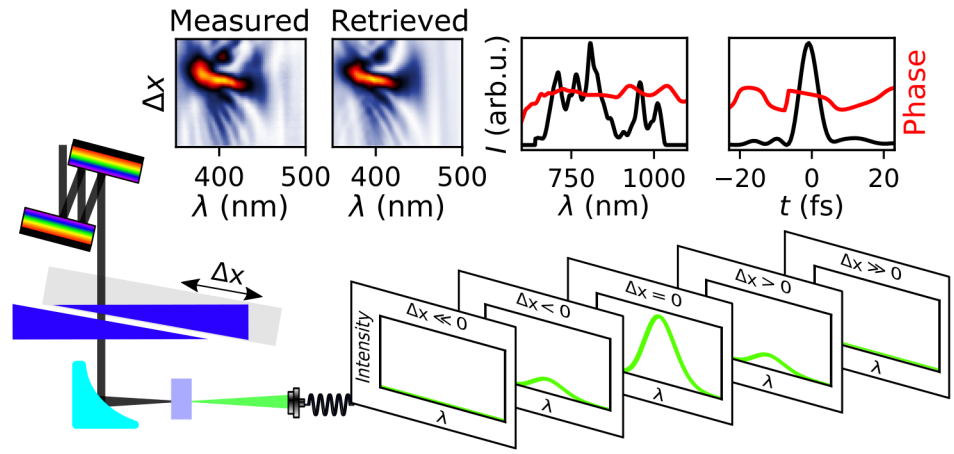

Figure 4.4: D-scan setup with chirped mirrors, a wedge pair with variable insertion (dark blue), and off-axis parabola (cyan) and a SHG crystal (purple) (bottom) and an example of a d-scan trace, experimental and retrieved including the spectral and temporal characteristics (top).

From the shape of an experimental d-scan trace many pulse parameters can be intuitively understood. Similarly to Fig. 4.3, d-scan traces are calculated using Eq. (4.4) and presented in Fig. 4.5, assuming positive dispersion from different thicknesses of BK-7 glass.

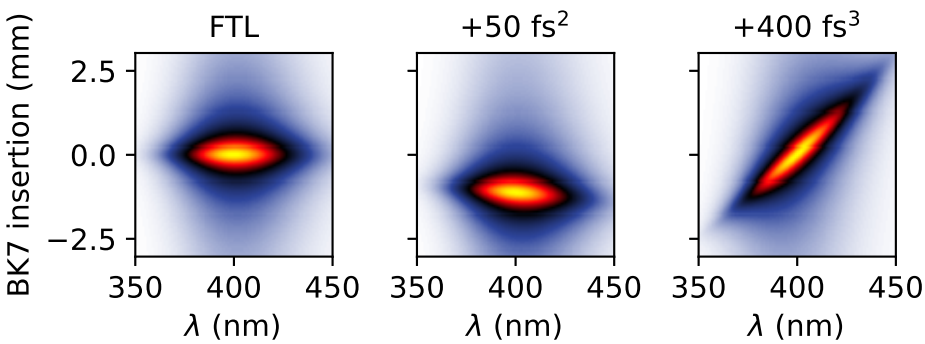

Figure 4.5: Simulated d-scan traces for a Fourier-limited pulse (left), a second-order dispersed (middle) and a third-order dispersed (right) pulse.

The zero on the vertical axis refers to the point where the amount of material perfectly compensates the pre-chirping, coinciding with the maximum signal of the trace. If a pulse is Fourier-limited before entering the chirped mirrors, the amount of dispersion needed to compress the pulse will be identical for all wavelengths, making the trace look "flat". If positive GDD is added to the pulse, as seen in the center of Fig. 4.5,

the trace will shift down, as less material is needed to compress the pulse to close to its Fourier limit. If the sign of the added GDD is negative, the trace shifts up. For TOD, the trace is tilted, as seen on the right. As TOD is proportional to the first derivative of GDD, a different amount of GDD, increasing linearly with frequency is needed to compress the pulse. The sign of the applied TOD is therefore also encoded in the direction of the tilt.

To design a d-scan setup, the proper type and amount of dispersion changing material have to be chosen. The longer the pulses are, the less sensitive they are to additional dispersion (see Fig. 2.2) which is the main reason why d-scan using material insertion and pre-chirping is so far only viable for very short, few-cycle pulses.

4.3 Time-dependent polarization

In the vast majority of applications, the polarization state of light is constant over time and can easily be characterized by measuring powers after waveplates and polarizers. In general, the interaction between light and matter depends on the polarization, e.g. ionization [113]. Polarization also has a large effect on the efficiency of HHG. The more the electric field deviates from linear polarization, the less likely the electrons are to return back to their parent atom [114–116]. This can be exploited to generate isolated single attosecond pulses if the driving pulse is linearly polarized for exactly one half-cycle [55], which is known as *polarization gating*.

In this section, a practical approach to generate a polarization gate is presented. The characterization of the gate is performed using the d-scan technique (see **Paper II**).

4.3.1 Polarization gate

There exist several methods to create a time-dependent polarization state, based e.g. on metasurfaces [117] or liquid crystals [118]. The simplest and most cost-effective approach is the use of birefringent materials which was first proposed in 1990 [119] and is now widely employed [115, 116, 120].

Such an approach, using a combination of standard waveplates, is presented in Fig. 4.6. The initial laser pulse, shown on the left, is perfectly linear, horizontally polarized, with no electric field components in the y-direction. The parameters of its polarization ellipse (see Fig. 2.6), shown at the bottom, χ (black) and 2ψ (red), are both constant and equal to zero.

This pulse is centered at a wavelength of $800\,\mathrm{nm}$ with a duration of only a few laser

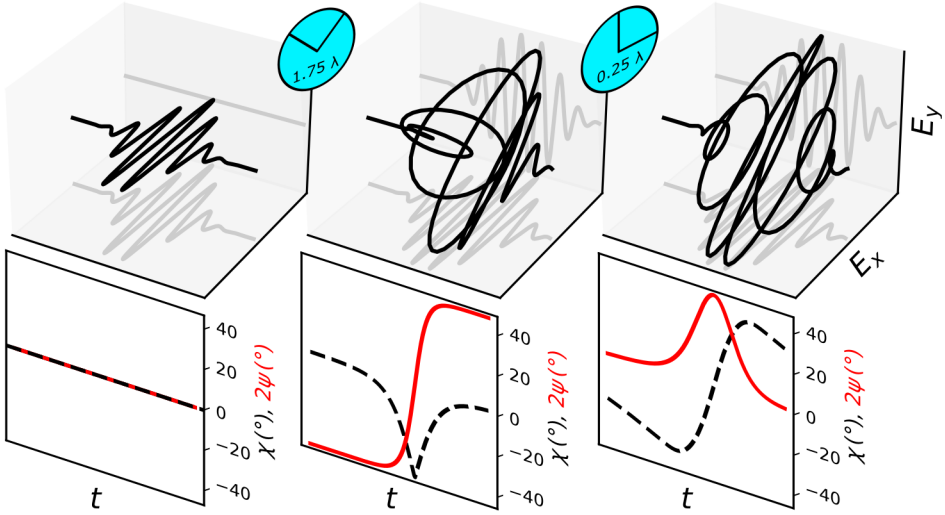

Figure 4.6: Experimental realization of a polarization gate. The electric field of an ultrashort pulse with projection in x and y in its initial, horizontally polarized state (left) after a 1.75λ (middle) and after a subsequent 0.25λ waveplate (right) (top) with the polarization ellipse parameters χ (black, dashed) and 2ψ (red) (bottom).

cycles. It then passes through a 1.75λ waveplate which is rotated by $45°$. In practice it means that this waveplate delays the orthogonal components of the pulse by $1.75\lambda/c \approx 4.7$ fs. Such a waveplate can be realized with a 157 µm thick quartz crystal with its birefringent properties highlighted in Fig. 2.5.

As one is usually interested in a strong linearly polarized component in the pulse center, a 0.25λ plate is required to transform the linear components into circular and vice versa, as shown on the right. The resulting pulse now has a strong linear component at an angle of $2\psi = 45°$ that turns into left-handed (left) and right-handed (right) circular polarization with $\chi = \pm 45°$ towards the extremities of the pulse.

The calculations leading to the illustrations of Fig. 4.6 were performed using the Jones formalism with Jones vectors resolved by frequency, further described in Section 2.3 and in **Paper II**.

4.3.2 Polarization d-scan

Several dedicated and established methods exist to characterize a time-dependent polarization state of ultrashort laser pulses, such as time-resolved ellipsometry [121], POLLIWOG [122], attosecond streaking [123] and amplitude-swing [124, 125]. Most

of these methods come with the disadvantage of having relatively complicated and alignment-sensitive experimental setups or requiring a known reference pulse.

An alternative approach is the extension of standard methods to characterize the spectral phase of linearly polarized pulses by measuring different, linear projections of the time-dependent polarization, demonstrated first with the TURTLE method [126] in 2018. In **Paper II**, this approach is used to further extend the d-scan technique (see Sec. 4.2.2).

The polarization d-scan experiment consists of a typical d-scan setup, as shown in Fig. 4.4, with two additional waveplates that produce the polarization gate, sketched in Fig. 4.6. A polarizer selects an electric field component at a defined angle after the gate has been created. A BBO generates the second harmonic signal, whose spectrum is recorded.

A d-scan measurement at two orthogonal polarizer angles (0° and 90°) is sufficient to retrieve E_x and E_y (the projections in Fig. 4.6). Such a measurement is shown in Fig. 4.7, for 5 fs long pulses at 800 nm from an Yb-pumped OPCPA described in [47, 101], after the polarization gate. The measured (left) and retrieved (middle) d-scan traces are shown for the horizontal (top) and vertical (bottom) projections. On the right is the reconstructed electric field. It has to be noted that d-scan is not sensitive to the first-order (GD) spectral phase components, meaning that the time axis is not absolute.

Thus, the only missing information is the delay between E_x and E_y, in order to fully

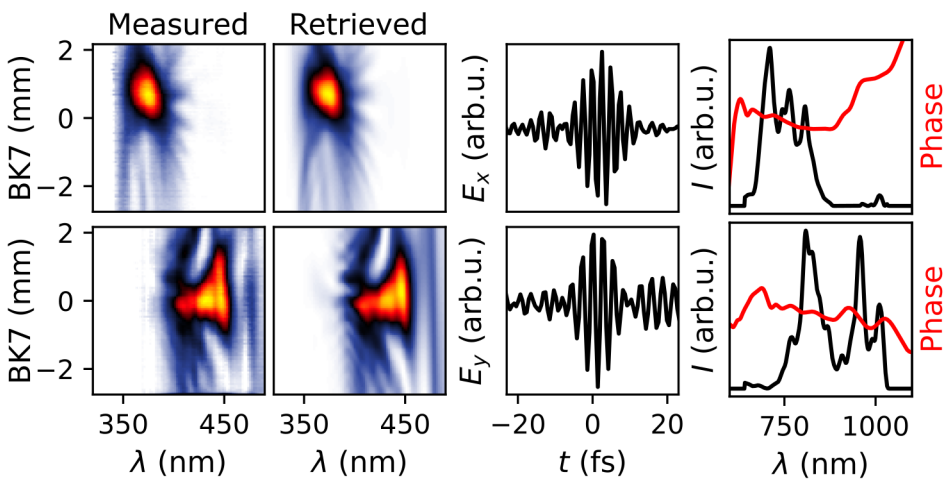

Figure 4.7: D-scans (left) and their retrieved electric field and spectrum (right) for a horizontal (top) and vertical (bottom) projection with a polarizer after a polarization gate.

describe the pulse. The complete electric field at a projection angle α is

$$\mathbf{E}_\alpha(\omega) = \cos(\alpha)E_x(\omega) + \sin(\alpha)E_y(\omega)e^{-i\omega\tau - i\varphi}\,. \tag{4.5}$$

where a first order term τ and a zero-order term φ are introduced. The spectra, $E_x(\omega)$ and $E_y(\omega)$, including their phase, are already known from the d-scan retrievals seen to the right of Fig. 4.7, meaning that the spectrum can now be calculated for any other arbitrary polarization projection angle. To find τ and φ, Eq. (4.5) is evaluated for an equally spaced grid of reasonable τ and φ values, and the calculated spectral intensity $|\mathbf{E}_\alpha(\omega)|^2$ is compared with the measured spectrum at α. τ and φ are extracted from the spectrum for which the difference between calculated and measured spectra is minimal.

In **Paper II** the complete reconstruction of a polarization gate was demonstrated using this method, from only two d-scans at orthogonal angles, presented in Fig. 4.7, and an additional spectrum at another angle.

4.4 Spatio-temporal couplings

Whenever the description of a pulse cannot be separated anymore into spatial and temporal or spectral components, see Eq. (2.26), the pulse is subjected to STCs, as discussed in Sec. 2.6. The origin of such couplings can be misaligned chromatic optical components or nonlinear interactions with matter. Especially in dispersion-manipulating elements, such as a grating compressor, which is a standard component in many ultrafast laser systems, any minor misalignment or material deformation can be detrimental [127].

In gas-filled MPCs, it has been predicted that approaching the critical power, the beam will significantly deteriorate due to STCs [96]. For bulk MPCs, where sometimes the critical power is exceeded by a factor of > 80, such as in **Paper I**, measuring the beam quality before and after the MPC is an important step to gain an understanding of how far bulk MPCs can be scaled up in terms of peak power. The same question applies to new approaches for energy scaling, such as beam folding presented in **Paper VI** where the beam undergoes a large amount of mirror reflections.

For characterizing STCs, a selection of methods exists. The most established ones are spatially-resolved Fourier transform spectrometry [128] and TERMITES [129], INSIGHT [130] which is based on phase retrieval, and SEA-SPIDER [131] based on spectral shearing. One downside of these methods is the large amount of data being generated. More recently, a novel idea was suggested and demonstrated based on a pinhole mask that requires only a few camera images, with a possibility for single-shot operation [132].

In this section, spatially-resolved Fourier transform spectrometry is introduced in more detail, as it was used to perform STC measurements for **Papers I** and **VI**. The relevance of these results will be discussed, giving an outlook on further MPC energy and peak power scalability.

4.4.1 Spatially-resolved Fourier transform spectrometry

In Fig. 4.8 we present an experimental setup. The laser beam is split to create an interferometer. In one arm, the beam is focused tightly with an off-axis parabolic mirror (cyan) and continues its path strongly diverging. In the other arm the beam remains collimated. Both beams are overlapped on a camera. One arm contains a translation stage, allowing to scan the delay τ (grey box in Fig. 4.8) when recording images.

As the distance between the camera and the geometric focus after the parabola are typically large, in the order of $0.5\,\mathrm{m}$ to $1\,\mathrm{m}$, the diverging beam has an almost homogeneous wavefront, filling the camera chip uniformly. Before entering this setup, the beam size is chosen so that the collimated beam fills the camera chip without clipping. If both beams do not overlap in time ($\tau \ll 0$ or $\tau \gg 0$), the images have a constant background (dark blue) from the diverging arm with the collimated beam in the center, shown at the bottom of Fig. 4.8. During temporal overlap, both beams interfere, giving rise to interference rings with the greatest contrast at $\tau = 0$. This behavior is summarized on the top right of Fig. 4.8 representing the relative intensity of the pixel in the center of the image as $I(x = 0, y = 0, \tau)$. The Fourier-limited spectrum $I(x, y, \omega)$ can be reconstructed for each pixel individually by Fourier transforming $I(x, y, \tau)$. To resolve the whole spectrum of a pulse, the scan range has to be large

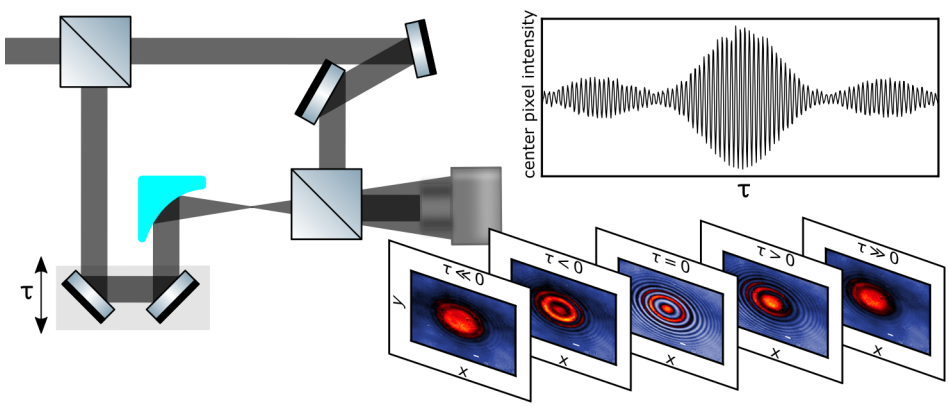

Figure 4.8: Experimental setup for spatially-resolved Fourier transform spectrometry, inspired by [128].

for narrow spectra and can be smaller for broader spectra.

As the distance between focus and camera is known in the diverging arm, the curvature of the wavefront can be subtracted in the spectral domain, and $I(x, y, \omega)$ can be propagated to the desired plane of observation (see Fig. 2.10).

4.4.2 Evaluation of spatio-temporal couplings in MPCs

At the time of evaluating the results of the MPC in **Paper I** (Fig. 3.14), this work constituted the highest input peak power in a bulk MPC with 370 MW, which is > 80 times the critical power for fused silica (4.3 MW [82]). Since for peak powers $P > 50P_{\text{crit}}$ small scale self-focusing and filamentation can occur [34], the risk of beam quality degradation was deemed significant. Therefore, an STC measurement using spatially-resolved Fourier transform spectrometry with the setup presented in Fig. 4.8 was performed on the input as well as the output of the MPC.

The results are summarized in Fig. 4.9, with the input of the cell on the left and the output on the right showing the far-field plane (focus). The top and the middle graphs represent a cut through one spatial dimension ($y = 0$ or $x = 0$). In the spectral domain at the top, the reconstructed spectra match the experimental ones shown in Fig. 3.14 reasonably well. In the horizontal (x) direction, no significant couplings are visible, evident by a homogeneous spectrum independent of the x value. Along the y-direction, however, a tilt becomes visible (dashed line). Interestingly, a similar tilt is also visible in the MPC output to the right, but only for the central, unbroadened frequency part, whereas the new frequencies do not exhibit this spatial chirp.

Later, it was found that a misaligned grating compressor after the Yb rod amplifier that served as the input for the MPC was responsible for the observed tilt. However, it indicated that the frequencies created via self-phase modulation do not seem to inherit STCs from the input beam.

The bottom of Fig. 4.9 shows the sum over all frequencies (or times) for y vs. x, thus the beam profile one would observe on a camera. For the input and the output, the reconstructed focal spot looks perfectly round. For a fair judgement, these foci are compared with the reconstructed foci where all wavefront errors are removed artificially, thus the cleanest beam that is theoretically achievable. Both images, with the measured wavefront and the ideal wavefront, are normalized to the maximum of the ideal one. Comparing the peaks of measured and ideal focus yields the 2D-Strehl ratio, defined by

$$S_{\text{2D}} = \frac{\max(I_{\text{meas}}(x, y))}{\max(I_{\text{ideal}}(x, y))} \,. \tag{4.6}$$

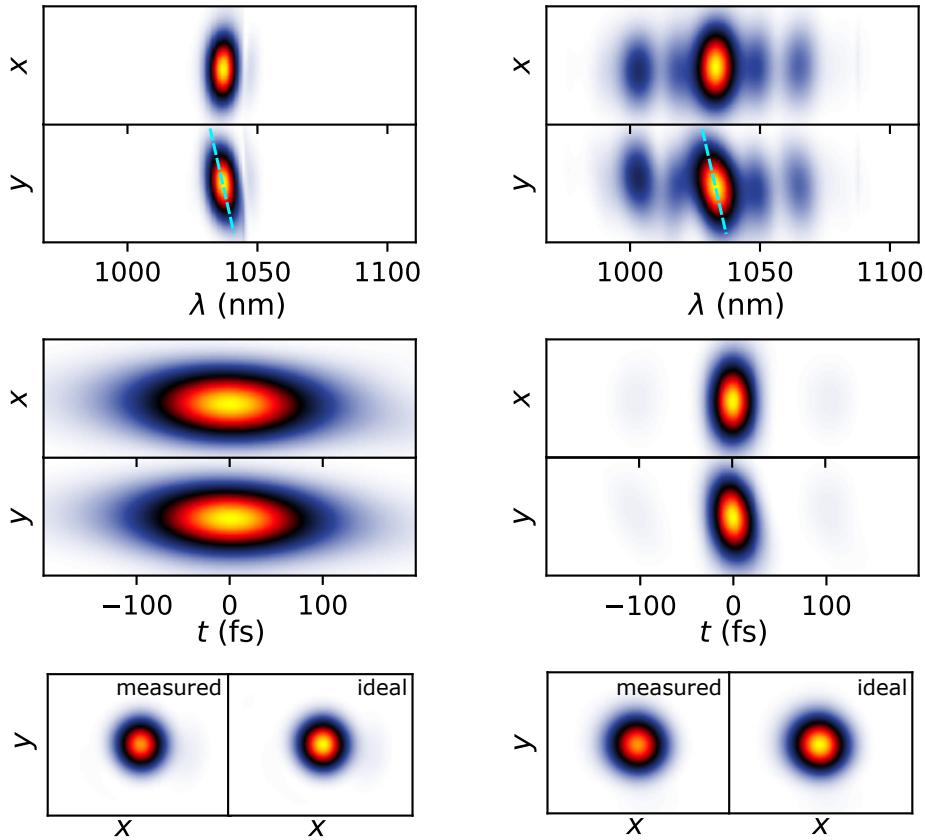

Figure 4.9: Results from a spatio-temporal measurement for the input (left) and output (right) of the MPC presented in Fig. 3.14, for $x/y - \lambda$ with $y = 0/x = 0$ (top), $x/y - t$ with $y = 0/x = 0$ (middle) and $x - y$ (bottom) representation.

For both the input and the output of the MPC, a Strehl ratio of ≈ 0.9 was found, showing no significant change in STCs with a total of 60 passes through fused silica plates with powers exceeding the critical power over 80 times.

For **Paper VI**, where a folded design is adopted for a gas MPC, the concerns about STCs were of different nature. As the number of mirror reflections scales linearly with the folding factor introduced by the plane mirror pair (see Fig. 3.15 (right)), the question of whether such a large number of reflections (> 500) negatively affects the beam quality was raised. The same type of measurements as shown in Fig. 4.9 were performed, with the conclusion that the number of mirror reflections itself does not seem to impact the results. However, a degradation of the beam quality was observed relatively quickly when exceeding $P/P_{\text{crit}} > 0.5$ for the MPC filled with 1 bar of krypton.

An example for $P/P_{\text{crit}} = 0.65$ is given in Fig. 4.10. Quantifying STCs by defining a specific slope or other feature, as it is done in Fig. 4.9 (dashed lines), is hardly possible here.

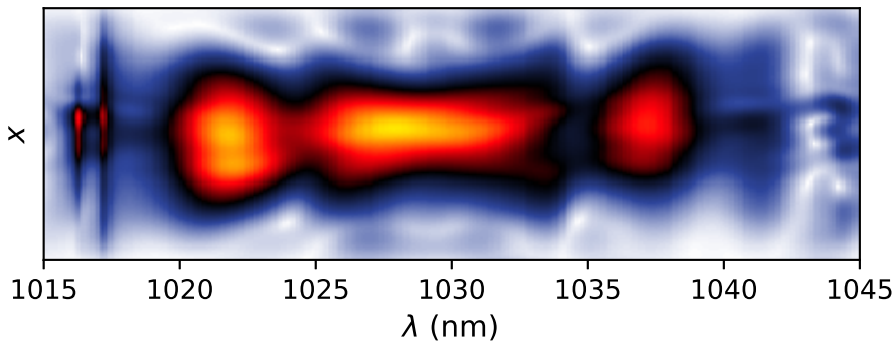

Figure 4.10: $x - \lambda$ representation of the folded gas MPC filled with $1\,\text{bar}$ of krypton for $P/P_{\text{crit}} = 0.65$.

In one of the first experimental works on MPCs for post-compression in 2017, the measure of spectral homogeneity parameter V was introduced [84], calculated by

$$V(x,y) = \frac{\int \sqrt{I(x,y,\lambda) \cdot I(x_0,y_0,\lambda)}d\lambda}{\int I(x,y,\lambda)d\lambda \cdot \int I(x_0,y_0,\lambda)d\lambda} \tag{4.7}$$

where x_0 and y_0 hereby refer to the coordinates of the center of the beam profile. The spatially-dependent V parameter is plotted in Fig. 4.11 for $P/P_{\text{crit}} = 0.4$, 0.5, $0,6$ and 0.65 from left to right for the krypton-filled MPC. The x and y axes are normalized to the respective beam size, with the cyan circle indicating w_0.

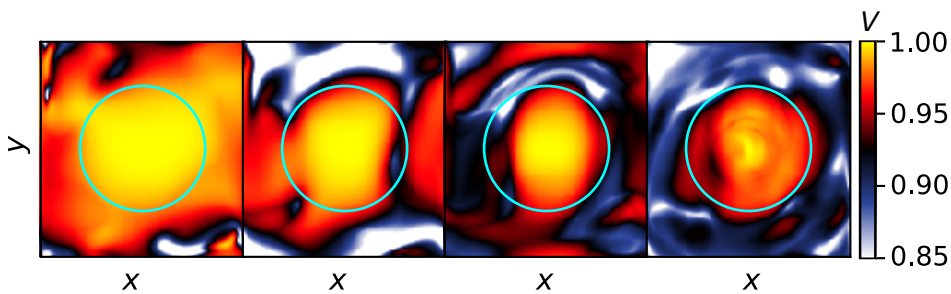

Figure 4.11: Spectral homogeneity V for $P/P_{\text{crit}} = 0.4$, 0.5, $0,6$ and 0.65 from left to right. The cyan circle represents w_0. Figure adapted from **Paper VI**.

The decline in the mean value of V within the cyan circle is evident when approaching

the critical power. The degradation towards P_{crit} in gas MPCs is expected, as predicted in [96].

4.5 Carrier-envelope phase

When pulses approach the few- to single-cycle regime, the offset between the maximum of the electric field and its field envelope has a significant influence on the field shape within the pulse, which can have a large effect on strong-field phenomena, such as HHG [133].

The dependence of strong field processes on the laser electric field can also be used to detect the CEP, by e.g. observing asymmetric count rates of electrons in opposite directions while performing above-threshold-ionization (ATI) experiments, known as stereo-ATI [134]. Other methods depending on strong-field interactions, such as attosecond streaking [135], tunnel ionization in air [136] or electro-optical sampling relying on the Pockels effect [137] allow complete electric field reconstructions including CEP information. Most of these techniques rely on interferometric measurements and thus are not suitable for single-shot detection. Although, e.g. stereo-ATI is capable of providing high-repetition-rate CEP detection [138], it requires laser pulse energies of several µJ as well as expensive vacuum equipment.

In this thesis work (**Paper III**) a characterization method allowing single-shot CEP detection at high repetition rates (hundreds of kHz) is presented. It is based on f-$2f$ interferometry which was developed in the late 90s, encoding the CEP in the spectral domain [139, 140].

4.5.1 f-$2f$ interferometry

The principle is illustrated in Fig. 4.12. A laser pulse is first broadened to an octave-spanning spectrum via white-light generation and then sent subsequently into a crystal to generate the second harmonic. If the input spectrum is broad enough, as seen in the bottom, the fundamental and its second harmonic will spectrally overlap, creating interference fringes. The fringe frequency depends on the time delay between the fundamental and second harmonic, but the fringe phase offset is CEP dependent. When zooming into the spectral overlap region, the difference between $\varphi = 0$ (black) and $\varphi = \pi$ (red) is shown. This relative phase-offset between two pulses can be easily extracted by performing a Fourier transform of the fringes, as seen in the top right in Fig. 4.12.

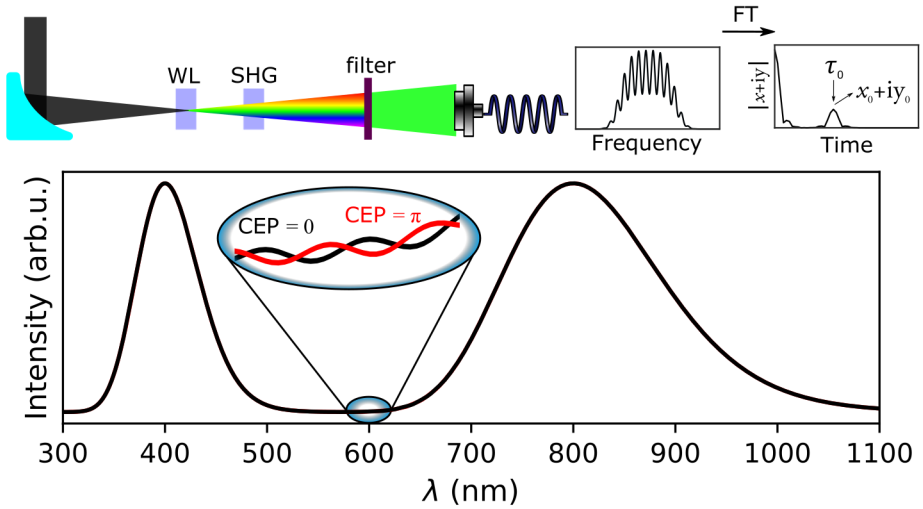

Figure 4.12: f-$2f$ measurement scheme. The laser pulses (f) are first broadened to an octave-spanning spectrum via white-light (WL) generation before generating the second harmonic ($2f$) in a crystal via SHG. The spectral overlap between fundamental f and $2f$ is filtered (green) and sent to a spectrometer (top). The CEP is encoded in the phase of the spectral overlap fringes (bottom).

4.5.2 Digital single-shot CEP detection

The practical challenge lies in recording and evaluating those fringes experimentally, at high repetition rates of several tens to hundreds of kHz. Recording CEP fringes at 200 kHz with a fast line-camera was demonstrated in single-shot operation [101], however, the amount of data that is generated quickly exceeds the frame of practically handlable datasets after not even a few seconds. The recorded data also has to be post-processed to extract the relative CEP in an additional step.

The challenge of fast data acquisition can, for example, be tackled by converting the spectral fringes to temporal fringes and then relying on fast analog electronics [141]. However, this does not solve the issue of having to perform the Fourier transformations in a separate step.

If the objective of the CEP measurement is to prove that a certain laser system preserves the CEP stability of the actively stabilized oscillator front-end, recording a small dataset with a separate evaluation later is usually sufficient. For example, 200 000 spectra after an f-$2f$ setup were recorded in single-shot with a fast line camera during 1 s for the output of the MPC discussed in **Paper I**. As only the oscillator in the laser chain is actively CEP stabilized, it was interesting to demonstrate that this stability is preserved. On the left in Fig. 4.13, the oscillator is free-running, on the right it is actively stabilized. While the CEP fringes on the left are washed out when displaying

200 000 individual spectra on top of each other, the fringes on the right remain with an almost constant frequency offset, clearly demonstrating maintained CEP stability.

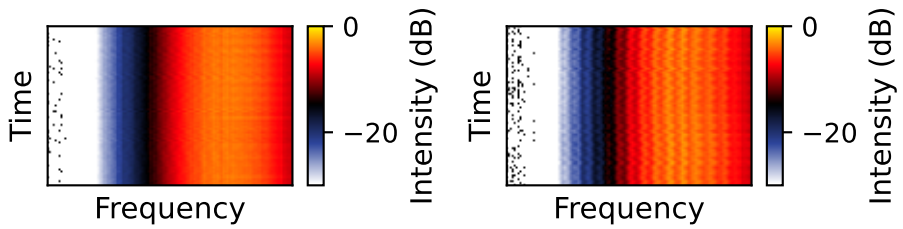

Figure 4.13: Fringes from an f-$2f$ scheme for the output of the MPC discussed in Fig. 3.14 for a free-running (left) and an actively CEP stabilized (right) oscillator, for $200\,000$ spectra measured in single-shot during $1\,\mathrm{s}$ with a fast line camera, adapted from **Paper I**.

Even if the CEP stability is evident to the right of Fig. 4.13, looking more closely, small variations are visible. For experiments that are highly CEP sensitive, such as HHG with few-cycle pulses and subsequent applications in pump-probe photoelectron spectroscopy [101], logging these variations can lead to significantly higher data quality in post-processing and give further insight into measurement errors in the actual experiment. This necessity led to the efforts presented in **Paper III**, providing a direct, relative CEP measurement with the required Fourier transform of the f-$2f$ fringes performed optically.

4.5.3 Analogue CEP detection

Optical Fourier transform

A numerical Fourier transform of a spectrum $I(\omega)$ yields a complex quantity

$$I(\tau) = x + iy = \int_{-\infty}^{+\infty} I(\omega) e^{-i\omega\tau} d\omega \tag{4.8}$$

which is mathematically equivalent to

$$x + iy = \int_{-\infty}^{+\infty} I(\omega) \left(\cos(\omega\tau) - i\sin(\omega\tau)\right) d\omega\,. \tag{4.9}$$

In Fig. 4.14, Eq. (4.9) is illustrated graphically. If, for a specific τ_0, x_0 and y_0 are extracted and plotted against each other, the angle between the x-axis and the (x_0, y_0) vector describes the relative phase φ, which is equal to the CEP if $I(\omega)$ describes fringes from an f-$2f$ setup.

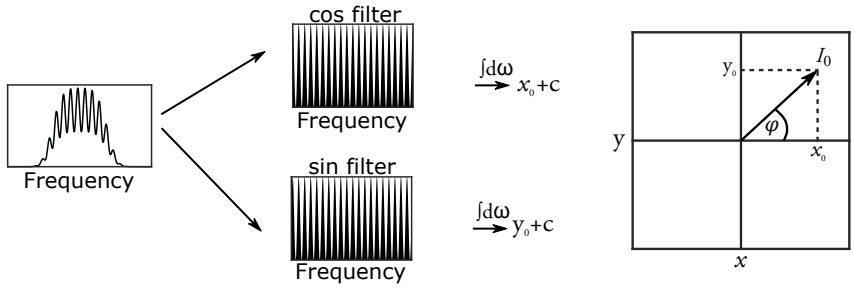

Figure 4.14: Principle of an optical Fourier transformation. By applying a cosine and sine frequency filter (middle) to the spectral fringes from an f-$2f$ setup (left), the CEP φ can be reconstructed (right). Illustration adapted from **Paper III**.

In **Paper III** a purely optical Fourier transform was demonstrated to extract φ with fast photodiodes and analogue differential amplifiers, providing CEP tagging at 200 kHz by realizing optical sine and cosine filters with an interferometer.

Experimental setup

The experimental setup is shown in Fig. 4.15.

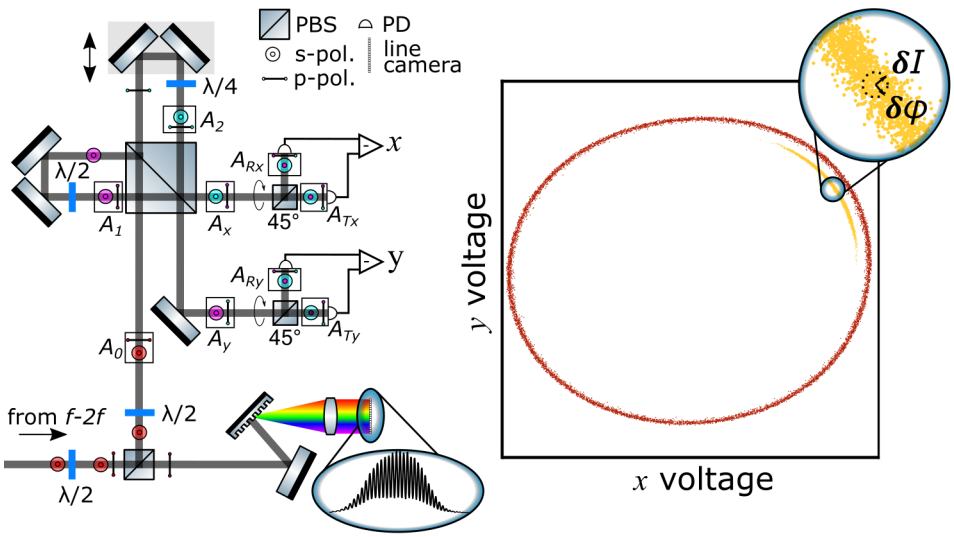

Figure 4.15: Experimental setup for an optical Fourier transform (left) and its measurement results for free-running CEP (red) and actively stabilized CEP (yellow) (right), adapted from **Paper III**.

An f-$2f$ signal is created from the output of an OPCPA centered at 800 nm with a pulse duration of 6 fs [47] with vertical (s) polarization (circle), shown at the bottom

of the figure. A $\lambda/2$ plate turns the polarization to $45°$ to split the signal equally with a polarizing beam splitter (PBS). The transmitted part, linearly polarized (p) is dispersed by a grating, separating the frequencies spatially, and sent on a fast line camera, which is able to record the spectral fringes in single-shot at very high speeds. This part of the setup represents a traditional CEP measurement, comparable to Fig. 4.13, and was used to benchmark the newly presented method.

The vertically polarized part is turned to $45°$ polarization (A_0) and enters an interferometer. At the large PBS, the s-polarized part will be reflected into arm 1, the p-polarized part will be transmitted into arm 2. In arm 1, the linearly, vertically polarized light will be turned by a $\lambda/2$ waveplate to $45°$, the total electric field vector $\mathbf{A_1}(\omega)$ at the end of this interferometer arms then reads

$$\mathbf{A_1}(\omega) = \frac{1}{2}A_0(\omega)e^{i\omega\tau_1}\hat{s} + \frac{1}{2}A_0(\omega)e^{i\omega\tau_1}\hat{p} \tag{4.10}$$

with τ_1 being the time delay accumulated in the interferometer arm. In arm 2, a $\lambda/4$ introduces a $\pi/2$ phase shift to the linearly, horizontally polarized light turning the polarization state to circular. An additional phase shift $\Delta\phi$ due to setup imperfections and the arm length correspond to a delay τ_2. The total electric field vector $\mathbf{A_2}(\omega)$ is

$$\mathbf{A_2}(\omega) = \frac{1}{2}A_0(\omega)e^{i\omega\tau_2}\hat{s} + \frac{1}{2}A_0(\omega)e^{i\omega\tau_2 - i\pi/2 + i\Delta\phi}\hat{p}\,. \tag{4.11}$$

The PBS splits $\mathbf{A_1}(\omega)$ and $\mathbf{A_2}(\omega)$ again, mixing the s and p components of arm 1 and 2, resulting in

$$\mathbf{A_x}(\omega) = \frac{1}{2}A_0(\omega)e^{i\omega\tau_2}\hat{s} + \frac{1}{2}A_0(\omega)e^{i\omega\tau_1}\hat{p} \tag{4.12}$$

and

$$\mathbf{A_y}(\omega) = \frac{1}{2}A_0(\omega)e^{i\omega\tau_1}\hat{s} + \frac{1}{2}A_0(\omega)e^{i\omega\tau_2 - i\pi/2 + i\Delta\phi}\hat{p}\,. \tag{4.13}$$

The subsequent elements in the x part and in the y part of the setup are identical. Another PBS rotated by $45°$ mixes the s and p components in the reflected (R) and transmitted (T) components. The intensities are measured by the photodiodes (PDs). Assuming $\tau_1 = \tau_2 = \tau$ with $\Delta\phi$ accounting for the remaining relative delay, the transmitted intensity for x becomes

$$I_{Tx} = |\mathbf{A_{Tx}}|^2 = \frac{A_0^2}{4}(1 + \cos(\omega\tau))\,. \tag{4.14}$$

The reflective intensity is

$$I_{Rx} = |\mathbf{A_{Rx}}|^2 = \frac{A_0^2}{4}(1 - \cos(\omega\tau)) \tag{4.15}$$

accounting for the π phase-shift between transmission and reflection. A_x is multiplied by $\left(\frac{1}{\sqrt{2}}\hat{s} + \frac{1}{\sqrt{2}}\hat{p}\right)$ (transmission) and $\left(\frac{1}{\sqrt{2}}\hat{s} - \frac{1}{\sqrt{2}}\hat{p}\right)$ (reflection) respectively to simplify Eq. (4.14) and Eq. (4.15).

The difference between the two PD signals thus is proportional to

$$I_{Tx} - I_{Rx} \propto \cos(\omega\tau)\,. \tag{4.16}$$

Applying the same math to the y part and accounting for the additional $\pi/2$ phase term in $\mathbf{A_y}(\omega)$ results in a sine instead of a cosine term,

$$I_{Ty} - I_{Ry} \propto \sin(\omega\tau + \Delta\phi)\,. \tag{4.17}$$

The voltages x and y that are actually measured by the PDs are integrated over ω, assuming a CEP of φ, resulting in

$$x \propto a\cos\varphi \tag{4.18}$$
$$y \propto b\sin(\varphi - \Delta\phi) \tag{4.19}$$

with a, b being the response of the PDs.

Results

In an ideal experiment, with $\Delta\phi = 0$ and $a = b$, x and y are tracing a perfect circle when plotting them for varying values of φ. For a real experimental setup y over x traces an ellipse, as seen to the right of Fig. 4.15 in red containing 100 000 individual dots, measured in single-shot over the span of 0.5 s. When actively stabilizing the CEP, the dots are confined to a small section of the graph (yellow), where their spread in angle is the standard deviation $\delta\varphi$ of the CEP.

This method, demonstrated at 200 kHz potentially opens up new possibilities for measuring the CEP of individual laser pulses at the full repetition rate of ultrafast oscillators in the several tens of MHz regime.

Chapter 5

Yield optimization of high-order harmonic generation with a two-color laser driver

This chapter contains our results on HHG driven by an Yb-based laser and its second harmonic. First, a historical background on the origin and applications of two-color HHG is given, with an emphasis on yield optimization efforts. Then the experimental results (see also **Paper V**), using the setup described in **Paper IV**, are presented, before introducing the theoretical model used to predict the optimum two-color field parameters to achieve an enhancement of the XUV flux for a specific high harmonic order.

5.1 Applications of two-color HHG and project motivation

The first two-color HHG experiment was conducted in 1994 where Watanabe et al. observed a strong enhancement of the HHG flux by adding 3ω to their ω field at a central wavelength of $745\,\mathrm{nm}$ [12]. A more detailed study on the effect of relative phase and relative field ratio was published later using a ω-2ω field, highlighting that in addition to obtaining also even harmonic orders and a general increase in HHG flux, the flux of different harmonic orders peaked at different relative phases at a fixed field ratio [142]. This was also theoretically investigated and confirmed, linking the shape of the return energy vs. return time curves (see bottom of Fig. 2.17) to the harmonic yield, further confirming the validity of the semi-classical three-step model [143].

HHG with more than one color has been used in various applications, from employing the second harmonic as a perturbative probe for studying the HHG process itself [14–16, 144, 145] to HHG flux optimization [146–150], orbital-angular momentum studies [151, 152] and spectral [153–156] and temporal [157] shaping. Theoretical studies have provided also waveform parameters for multi-color synthesis to enhance flux and/or cutoff [13, 158, 159].

The study presented in **Paper V** is focused on the optimization aspect of the HHG flux.

5.2 Experimental method

In the experiment, the two-color phase ϕ and the ratio R of the second harmonic compared to its fundamental are varied, at constant total intensity, to optimize the yield for each high harmonic order in the XUV spectrum.

5.2.1 Experimental setup

The experimental setup shown in Fig. 5.1, and described and discussed in detail in **Paper IV**. It is capable of controlling all parameters of the two-color field described by Eq. (2.44) as well as the spatial alignment of the individual colors.

Beampath

The heart of the setup is a commercial Yb-laser source (Pharos, Light Conversion) with 180 fs long pulses at a pulse energy of 700 µJ and a repetition rate of 10 kHz. A beamsplitter with 80 % reflectance and 20 % transmittance divides the power. Most of it is reflected into the 1030 nm arm of the interferometer (black). The remaining transmitted power is converted with 40 % efficiency to 515 nm (green) in a 1 mm thick BBO crystal, and the unconverted infrared is dumped with a dichroic mirror and beam block.

Both interferometer arms start with an attenuator, consisting of a half-wave plate on a motorized mount in combination with a polarizer. These were used to achieve precise and reproducible control of the total combined intensity I_{tot}, as well as the fraction of second harmonic intensity R (see Eq. (2.44)).

The beam is telescoped with two lenses to a $1/e^2$ diameter of 8 mm to optimally fill the size of the respective active area of a spatial-light modulator (SLM), which will be

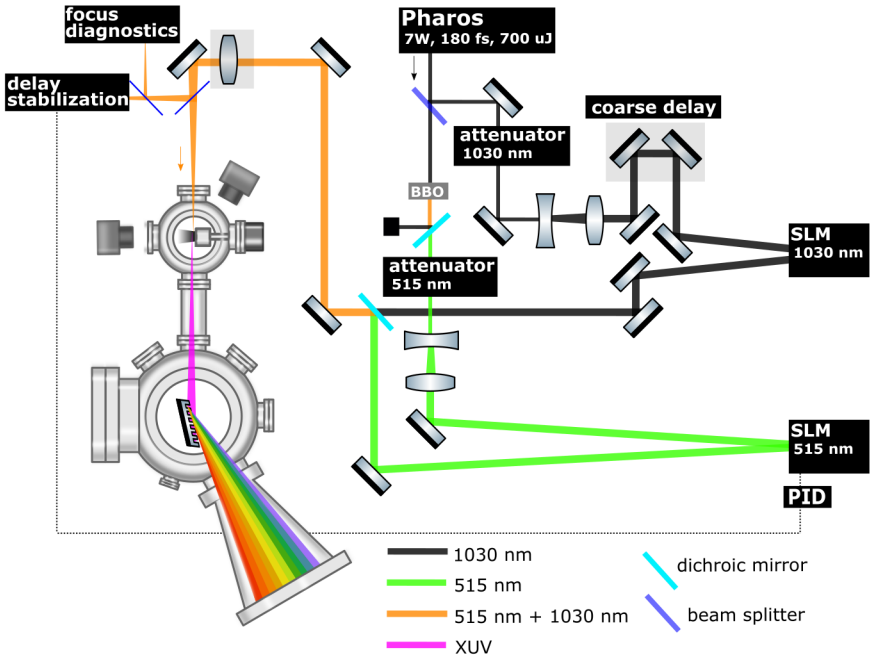

Figure 5.1: Experimental setup for two-color HHG. Figure adapted from **Paper** IV.

discussed in more detail later in this section. The beams are recombined with another dichroic mirror and propagate collinearly (orange). A lens with $f = 250\,\mathrm{mm}$ focuses both colors into the HHG gas target. After this lens, a thin glass plate reflects $\approx 1\,\%$ of the fundamental and the second harmonic out, into the diagnostic part of the setup.

A fraction of this $1\,\%$ is reflected onto a camera that is placed on a motorized translation stage to estimate the relative positions and sizes of the focii in the gas target area for both colors.

The rest of the $1\,\%$ leak is sent into the delay stabilization part. A waveplate rotates the polarization of the $1030\,\mathrm{nm}$ from horizontal to vertical. $9\,\mathrm{mm}$ of additional BK-7 glass delay the two colors artificially. In another BBO crystal, second harmonic is generated at perpendicular polarization compared to its fundamental input, resulting in identical polarization for the newly generated second harmonic and the second harmonic from the interferometer. These two contributions interfere spectrally. From the resulting interference fringes, the relative phase ϕ can be extracted via Fourier transformation.

The working principle of an SLM is illustrated in the top of Fig. 5.2.

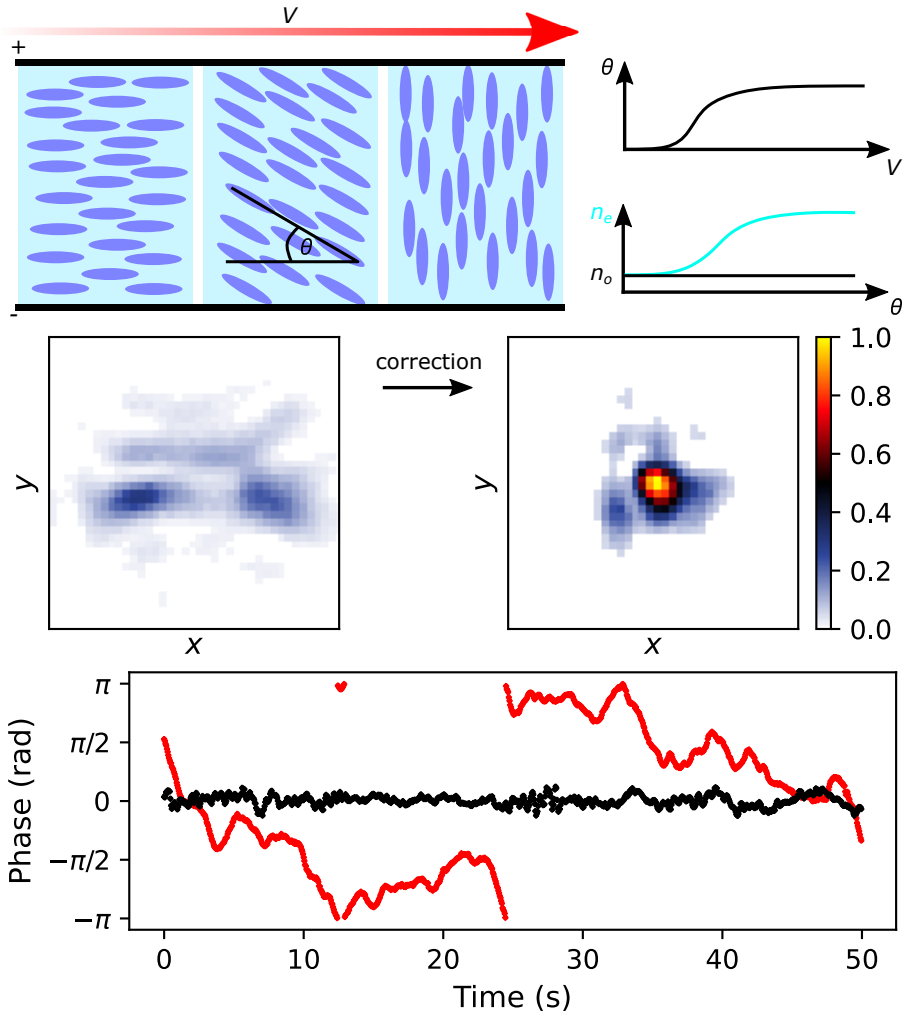

Figure 5.2: Working principle of a spatial light modulator (top), with an illustration of the liquid crystal array (left) and the schematic evolution of crystal angle and resulting refractive indices (right). Example of a beam-profile correction (middle), from an abberated profile in the focus (left) to a significant improvement (right) after correction. Both images are normalized to the same area. Measured relative two-color phases (bottom) for free-running (red) and actively stabilized (black).

It usually consists of an array of elongated molecules between electrodes that form a crystalline structure. The orientation angle θ of these molecules is sensitive to the applied voltage V. Due to the change in crystal structure, the extraordinary refractive index n_e is also affected, schematically sketched in the top right in Fig. 5.2. A change

in refractive index is equivalent to a time delay and thus a phase shift, and as V can be set individually for each pixel in this array, the wavefront across a whole laser beam can be shaped.

A common use of SLMs is to correct for spatial aberrations; see Sect. 2.5. A practical example is presented in the middle of Fig. 5.2. On the left, the intensity of a beam profile is shown after focusing it with a lens onto a camera. By applying a combination of Zernicke polynomials (see Fig. 2.8) to the SLM, which is located before the focusing lens, the spatial phase of the beam can be corrected. Thus, the beam profile improves significantly in the focus, enabling higher peak intensities, as seen on the right.

In addition to arbitrary wavefront correction, the application of Z^1_{-1} (vertical tilt) and Z^1_1 (horizontal tilt) can serve as a fine alignment tool perpendicular to the propagation direction, while Z^2_0 (defocus) can shift the focused beam along z.

Z^0_0 is a constant phase shift over the whole beam area, which is equal to a time delay. An SLM can therefore be used to temporally control the arrival time of a laser pulse on the sub-cycle level. In the bottom of Fig. 5.2 the measured phase between two colors (ϕ in Eq. (2.44)) is shown without (red) and with (black) active phase stabilization, with a standard deviation of $< 150\,\mathrm{mrad}$. Each data point in the graph consists of 20 individual laser pulses. The SLM used has a response time of $200\,\mathrm{ms}$, and a range of $\Delta\phi = 2\pi$.

5.2.2 Experimental procedure

The fundamental at $1030\,\mathrm{nm}$ is first sent into the argon gas jet for alignment. In Fig. 5.3 a simplified version of the HHG part of Fig. 5.2 is shown. At a gas pressure of around $1\,\mathrm{mbar}$ in the generation chamber, the geometric focus of the beam becomes visible due to the generated plasma. Camera A can then be used to align the laser with the gas nozzle vertically and to determine the focus position along the propagation direction. The chamber is then pumped down to $\approx 1 \times 10^{-6}\,\mathrm{mbar}$. In HHG conditions, with a high pressure at the exit of the nozzle, a plasma plume is observed at the intersection of the laser and the gas. Camera B is then used to control the distance between the plasma plume and the gas nozzle exit. Camera C is used as a beam profiler, mounted on a motorized translation stage. If the geometrical focus is moved along the propagation direction, with either the lens in front of the chamber or one of the SLMs, the beam profiler can be moved as well. The beam profile measured at the HHG position allows for the estimation of the laser intensity. Finally, C is also utilized to visualize the alignment for optimum overlap of the two colors.

The generated XUV spectrum is spatially dispersed by a curved grating (Hitachi,

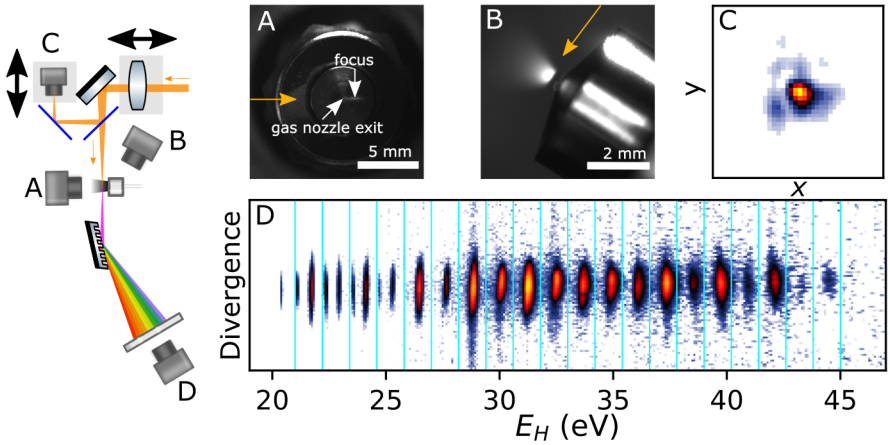

Figure 5.3: Simplified schematics of the HHG part of the waveform synthesizer (left) with the view of four cameras (right) for alignment and focus positioning into the chamber (A,B), focus diagnostic on a motorized translation stage (C) and the image of the MCP displaying the HHG spectrum after energy axis calibration (D). The orange arrows in A and B represent the laser direction.

600/mm, 22 nm to 124 nm) onto an MCP with a phosphor screen behind, which is imaged with camera D. To have a fair comparison of the XUV yield between only the fundamental and the synthesized two-color waveform, the signal on D is optimized while the 515 nm arm is blocked by fine alignment of the focus position with the 1030 nm SLM. To then optimize the XUV signal with the spatial overlap of both colors, the phase is actively stabilized to a certain value to disentangle the effect of the relative phase and spatial overlap.

5.2.3 Data collection and treatment

For each combination (R, ϕ) an image is taken by camera D. This happens fully automated and thus reduces human error significantly. Figure 5.3 shows an example of an XUV spectrum on a logarithmic intensity scale for better visibility, with the x axis energy-calibrated. The odd and even harmonics, due to the two-color field, are spaced by the expected 1.2 eV. To judge the XUV yield per harmonic, the intensity within the cyan lines is summed up. For low-order harmonics, the second diffraction order of the grating is visible, thus the integration window has to be smaller in this region. For each XUV spectrum the laser parameters (R, ϕ, I_{tot}, foci position) are recorded simultaneously by a home-built control software.

I_{tot} is defined by the sum of the peak intensities of the fundamental and second harmonic. In the experiment, R was set to represent the second harmonic intensity ratio in the center of the beam profiles. Since the focus sizes of the two colors differ by a

factor of 2 ($w_\omega = 27\,\mu\text{m}$, $w_{2\omega} = 14\,\mu\text{m}$), R in the following graphs, further analysis refers to the weighted average R between the two beam profiles.

5.3 Experimental results

In Fig. 5.4, the XUV yield measured at a constant $I_{\text{tot}} = 0.9 \times 10^{14}\,\text{W/cm}^2$ for the individual harmonic orders is shown as a function of R and ϕ. The graphs are normalized for each harmonic.

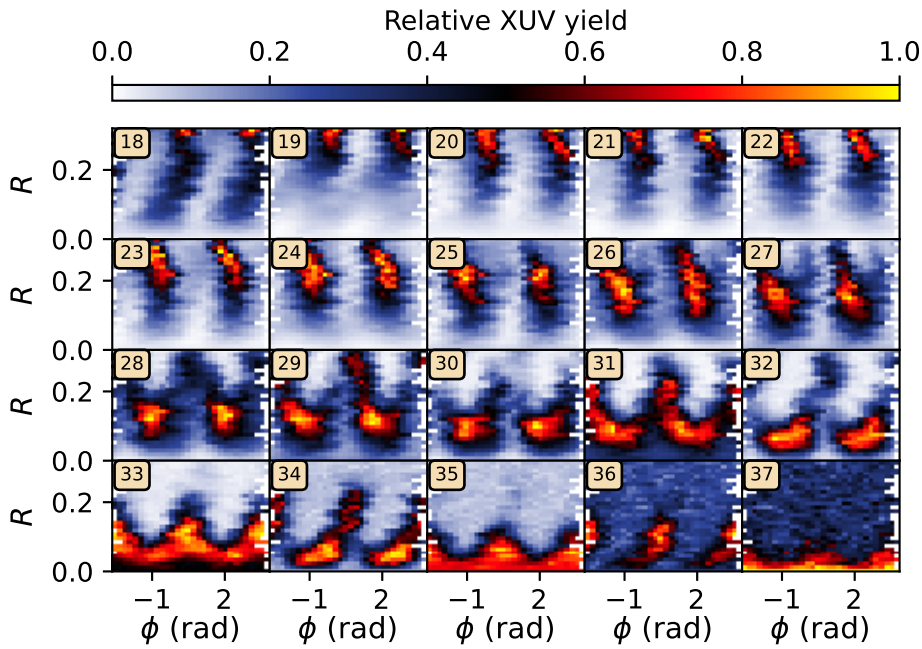

Figure 5.4: XUV yield for individual harmonic orders for R vs. ϕ in a 2π range, for $I_{\text{tot}} = 0.9 \times 10^{14}\,\text{W/cm}^2$. The harmonic order is indicated in each subfigure.

For each harmonic order and R, the yield oscillates with ϕ with a π periodicity. For low harmonic orders up to H22, a global XUV yield maximum (R_{opt}), is beyond the experimentally accessible range. From H23 until the cutoff at H37 R_{opt} can be determined. The structure of the XUV yield in Fig. 5.4 is more and more complex towards the cutoff, where it becomes difficult to determine an optimum phase ϕ_{opt}.

For each harmonic and R, a cosine function $Y_R(\phi)$ is fitted to the measured XUV

yield as

$$Y_R(\phi) = A\cos(2(\phi - \phi_{\text{opt}})) + C \tag{5.1}$$

with A being the two-color XUV oscillation amplitude and C the signal baseline. The results of the fit are presented in Fig. 5.5 on the top.

On the left, $Y_R(\phi_{\text{opt}})$ as a function of harmonic order H and R is plotted which translates to $A + C$. The cyan dashed line indicates R_{opt}, the ratio value for which a harmonic order has the highest flux. By comparing these XUV yield values at R_{opt} to the value for $R = 0$, the maximum flux enhancement is shown in the bottom left of the figure for odd harmonic orders. The red area indicates where R_{opt} is outside the experimental range.

On the right of Fig. 5.5, the phase value ϕ_{opt} corresponding to the maximum yield

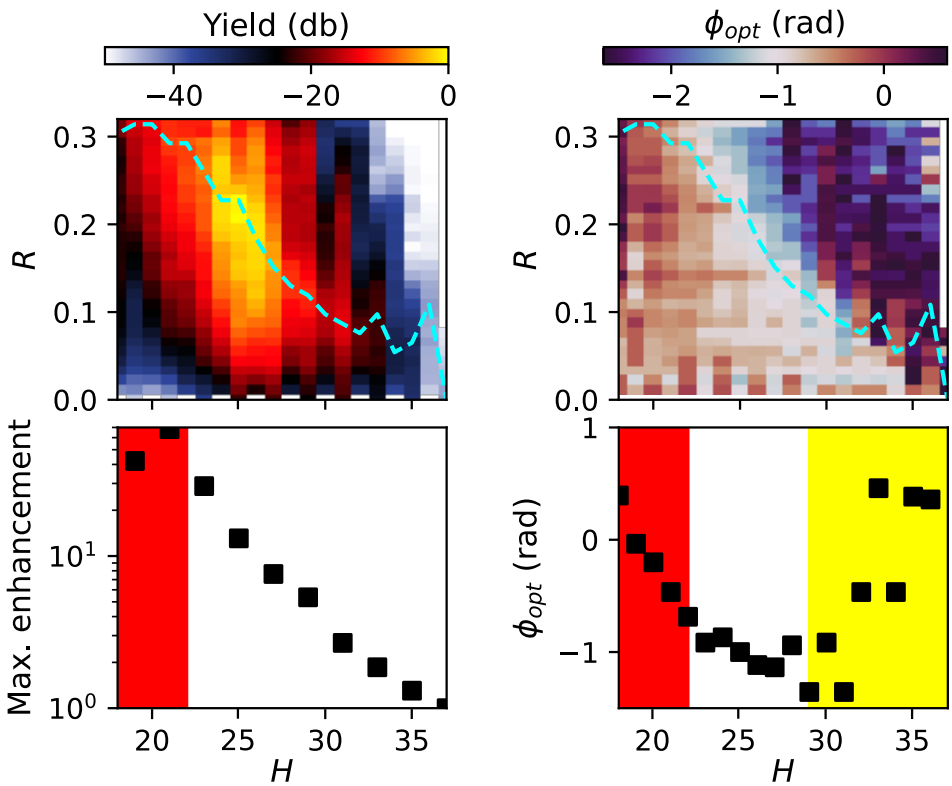

Figure 5.5: Maximum yield as a function of harmonic order H and R (top left). The dashed line goes through the maximum for each harmonic order, representing R_{opt} . The same line is shown on top of the optimum phase ϕ_{opt}, again as a function of R and H, at which the maximum yield is achieved (top right). The maximum enhancement value is steadily decreasing with harmonic order (bottom left). The overlap of the dashed line and ϕ_{opt} is extracted to highlight, that $\phi_{\text{opt}} \approx -1\,\text{rad}$ (bottom right) for a large number of harmonics. The red areas mark where a global optimum of R could not be reached. In the area marked with yellow, the XUV yield structure in Fig. 5.4 does not have a distinct global maximum.

is shown in a cyclic color scale. By overlaying the dashed line for the best yield enhancement on top, it becomes evident that the best enhancement is achieved for approximately the same phase over a large number of harmonics. The extracted ϕ_{opt} values corresponding to the dashed line are shown in the bottom right. For the white area, where a clear global maximum is visible (see also H22 - H29 in Fig. 5.4), $\phi_{\text{opt}} = \text{constant} \approx -1\,\text{rad}$.

In the red area, outside the experimental yield maximum range, ϕ_{opt} increases steadily. The yellow area are the harmonic orders where there is no distinct yield maximum (see also H30 - H37 in Fig. 5.4).

The same experiment was also conducted for $I_{\text{tot}} = 1.35 \times 10^{14}\,\text{W/cm}^2$, with identical findings of $\phi_{\text{opt}} = \text{constant} \approx -1\,\text{rad}$, but overall higher R_{opt}. This observation leads to the conclusion that there must be an optimization law connecting I_{tot} and R_{opt} for individual harmonic orders.

5.4 Towards an XUV yield optimization recipe

5.4.1 Two-color HHG in the semi-classical three-step model

The semi-classical three-step model [8], which is introduced in Sec. 2.8.1, is applied to the experimental conditions. The equation of motion, Eq. (2.39), is evaluated for the ponderomotive potential for the one-color case ($R = 0$) with $E = \sqrt{I/(\epsilon_0 c)}$ for $I = 0.9 \times 10^{14}\,\text{W/cm}^2$ and $\lambda = 1030\,\text{nm}$, $R = 0$ to 0.32 and $\phi = -\pi$ to π. The kinetic energy at the time of return T_R is added to the ionization potential I_p of argon ($15.6\,\text{eV}$ [160]) and is divided by $1.2\,\text{eV}$ to correspond to the respective harmonic order for $1030\,\text{nm}$.

Figure 5.6 shows this return energy in units of harmonic order as a color scale for four distinct second harmonic intensity fractions, $R = 0$, $R = 0.1$, $R = 0.2$ and $R = 0.3$, from left to right. The x-axis is the return time T_R given in units of the one-color laser cycle (T_ω), for one of the two electric field half-cycles. As ϕ has a range of 2π, the contribution of the other half-cycle corresponds to a phase shift of π.

For $R = 0$, the phase obviously does not have an influence. For increasing R, the return energies in one half-cycle decrease while in the other half-cyle they increase; see also Fig. 2.17. At $\phi = -1\,\text{rad}$, indicated by the cyan dashed line in Fig. 5.6 the return energy decrease is the strongest, flattening the peak until $R \approx 0.2$ before transitioning into an M-shape for $R > 0.2$, as seen in the line-outs of E_R corresponding to the cyan dashed line ($\phi = -1\,\text{rad}$) at the bottom. The position of the cutoff increase in the other half-cycle is indicated by the pink dashed line.

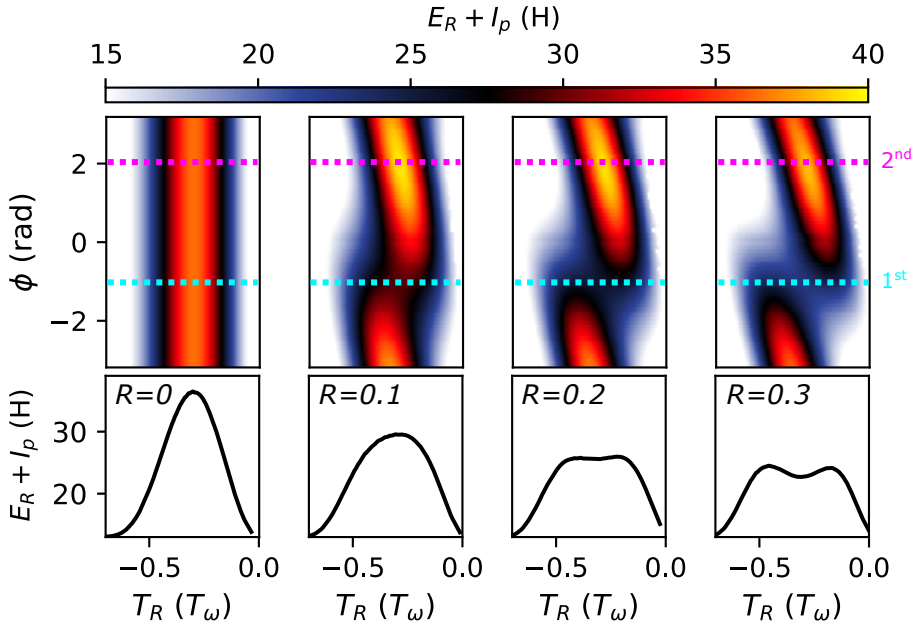

Figure 5.6: Return energy (color) in the unit of harmonic order (top) of electrons ionized during one electric field half-cycle for $R = 0$, $R = 0.1$, $R = 0.2$ and $R = 0.3$ (from left to right) as a function of phase ϕ and return time T_R. The cyan dashed line is located at $\phi_{\text{opt}} = -1\,\text{rad}$, corresponding to the first half-cycle. The pink dashed line highlights the corresponding second half-cycle, shifted by π. The values of E_R corresponding to the cyan line are plotted as line-outs (bottom).

Intuitively one would expect a higher XUV yield for harmonic orders in close proximity of a flattening in the time-energy curve, such as for $R = 0.2$, as more electrons return with the same energy compared to $R = 0$.

To derive a simple law relating I_{tot} and R to the location in energy of the flattening of the time-energy curve, we study the relation between the electric field at ω and 2ω and the return energies for $\phi = -1\,\text{rad}$, see Fig. 5.7.

On the top, the electric field contributions for ω (black) and 2ω (green) for an exemplary ratio of $R = 0.15$ are plotted. The resulting total electric field (see Eq. (2.44)) is shown as the dashed line. Sharing the same time axis, the electron return energies, with the same color scale as in Fig. 5.6, are presented at the bottom. The return energies are now shown with respect to their time of ionization T_I. It is noticeable that the time of the flattening of the time-energy curve, which forms at $\phi = -1\,\text{rad}$, does not change significantly with R, highlighted by the solid lines for ionization (orange, $T_I = -0.930\,T_\omega$) and recombination (cyan, $T_R = -0.295\,T_\omega$).

Assuming that the ionization and recombination times remain constant for the electrons returning in the flattened region, independently of R, the return energies can be now calculated analytically. The absolute value of the velocity an electron acquires

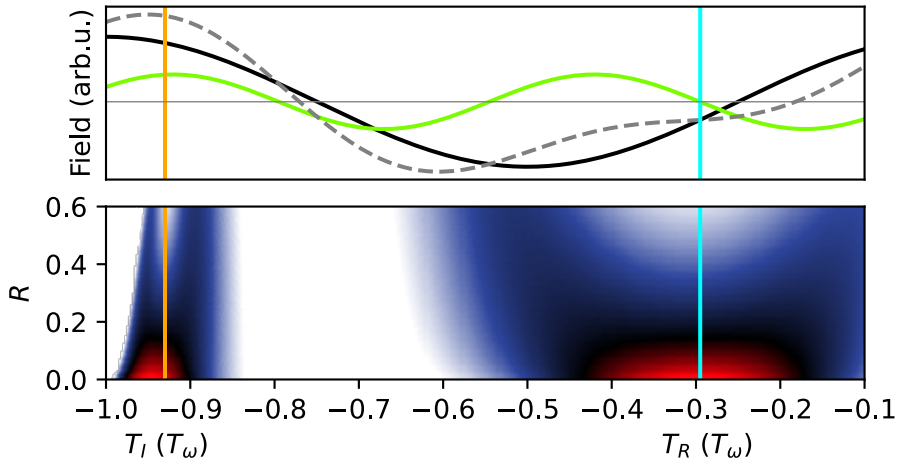

Figure 5.7: Electric field at $R = 0.3$ and $\phi = -1\,\mathrm{rad}$ (top). The green and black line represent the ω and 2ω contributions, the dashed line the total electric field. The return energies as a function of R at $\phi = -1\,\mathrm{rad}$ with respect to ionization time T_I and return time T_R (bottom) are shown sharing the same color scale as in Fig. 5.6. The approximately constant flattening location with respect to ionization (orange) and return (cyan) is highlighted with solid lines.

in an electric field is calculated by

$$v = \frac{p}{m_2} = -e \int_{T_I}^{T_R} \frac{E}{m_e} dt \tag{5.2}$$

The orange line in Fig. 5.7 is very close to the ionization time, where for $R = 0$ the maximum energy according to Eq. (2.41) is reached, almost perfectly coinciding with the cutoff energy return time (cyan line). For the ω contribution, the relation

$$\Delta v_\omega = -\sqrt{\frac{2}{m_e} \cdot 3.17 U_p \cdot (1 - R)} \tag{5.3}$$

holds. For the 2ω contribution, the orange line coincides with the peak of the field, and the cyan line with the zero crossing. The integral in Eq. (5.2) is therefore easily solvable, using the definition of U_p (see Eq.(2.40)) with the result

$$\Delta v_{2\omega} = \frac{e\sqrt{R I_{\mathrm{tot}}}}{m_e 2\omega} = \sqrt{\frac{R U_p}{m_e}}\,. \tag{5.4}$$

Adding the contributions of both colors together, we arrive at the kinetic energy $(\Delta v_\omega + \Delta v_{2\omega})^2/(2m_e)$ of an electron landing in the flattened region. The corresponding emitted XUV photon energy then reads

$$
\begin{aligned}
E_H &= I_p + \frac{1}{2} m_e (\Delta v_\omega + \Delta v_{2\omega})^2 \\
&= I_p + \frac{1}{2} U_p \left(\sqrt{2 \cdot 3.17 \cdot (1 - R)} - \sqrt{R} \right)^2 .
\end{aligned}
\tag{5.5}
$$

5.4.2 Comparison of experiment and theory

Figure 5.8 shows the comparison between Eq. 5.5 (dashed lines) and the experimental results (triangles) for two different I_{tot}, with excellent agreement. The shaded areas represent the effect of a 10 % change of I_{tot} and R in the theory. The experimental data points are only shown for harmonic orders where a global yield maximum has been reached. For $I_{\text{tot}} = 0.9 \times 10^{14}\,\text{W/cm}^2$ (red), the experimental range reaches $R = 0.32$ and $R = 0.2$ for $I_{\text{tot}} = 1.35 \times 10^{14}\,\text{W/cm}^2$ (blue).

Harmonic orders higher than 38 could not be observed with this specific setup as the HHG chamber and grating configuration were initially designed to investigate low-order high harmonics.

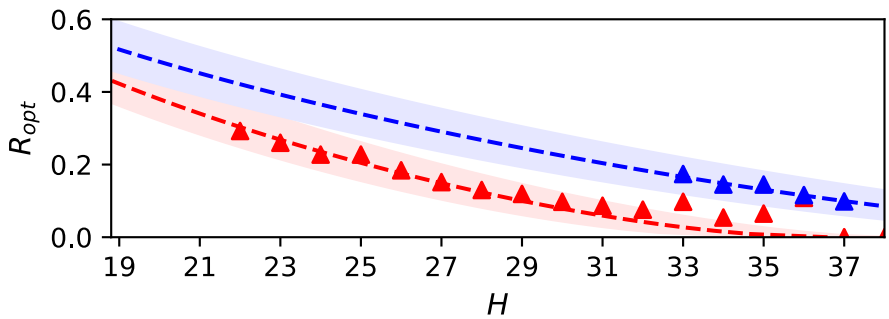

Figure 5.8: Comparison between the theory from Eq. (5.5) (dashed line) and experiment (triangles) for $I_{\text{tot}} = 0.9 \times 10^{14}\,\text{W/cm}^2$ (red) and $I_{\text{tot}} = 1.35 \times 10^{14}\,\text{W/cm}^2$ (blue).

5.4.3 Discussion and related work

According to the semi-classical three-step model, the yield at a certain energy is proportional to $(dE_R/dT_R)^{-1}$ [8] which is the inverse derivative of the time-energy curves of the returning electron after solving the equations of motion (see Eq. (2.39)). At the cutoff, which is the peak of the time-energy curve, the derivative becomes zero which leads to a singularity of the yield.

HHG with $\omega/2\omega$ at a fundamental of 800 nm with a pulse duration of 30 fs was studied in 2012 by Raz et al. [161]. In their experiment, strong enhancements of the

XUV yield were observed for certain regions of the HHG spectrum, which coincided with the relative phases and field ratios where local extrema occurred in the time-energy curves. The singularities were treated using catastrophe theory [162] which resulted in a diffraction pattern with local, strong enhancements in the form of caustics [163]. The strength of the enhancement depends on the degree of the singularity. In our trajectory analysis and ratio definition (see Eq. (2.43)), the ratio that yields the largest flattening and thus the highest degree of singularity according to [161] is at $R \approx 0.2$ (see bottom of Fig. 5.6). Compared to the yield in the experiment in Fig. 5.5, the highest overall yield was also achieved there. **Paper V** confirms the results of [161], concerning the relation between enhancement and time-energy curve "flatness".

The conclusions of **Paper V** with respect to XUV yield optimization using a laser field consisting of a fundamental ω and its second harmonic 2ω are summarized here:

- There is a maximum yield for a harmonic order, found where the return energy curve is flat at $\phi \approx -1\,\mathrm{rad}$.
- For a given harmonic order and $\mathrm{I_{tot}}$ there is a ratio R giving the maximum enhancement, which can be estimated by a simple formula given by Eq. (5.5).

Overall, the experimental results shown in Fig. 5.5 encompass much more than just XUV yield optimization. For example, at low ratios with $R < 0.05$ the phase jumps between odd and even harmonic orders are visible, related to interference effects [14]. The change of the optimum phase with harmonic order is evident as well by observing one row on the right of Fig. 5.5 for a specific R [142, 143]. In general, the experimental setup, discussed in detail in **Paper IV** provides a highly versatile tool to investigate two-color HHG.

5.4.4 Outlook on remaining research questions

Our discussions only considered HHG in terms of the single-atom response, disregarding phase matching effects [24].

The phase-matching conditions, see Eq. (2.42), change when varying phase and ratio as the ionization degree in the gas target is affected. The fairest comparison between single-color and multi-color HHG would be to compare the perfectly phase-matched optimized yields, by i.e. changing the gas pressure or the gas target length until a maximum yield is reached for each (R, ϕ).

In **Paper V** the generation conditions were left untouched when comparing $R = 0$ with $R \neq 0$ to ensure better reproducibility. Raz et al. also state, supported by

additional measurements in form of a pressure scan, that as long as the Rayleigh length z_R of the laser (see Eq. (2.18)) is significantly longer than the gas target, propagation effects can be neglected. This aligns with more recent phase-matching investigations, where HHG experimental setups are divided into two regimes, one with a long gas target length compared to z_R, and one with a short target [24]. A clear difference in sensitivity to pressure and intensity was observed in the two regimes, with short gas targets showing less dependence on gas pressure. As the setup in **Paper IV** also has a short gas target, phase-matching was not investigated further within **Paper V**. However, theoretical works on phase-matching with two-color HHG predict various effects and limitations that still need to be verified experimentally [164–166].

An additional, interesting study would be to test the effects of the relative beam sizes of ω and 2ω. The experiments shown in this section are carried out with a difference of 2 in focus size for ω and 2ω to reach higher values for R. So far, the variation in focus size is treated by calculating an average R over the whole beam profile. The validity of this assumption and the effect of changing the relative beam sizes should be tested in further studies.

Chapter 6

Summary & outlook

The work presented in this thesis is dedicated to the investigation of Yb-based laser sources for efficient high-order harmonic generation, via two different strategies:

1. Manipulating the HHG laser driver
2. Optimizing the HHG process itself

In this chapter, the findings of both strategies as well as the work on characterizing laser beams and pulses, which is equally important for laser development and for working with HHG, will be summarized and followed by an outlook on open questions and future projects.

6.1 Towards high peak and average power laser drivers for HHG using MPCs

For the first strategy, the focus is placed on pulse post-compression using bulk MPCs. Laser technology is slowly shifting from Ti:Sa to Yb-based systems, as Yb as a gain medium offers the ability to amplify the laser at much higher repetition rates, while also being significantly cheaper to operate. The largest drawback of Yb is the longer pulse duration. Post-compression offers a very efficient way to achieve shorter pulses by first broadening the spectrum due to the Kerr effect in a nonlinear medium and then compressing it in time by dispersion management.

In **Paper I** a bulk MPC is introduced, post-compressing 300 fs pulses at 370 MW input peak power to 31 fs, reaching > 2.5 GW at a repetition rate of 200 kHz with

a very compact experimental setup, built from standard components. Excellent pulse quality is also shown to be maintained, although the critical power for self-focusing in the glass plates is exceeded by a factor > 80. This work indicates that as long as material damage, ionization in air and beam collapse in the nonlinear material are avoided, even very large factors above the critical power for self-focusing do lead to a diminution of the output pulse quality.

For further output peak power scaling, where often gas-filled MPCs are employed, damage on the cell mirrors soon becomes the limiting factor. Experimental setups can be scaled up in size to increase the beam sizes and thus the peak fluence on the mirrors. The standard MPC configuration with two concave mirrors, however, soon reaches limits of practicality [70]. To counteract the setup size limits, alternative MPC geometries are currently investigated [97, 99] in addition to the folding approach discussed in **Paper VI**. Other strategies reduce the peak intensities in an MPC by dividing pulses in time [167] or by spatially redistributing the intensity in the beam profile [168].

These scaling possibilities constitute a very promising path to further explore Yb lasers followed by MPCs as HHG drivers, as they are able to efficiently deliver pulses with high peak powers at high repetition rate. In addition to a high XUV flux, high repetition rates also benefit applications relying on good statistics, such as electron-ion coincidence measurements [101]. Great potential also lies in the opportunity to easily tune the pulse duration with MPCs. For HHG, the optimal pulse duration to maximize the XUV conversion efficiency is currently under debate [169]. An MPC offers a great experimental investigation and verification tool, as the nonlinearity and thus the spectral broadening and minimum pulse duration can easily be tuned. In addition, the pulse duration can be varied independently of other parameters, such as the peak intensity or the beam size. Practically, this is achieved with an MPC, similar to the one presented in **Paper I** in combination with the HHG setup and the laser diagnostic part from **Paper IV**. Currently, the results of this HHG pulse duration study are being evaluated.

6.2 XUV flux enhancement with two-color HHG

Optimizing the HHG process itself can be divided into the interaction between the laser and a single atom emitting XUV radiation and propagation effects which depend on the geometry and density of the HHG target. The single-atom response is mainly governed by the scaling laws predicted by the semi-classical three-step model [8]. In **Paper V**, HHG is investigated using a two-color laser driver consisting of the fundamental and its second harmonic based on the experimental setup described in

Paper IV. The XUV yield of individual high harmonic orders at constant total intensity of the combined two colors was measured and compared to the single-color yield with identical intensity, while varying the relative phase and intensity ratio between the two colors. The optimum values for phase and ratio to achieve the highest XUV yield for the individual harmonic orders are determined experimentally. It is found that a global yield maximum always occurs at the same relative two-color phase, regardless of the total intensity. This maximum occurs when the return time vs. return energy curve calculated using the three-step model is flattening. Our results agree well with previous works linking yield enhancements to catastrophe theory that applies at singularities in the time-energy curves [161, 162]. Based on where the time-energy curves flatten, a simple equation is formulated connecting the total available laser intensity, fundamental wavelength, and the desired harmonic order to be maximized. The results of this derivation agree well with the experiment.

The influence of propagation effects with multi-color HHG is yet to be properly investigated. The setup in **Paper IV** offers nearly endless parameter control potential, especially due to to the spatial light modulators that are used to shape the individual focii. For **Paper V** the SLMs are only used for aberration correction, phase stabilization, and fine alignment. Improving the phase-matching conditions by spatially shaping the driving laser has been demonstrated in the past [170, 171] with a large potential for further optimization and broadening the knowledge and understanding of HHG. Currently, the setup in **Paper IV** is used in a study to control the XUV divergence by shaping the driving laser with the SLM, with the results being currently under investigation.

For further verification of the theory behind **Paper V**, a study of HHG with a ω-3ω interferometer are planned with a focus on not only enhancing the harmonic yield, but also the cutoff.

6.3 Pulse characterization

Lastly, to assess the quality of a laser during development and in HHG research, pulse characterization is mandatory. For the MPC project in **Paper I** that significantly extended the input peak power used for bulk MPCs, a valid concern was spatio-temporal couplings due to exceeding the critical power for self-focusing so many times. Using spatially-resolved Fourier transform spectrometry [128], it was shown that the MPC does not degrade the quality of the beam, in addition to the finding that the newly generated frequencies do not seem to inherit STCs from the input beam. The same method was also used to verify that several hundreds of mirror reflections in a folded MPC configuration in **Paper VI** do not deteriorate the beam quality.

For HHG, single-cycle laser pulses become interesting as they potentially enable isolated, single attosecond pulses with a continuous XUV spectrum. An alternative to the generation of single-cycle pulses is harnessing the polarization sensitivity of HHG, by creating a polarization gate where a few-cycle pulse is only linearly polarized in the middle; thus, only one half-cycle will contribute effectively to generate XUV. In **Paper II** the d-scan method [109] is extended to measure such a time-dependent polarization state.

As the carrier-envelope phase becomes a relevant parameter when using few-cycle pulses for HHG, measuring the CEP for every single pulse can be beneficial for CEP sensitive applications, such as photo-electron spectroscopy [101]. The challenge lies in providing a method that works at several hundreds of kHz without accumulating large amounts of data. In **Paper III** a measurement scheme is presented to obtain the CEP via optical Fourier transform. Single-shot analog CEP measurements were successfully demonstrated at 200 kHz. In principle, as this method relies only on measuring voltages after photodiodes, it can be scaled up to the MHz regime. Another interesting prospect is using this method in a feedback loop to CEP-stabilize not only the oscillator, but the entire laser chain, which has already been demonstrated with a stereo ATI [172].

Except for **Paper III**, all the methods described in Chapter 4 that were used throughout the thesis work and publications require many laser shots due to their scanning approach, involving delay and translation stages. Especially for very high peak-power laser systems towards the TW regime, pulse-to-pulse fluctuations in shape, duration, and other properties are not uncommon. Methods averaging over multiple shots may lead to misjudgment of the laser beam quality. For this reason, the demand for single-shot pulse characterization methods is steadily increasing. For measurements of the pulse duration, single-shot FROG [173] and single-shot d-scan [174] have already been demonstrated. More recently, a method that aims towards single-shot STC measurements has been presented [132]. The term "single-shot" herein usually refers to the data acquisition. The retrieval of the desired property from the data is usually performed in post-processing later on and can often take substantial computation time. Thus, a lot of potential lies in algorithm development, including artificial intelligence, which researchers have started exploring [175].

References

[1] M. Ferray, A. L'Huillier, X. F. Li, L. A. Lompre, G. Mainfray, and C. Manus. Multiple-harmonic conversion of 1064 nm radiation in rare gases. *Journal of Physics B: Atomic, Molecular and Optical Physics*, 21(3):L31, 1988.

[2] T. W. Hänsch. A proposed sub-femtosecond pulse synthesizer using separate phase-locked laser oscillators. *Optics Communications*, 80(1):71–75, 1990.

[3] M. Hentschel, R. Kienberger, C. Spielmann, G. A. Reider, N. Milosevic, T. Brabec, P. Corkum, U. Heinzmann, M. Drescher, and F. Krausz. Attosecond metrology. *Nature*, 414(6863):509–513, 2001.

[4] P. M. Paul, E. S. Toma, P. Breger, G. Mullot, F. Augé, Ph. Balcou, H. G. Muller, and P. Agostini. Observation of a train of attosecond pulses from high harmonic generation. *Science*, 292(5522):1689–1692, 2001.

[5] A. J. den Boef. Optical metrology of semiconductor wafers in lithography. In *International Conference on Optics in Precision Engineering and Nanotechnology*, 2013.

[6] C. Porter, T. Coenen, N. Geypen, S. Scholz, L. van Rijswijk, H.-K. Nienhuys, J. Ploegmakers, J. Reinink, H. Cramer, R. van Laarhoven, D. O'Dwyer, P. Smorenburg, A. Invernizzi, R. Wohrwag, H. Jonquiere, J. Reinhardt, O. el Gawhary, S. Mathijssen, P. Engblom, H. Chin, W. T. Blanton, S. Ganesan, B. Krist, F. Gstrein, and M. Phillips. Soft x-ray: novel metrology for 3d profilometry and device pitch overlay. In *Metrology, Inspection, and Process Control XXXVII*, volume 12496, pages 412–420, 2023.

[7] E. L. Falcão-Filho, V. M. Gkortsas, A. Gordon, and F. X. Kärtner. Analytic scaling analysis of high harmonic generation conversion efficiency. *Optics Express*, 17(13):11217–11229, 2009.

[8] P. B. Corkum. Plasma perspective on strong field multiphoton ionization. *Physical Review Letters*, 71(13):1994–1997, 1993.

[9] A. D. Shiner, C. Trallero-Herrero, N. Kajumba, H.-C. Bandulet, D. Comtois, F. Légaré, M. Giguère, J.-C. Kieffer, P. B. Corkum, and D. M. Villeneuve. Wavelength scaling of high harmonic generation efficiency. *Physical Review Letters*, 103(7):073902, 2009.

[10] J. Tate, T. Auguste, H. G. Muller, P. Salières, P. Agostini, and L. F. DiMauro. Scaling of wave-packet dynamics in an intense midinfrared field. *Physical Review Letters*, 98(1):013901, 2007.

[11] K. Midorikawa. Progress on table-top isolated attosecond light sources. *Nature Photonics*, 16(4):267–278, 2022.

[12] S. Watanabe, K. Kondo, Y. Nabekawa, A. Sagisaka, and Y. Kobayashi. Two-color phase control in tunneling ionization and harmonic generation by a strong laser field and its third harmonic. *Physical Review Letters*, 73(20):2692–2695, 1994.

[13] L. E. Chipperfield, J. S. Robinson, J. W. G. Tisch, and J. P. Marangos. Ideal waveform to generate the maximum possible electron recollision energy for any given oscillation period. *Physical Review Letters*, 102(6):063003, 2009.

[14] N. Dudovich, O. Smirnova, J. Levesque, Y. Mairesse, M. Yu. Ivanov, D. M. Villeneuve, and P. B. Corkum. Measuring and controlling the birth of attosecond XUV pulses. *Nature Physics*, 2(11):781–786, 2006.

[15] N. Dudovich, J. L. Tate, Y. Mairesse, D. M. Villeneuve, P. B. Corkum, and M. B. Gaarde. Subcycle spatial mapping of recollision dynamics. *Physical Review A*, 80(1):011806, 2009.

[16] M. Fieß, B. Horvath, T. Wittmann, W. Helml, Y. Cheng, B. Zeng, Z. Xu, A. Scrinzi, J. Gagnon, F. Krausz, and R. Kienberger. Attosecond control of tunneling ionization and electron trajectories. *New Journal of Physics*, 13(3):033031, 2011.

[17] D. Shafir, H. Soifer, B. D. Bruner, M. Dagan, Y. Mairesse, S. Patchkovskii, M. Y. Ivanov, O. Smirnova, and N. Dudovich. Resolving the time when an electron exits a tunnelling barrier. *Nature*, 485(7398):343–346, 2012.

[18] P. F. Moulton. Spectroscopic and laser characteristics of Ti:Al_2O_3. *JOSA B*, 3(1):125–133, 1986.

[19] H. Fattahi, H. G. Barros, M. Gorjan, T. Nubbemeyer, B. Alsaif, C. Y. Teisset, M. Schultze, S. Prinz, M. Haefner, M. Ueffing, A. Alismail, L. Vámos, A. Schwarz, O. Pronin, J. Brons, X. T. Geng, G. Arisholm, M. Ciappina,

V. S. Yakovlev, D.-E. Kim, A. M. Azzeer, N. Karpowicz, D. Sutter, Z. Major, T. Metzger, and F. Krausz. Third-generation femtosecond technology. *Optica*, 1(1):45–63, 2014.

[20] A. Dubietis, G. Jonušauskas, and A. Piskarskas. Powerful femtosecond pulse generation by chirped and stretched pulse parametric amplification in BBO crystal. *Optics Communications*, 88(4):437–440, 1992.

[21] T. Nagy, P. Simon, and L. Veisz. High-energy few-cycle pulses: post-compression techniques. *Advances in Physics: X*, 6(1):1845795, 2021.

[22] A.-L. Viotti, M. Seidel, E. Escoto, S. Rajhans, W. P. Leemans, I. Hartl, and C. M. Heyl. Multi-pass cells for post-compression of ultrashort laser pulses. *Optica*, 9(2):197, 2022.

[23] E. Constant, D. Garzella, P. Breger, E. Mével, Ch. Dorrer, C. Le Blanc, F. Salin, and P. Agostini. Optimizing high harmonic generation in absorbing gases: Model and experiment. *Physical Review Letters*, 82(8):1668–1671, 1999.

[24] R. Weissenbilder, S. Carlström, L. Rego, C. Guo, C. M. Heyl, P. Smorenburg, E. Constant, C. L. Arnold, and A. L'Huillier. How to optimize high-order harmonic generation in gases. *Nature Reviews Physics*, 4(11):713–722, 2022.

[25] B. E. A. Saleh and M. C. Teich. *Fundamentals of photonics*. 1991.

[26] W. G. Nagourney. *Quantum electronics for atomic physics and telecommunication*. 2014.

[27] I. Márton and L. Sarkadi. Study of the effect of higher-order dispersions on photoionisation induced by ultrafast laser pulses applying a classical theoretical method. *Scientific Reports*, 12(1):13841, 2022.

[28] K. Niu and C. Tian. Zernike polynomials and their applications. *Journal of Optics*, 24(12):123001, 2022.

[29] G. Kirchhoff. Zur Theorie der Lichtstrahlen. *Annalen der Physik*, 254(4):663–695, 1883.

[30] S. W. Jolly, O. Gobert, and F. Quéré. Spatio-temporal characterization of ultrashort laser beams: a tutorial. *Journal of Optics*, 22(10):103501, 2020.

[31] S. Akturk, X. Gu, P. Bowlan, and R. Trebino. Spatio-temporal couplings in ultrashort laser pulses. *Journal of Optics*, 12(9):093001, 2010.

[32] P. A. Franken, A. E. Hill, C. W. Peters, and G. Weinreich. Generation of optical harmonics. *Physical Review Letters*, 7(4):118–119, 1961.

[33] R. H. Stolen and C. Lin. Self-phase-modulation in silica optical fibers. *Physical Review A*, 17(4):1448–1453, 1978.

[34] R. W. Boyd, S. G. Lukishova, Y. Shen, and C. Ascheron, editors. *Self-focusing: Past and Present: Fundamentals and Prospects*, volume 114 of *Topics in Applied Physics*. New York, NY, 2009.

[35] C. Guo, A. Harth, S. Carlström, Y.-C. Cheng, S. Mikaelsson, E. Mårsell, C. Heyl, M. Miranda, M. Gisselbrecht, M. B. Gaarde, K. J. Schafer, A. Mikkelsen, J. Mauritsson, C. L. Arnold, and A. L'Huillier. Phase control of attosecond pulses in a train. *Journal of Physics B: Atomic, Molecular and Optical Physics*, 51(3):034006, 2018.

[36] T. Gaumnitz, A. Jain, Y. Pertot, M. Huppert, I. Jordan, F. Ardana-Lamas, and H. J. Wörner. Streaking of 43-attosecond soft-X-ray pulses generated by a passively cep-stable mid-infrared driver. *Optics Express*, 25(22):27506–27518, 2017.

[37] J. Li, X. Ren, Y. Yin, K. Zhao, A. Chew, Y. Cheng, E. Cunningham, Y. Wang, S. Hu, Y. Wu, M. Chini, and Z. Chang. 53-attosecond X-ray pulses reach the carbon k-edge. *Nature Communications*, 8(1):186, 2017.

[38] A. Ludwig, J. Maurer, B. W. Mayer, C. R. Phillips, L. Gallmann, and U. Keller. Breakdown of the dipole approximation in strong-field ionization. *Physical Review Letters*, 113(24):243001, 2014.

[39] E. Takahashi, Y. Nabekawa, T. Otsuka, M. Obara, and K. Midorikawa. Generation of highly coherent submicrojoule soft x rays by high-order harmonics. *Physical Review A*, 66(2):021802, 2002.

[40] A. Einstein. Zur Quantentheorie der Strahlung. *Physika Zeitschrift*, 18:121–128, 1917.

[41] T. H. Maiman. Stimulated optical radiation in ruby. *Nature*, 187(4736):493–494, 1960.

[42] D. Strickland and G. Mourou. Compression of amplified chirped optical pulses. *Optics Communications*, 55(6):447–449, 1985.

[43] N. M. Kroll. Parametric amplification in spatially extended media and application to the design of tuneable oscillators at optical frequencies. *Physical Review*, 127(4):1207–1211, 1962.

[44] J. A. Giordmaine and R. C. Miller. Tunable coherent parametric oscillation in $LiNbO_3$ at optical frequencies. *Physical Review Letters*, 14(24):973–976, 1965.

[45] T. Wilhelm, J. Piel, and E. Riedle. Sub-20-fs pulses tunable across the visible from a blue-pumped single-pass noncollinear parametric converter. *Optics Letters*, 22(19):1494–1496, 1997.

[46] W. Li, Z. Gan, L. Yu, C. Wang, Y. Liu, Z. Guo, L. Xu, M. Xu, Y. Hang, Y. Xu, J. Wang, P. Huang, H. Cao, B. Yao, X. Zhang, L. Chen, Y. Tang, S. Li, X. Liu, S. Li, M. He, D. Yin, X. Liang, Y. Leng, R. Li, and Z. Xu. 339 J high-energy Ti:sapphire chirped-pulse amplifier for 10 PW laser facility. *Optics Letters*, 43(22):5681–5684, 2018.

[47] A. Harth, C. Guo, Y.-C. Cheng, A. Losquin, M. Miranda, S. Mikaelsson, C. M. Heyl, O. Prochnow, J. Ahrens, U. Morgner, A. L'Huillier, and C. L. Arnold. Compact 200 kHz HHG source driven by a few-cycle opcpa. *Journal of Optics*, 20(1):014007, 2017.

[48] E. Sorokin. In *Few-Cycle Laser Pulse Generation and Its Applications*. 2004.

[49] J. Koerner, C. Vorholt, H. Liebetrau, M. Kahle, D. Kloepfel, R. Seifert, J. Hein, and M. C. Kaluza. Measurement of temperature-dependent absorption and emission spectra of Yb:YAG, Yb:LuAG, and Yb:CaF_2 between 20 °c and 200 °C and predictions on their influence on laser performance. *JOSA B*, 29(9):2493–2502, 2012.

[50] I. Sytcevich, A.-L. Viotti, C. Guo, J. Vogelsang, F. Langer, A. L'Huillier, and C. L. Arnold. Few-cycle short-wave-infrared light source for strong-field experiments at 200 kHz repetition rate. *Optics Express*, 30(15):27858–27867, 2022.

[51] E. Shestaev, S. Hädrich, N. Walther, T. Eidam, A. Klenke, I. Seres, Z. Bengery, P. Jójárt, Z. Várallyay, Á. Börzsönyi, and J. Limpert. Carrier-envelope offset stable, coherently combined ytterbium-doped fiber CPA delivering 1 kW of average power. *Optics Letters*, 45(23):6350–6353, 2020.

[52] P. Russbueldt, T. Mans, G. Rotarius, J. Weitenberg, H. D. Hoffmann, and R. Poprawe. 400 W Yb:YAG innoslab fs-amplifier. *Optics Express*, 17(15):12230–12245, 2009.

[53] S. Goncharov, K. Fritsch, and O. Pronin. 110 MW thin-disk oscillator. *Optics Express*, 31(16):25970–25977, 2023.

[54] M. E. V. Pedersen, M. M. Johansen, A. S. Olesen, M. Michieletto, M. Gaponenko, and M. D. Maack. 175 W average power from a single-core rod fiber-based chirped-pulse-amplification system. *Optics Letters*, 47(19):5172–5175, 2022.

[55] G. Sansone, E. Benedetti, F. Calegari, C. Vozzi, L. Avaldi, R. Flammini, L. Poletto, P. Villoresi, C. Altucci, R. Velotta, S. Stagira, S. De Silvestri, and M. Nisoli. Isolated single-cycle attosecond pulses. *Science*, 314(5798):443–446, 2006.

[56] J. C. Knight, T. A. Birks, P. S. J. Russell, and D. M. Atkin. All-silica single-mode optical fiber with photonic crystal cladding. *Optics Letters*, 21(19):1547–1549, 1996.

[57] M. Nisoli, S. De Silvestri, and O. Svelto. Generation of high energy 10 fs pulses by a new pulse compression technique. *Applied Physics Letters*, 68(20):2793–2795, 1996.

[58] M. Nisoli, S. D. Silvestri, O. Svelto, R. Szipöcs, K. Ferencz, C. Spielmann, S. Sartania, and F. Krausz. Compression of high-energy laser pulses below 5 fs. *Optics Letters*, 22(8):522–524, 1997.

[59] T. Nagy, M. Forster, and P. Simon. Flexible hollow fiber for pulse compressors. *Applied Optics*, 47(18):3264–3268, 2008.

[60] T. Nagy, M. Kretschmar, M. J. J. Vrakking, and A. Rouzée. Generation of above-terawatt 1.5-cycle visible pulses at 1 kHz by post-compression in a hollow fiber. *Optics Letters*, 45(12):3313–3316, 2020.

[61] G. Fan, P. A. Carpeggiani, Z. Tao, G. Coccia, R. Safaei, E. Kaksis, A. Pugzlys, F. Légaré, B. E. Schmidt, and A. Baltuška. 70 mJ nonlinear compression and scaling route for an Yb amplifier using large-core hollow fibers. *Optics Letters*, 46(4):896–899, 2021.

[62] C.-H. Lu, Y.-J. Tsou, H.-Y. Chen, B.-H. Chen, Y.-C. Cheng, S.-D. Yang, M.-C. Chen, C.-C. Hsu, and A. H. Kung. Generation of intense supercontinuum in condensed media. *Optica*, 1(6):400–406, 2014.

[63] C.-H. Lu, W.-H. Wu, S.-H. Kuo, J.-Y. Guo, M.-C. Chen, S.-D. Yang, and A. H. Kung. Greater than 50 times compression of 1030 nm Yb:KGW laser pulses to single-cycle duration. *Optics Express*, 27(11):15638–15648, 2019.

[64] C.-H. Lu, T. Witting, A. Husakou, M. J. J. Vrakking, A. H. Kung, and F. J. Furch. Sub-4 fs laser pulses at high average power and high repetition rate from an all-solid-state setup. *Optics Express*, 26(7):8941–8956, 2018.

[65] J. Schulte, T. Sartorius, J. Weitenberg, A. Vernaleken, and P. Russbueldt. Nonlinear pulse compression in a multi-pass cell. *Optics Letters*, 41(19):4511, 2016.

[66] J. U. White. Long optical paths of large aperture. *JOSA*, 32(5):285–288, 1942.

[67] D. Herriott, H. Kogelnik, and R. Kompfner. Off-axis paths in spherical mirror interferometers. *Applied Optics*, 3(4):523–526, 1964.

[68] L. Lavenu, M. Natile, F. Guichard, Y. Zaouter, X. Delen, M. Hanna, E. Mottay, and P. Georges. Nonlinear pulse compression based on a gas-filled multipass cell. *Optics Letters*, 43(10):2252, 2018.

[69] M. Ueffing, S. Reiger, M. Kaumanns, V. Pervak, M. Trubetskov, T. Nubbemeyer, and F. Krausz. Nonlinear pulse compression in a gas-filled multipass cell. *Optics Letters*, 43(9):2070, 2018.

[70] Y. Pfaff, G. Barbiero, M. Rampp, S. Klingebiel, J. Brons, C. Y. Teisset, H. Wang, R. Jung, J. Jaksic, A. H. Woldegeorgis, M. Trunk, A. R. Maier, C. J. Saraceno, and T. Metzger. Nonlinear pulse compression of a 200 mJ and 1 kW ultrafast thin-disk amplifier. *Optics Express*, 31(14):22740, 2023.

[71] C. Grebing, M. Müller, J. Buldt, H. Stark, and J. Limpert. Kilowatt-average-power compression of millijoule pulses in a gas-filled multi-pass cell. *Optics Letters*, 45(22):6250, 2020.

[72] M. Kaumanns, V. Pervak, D. Kormin, V. Leshchenko, A. Kessel, M. Ueffing, Y. Chen, and T. Nubbemeyer. Multipass spectral broadening of 18 mJ pulses compressible from 13 ps to 41 fs. *Optics Letters*, 43(23):5877, 2018.

[73] M. Seidel, P. Balla, C. Li, G. Arisholm, L. Winkelmann, I. Hartl, and C. M. Heyl. Factor 30 pulse compression by hybrid multipass multiplate spectral broadening. *Ultrafast Science*, 2022:2022/9754919, 2022.

[74] M. Hanna, F. Guichard, N. Daher, Q. Bournet, X. Délen, and P. Georges. Nonlinear optics in multipass cells. *Laser & Photonics Reviews*, 15(12):2100220, 2021.

[75] R. Szipöcs, K. Ferencz, C. Spielmann, and F. Krausz. Chirped multilayer coatings for broadband dispersion control in femtosecond lasers. *Optics Letters*, 19(3):201–203, 1994.

[76] E. Treacy. Optical pulse compression with diffraction gratings. *IEEE Journal of Quantum Electronics*, 5(9):454–458, 1969.

[77] G. Jargot, N. Daher, L. Lavenu, X. Delen, N. Forget, M. Hanna, and P. Georges. Self-compression in a multipass cell. *Optics Letters*, 43(22):5643, 2018.

[78] L. Silletti, A. Bin Wahid, E. Escoto, P. Balla, S. Rajhans, K. Horn, L. Winkelmann, V. Wanie, A. Trabattoni, C. M. Heyl, and F. Calegari. Dispersion-engineered multi-pass cell for single-stage post-compression of an ytterbium laser. *Optics Letters*, 48(7):1842, 2023.

[79] N. L. Wagner, E. A. Gibson, T. Popmintchev, I. P. Christov, M. M. Murnane, and H. C. Kapteyn. Self-compression of ultrashort pulses through ionization-induced spatiotemporal reshaping. *Physical Review Letters*, 93(17):173902, 2004.

[80] C. P. Hauri, A. Trisorio, M. Merano, G. Rey, R. B. Lopez-Martens, and G. Mourou. Generation of high-fidelity, down-chirped sub-10fs mJ pulses through filamentation for driving relativistic laser-matter interactions at 1 kHz. *Applied Physics Letters*, 89(15):151125, 2006.

[81] Á. Börzsönyi, Z. Heiner, A. P. Kovács, M. P. Kalashnikov, and K. Osvay. Measurement of pressure dependent nonlinear refractive index of inert gases. *Optics Express*, 18(25):25847–25854, 2010.

[82] G. Fibich and A. L. Gaeta. Critical power for self-focusing in bulk media and in hollow waveguides. *Optics Letters*, 25(5):335–337, 2000.

[83] M. Hanna, L. Daniault, F. Guichard, N. Daher, X. Délen, R. Lopez-Martens, and P. Georges. Nonlinear beam matching to gas-filled multipass cells. *OSA Continuum*, 4(2):732, 2021.

[84] J. Weitenberg, A. Vernaleken, J. Schulte, A. Ozawa, T. Sartorius, V. Pervak, H.-D. Hoffmann, T. Udem, P. Russbüldt, and T. W. Hänsch. Multi-pass-cell-based nonlinear pulse compression to 115 fs at 7.5 µj pulse energy and 300 w average power. *Optics Express*, 25(17):20502–20510, 2017.

[85] K. Fritsch, M. Poetzlberger, V. Pervak, J. Brons, and O. Pronin. All-solid-state multipass spectral broadening to sub-20 fs. *Optics Letters*, 43(19):4643, 2018.

[86] C.-L. Tsai, F. Meyer, A. Omar, Y. Wang, A.-Y. Liang, C.-H. Lu, M. Hoffmann, S.-D. Yang, and C. J. Saraceno. Efficient nonlinear compression of a mode-locked thin-disk oscillator to 27 fs at 98 W average power. *Optics Letters*, 44(17):4115, 2019.

[87] G. Barbiero, H. Wang, J. Brons, B.-H. Chen, V. Pervak, and H. Fattahi. Broadband terahertz solid-state emitter driven by Yb:YAG thin-disk oscillator. *Journal of Physics B: Atomic, Molecular and Optical Physics*, 53(12):125601, 2020.

[88] F. Meyer, T. Vogel, S. Ahmed, and C. J. Saraceno. Single-cycle, MHz repetition rate THz source with 66 mW of average power. *Optics Letters*, 45(9):2494, 2020.

[89] E. Vicentini, Y. Wang, D. Gatti, A. Gambetta, P. Laporta, G. Galzerano, K. Curtis, K. McEwan, C. R. Howle, and N. Coluccelli. Nonlinear pulse compression to 22 fs at 15.6 µJ by an all-solid-state multipass approach. *Optics Express*, 28(4):4541, 2020.

[90] G. Barbiero, H. Wang, M. Graßl, S. Gröbmeyer, D. Kimbaras, M. Neuhaus, V. Pervak, T. Nubbemeyer, H. Fattahi, and M. F. Kling. Efficient nonlinear compression of a thin-disk oscillator to 8.5 fs at 55 W average power. *Optics Letters*, 46(21):5304, 2021.

[91] M. Seidel, F. Pressacco, O. Akcaalan, T. Binhammer, J. Darvill, N. Ekanayake, M. Frede, U. Grosse-Wortmann, M. Heber, C. M. Heyl, D. Kutnyakhov, C. Li, C. Mohr, J. Müller, O. Puncken, H. Redlin, N. Schirmel, S. Schulz, A. Swiderski, H. Tavakol, H. Tünnermann, C. Vidoli, L. Wenthaus, N. Wind, L. Winkelmann, B. Manschwetus, and I. Hartl. Ultrafast mhz-rate burst-mode pump–probe laser for the FLASH FEL facility based on nonlinear compression of ps-level pulses from an Yb-amplifier chain. *Laser & Photonics Reviews*, 16(3):2100268, 2022.

[92] A.-L. Viotti, C. Li, G. Arisholm, L. Winkelmann, I. Hartl, C. M. Heyl, and M. Seidel. Few-cycle pulse generation by double-stage hybrid multi-pass multi-plate nonlinear pulse compression. *Optics Letters*, 48(4):984, 2023.

[93] A. Omar, M. Hoffmann, G. Galle, F. Sylla, and C. J. Saraceno. Hybrid air-bulk multi-pass cell compressor for high pulse energies with full spatio-temporal characterization. *Optics Express*, 32(8):13235, 2024.

[94] S. Hädrich, E. Shestaev, M. Tschernajew, F. Stutzki, N. Walther, F. Just, M. Kienel, I. Seres, P. Jójárt, Z. Bengery, B. Gilicze, Z. Várallyay, Á. Börzsönyi, M. Müller, C. Grebing, A. Klenke, D. Hoff, G. G. Paulus, T. Eidam, and J. Limpert. Carrier-envelope phase stable few-cycle laser system delivering more than 100 W, 1 mJ, sub-2-cycle pulses. *Optics Letters*, 47(6):1537, 2022.

[95] S. Westerberg. *in preparation*, 2024.

[96] M. Hanna, X. Délen, L. Lavenu, F. Guichard, Y. Zaouter, F. Druon, and P. Georges. Nonlinear temporal compression in multipass cells: theory. *Journal of the Optical Society of America B*, 34(7):1340, 2017.

[97] V. Hariton, K. Fritsch, K. Schwarz, N. Kovalenko, G. Figueira, G. Arisholm, and O. Pronin. Spectral broadening in convex-concave multipass cells. *Optics Express*, 31(12):19554, 2023.

[98] A. Omar, T. Vogel, M. Hoffmann, and C. J. Saraceno. Spectral broadening of 2 mJ femtosecond pulses in a compact air-filled convex–concave multi-pass cell. *Optics Letters*, 48(6):1458–1461, 2023.

[99] C. M. Heyl, M. Seidel, E. Escoto, A. Schönberg, S. Carlström, G. Arisholm, T. Lang, and I. Hartl. High-energy bow tie multi-pass cells for nonlinear spectral broadening applications. *Journal of Physics: Photonics*, 4(1):014002, 2022.

[100] R. Wallauer, M. Raths, K. Stallberg, L. Münster, D. Brandstetter, X. Yang, J. Güdde, P. Puschnig, S. Soubatch, C. Kumpf, F. C. Bocquet, F. S. Tautz, and U. Höfer. Tracing orbital images on ultrafast time scales. *Science*, 371(6533):1056–1059, 2021.

[101] S. Mikaelsson, J. Vogelsang, C. Guo, I. Sytcevich, A.-L. Viotti, F. Langer, Y.-C. Cheng, S. Nandi, W. Jin, A. Olofsson, R. Weissenbilder, J. Mauritsson, A. L'Huillier, M. Gisselbrecht, and C. L. Arnold. A high-repetition rate attosecond light source for time-resolved coincidence spectroscopy. *Nanophotonics*, 10(1):117–128, 2021.

[102] T. Gorkhover, A. Ulmer, K. Ferguson, M. Bucher, F. R. N. C. Maia, J. Bielecki, T. Ekeberg, M. F. Hantke, B. J. Daurer, C. Nettelblad, J. Andreasson, A. Barty, P. Bruza, S. Carron, D. Hasse, J. Krzywinski, D. S. D. Larsson, A. Morgan, K. Mühlig, M. Müller, K. Okamoto, A. Pietrini, D. Rupp, M. Sauppe, G. van der Schot, M. Seibert, J. A. Sellberg, M. Svenda, M. Swiggers, N. Timneanu, D. Westphal, G. Williams, A. Zani, H. N. Chapman, G. Faigel, T. Möller, J. Hajdu, and C. Bostedt. Femtosecond X-ray fourier holography imaging of free-flying nanoparticles. *Nature Photonics*, 12(3):150–153, 2018.

[103] A. E. Siegman. How to (maybe) measure laser beam quality. In *Diode Pumped Solid State Lasers: Applications and Issues*, 1998.

[104] A. E. Siegman. Defining, measuring, and optimizing laser beam quality. In *Laser Resonators and Coherent Optics: Modeling, Technology, and Applications*, 1993.

[105] R. W. Gerchberg. A practical algorithm for the determination of phase from image and diffraction plane pictures. *Optik*, 1972.

[106] L. J. Allen and M. P. Oxley. Phase retrieval from series of images obtained by defocus variation. *Optics Communications*, 199(1):65–75, 2001.

[107] J. A. Armstrong. Measurement of picosecond laser pulse widths. *Applied Physics Letters*, 10(1):16–18, 1967.

[108] R. Trebino and D. J. Kane. Using phase retrieval to measure the intensity and phase of ultrashort pulses: frequency-resolved optical gating. *JOSA A*, 10(5):1101–1111, 1993.

[109] M. Miranda, T. Fordell, C. Arnold, A. L'Huillier, and H. Crespo. Simultaneous compression and characterization of ultrashort laser pulses using chirped mirrors and glass wedges. *Optics Express*, 20(1):688–697, 2012.

[110] C. Iaconis and I. A. Walmsley. Spectral phase interferometry for direct electric-field reconstruction of ultrashort optical pulses. *Optics Letters*, 23(10):792–794, 1998.

[111] M. Miranda, C. L. Arnold, T. Fordell, F. Silva, B. Alonso, R. Weigand, A. L'Huillier, and H. Crespo. Characterization of broadband few-cycle laser pulses with the d-scan technique. *Optics Express*, 20(17):18732–18743, 2012.

[112] I. Sytcevich, C. Guo, S. Mikaelsson, J. Vogelsang, A.-L. Viotti, B. Alonso, R. Romero, P. T. Guerreiro, Í. J. Sola, A. L'Huillier, H. Crespo, M. Miranda, and C. L. Arnold. Characterizing ultrashort laser pulses with second harmonic dispersion scans. *JOSA B*, 38(5):1546–1555, 2021.

[113] M. Kakehata, R. Ueda, H. Takada, K. Torizuka, and M. Obara. Combination of high-intensity femtosecond laser pulses for generation of time-dependent polarization pulses and ionization of atomic gas. *Applied Physics B*, 70(1):S207–S213, 2000.

[114] K. S. Budil, P. Salières, A. L'Huillier, T. Ditmire, and M. D. Perry. Influence of ellipticity on harmonic generation. *Physical Review A*, 48(5):R3437–R3440, 1993.

[115] C. Altucci, C. Delfin, L. Roos, M. B. Gaarde, A. L'Huillier, I. Mercer, T. Starczewski, and C.-G. Wahlström. Frequency-resolved time-gated high-order harmonics. *Physical Review A*, 58(5):3934–3941, 1998.

[116] O. Tcherbakoff, E. Mével, D. Descamps, J. Plumridge, and E. Constant. Time-gated high-order harmonic generation. *Physical Review A*, 68(4):043804, 2003.

[117] L. Chen, P. Huo, J. Song, Z. Wang, T. Xu, W. Zhu, and A. Agrawal. Shaping polarization within an ultrafast laser pulse using dielectric metasurfaces. *Optica*, 10(1):26–32, 2023.

[118] S. M. Weber, F. Weise, M. Plewicki, and A. Lindinger. Interferometric generation of parametrically shaped polarization pulses. *Applied Optics*, 46(23):5987–5990, 2007.

[119] A. J. Duncan, A. Finch, and W. Sibbett. The effect of optically active devices on the polarisation properties of ultrashort pulses. *Journal of Physics B: Atomic, Molecular and Optical Physics*, 23(3):611, 1990.

[120] D. Kupka, P. Schlup, and R. A. Bartels. Simplified ultrafast pulse shaper for tailored polarization states using a birefringent prism. *Review of Scientific Instruments*, 80(5):053110, 2009.

[121] A. E. Paul, J. A. Bolger, A. L. Smirl, and J. G. Pellegrino. Time-resolved measurements of the polarization state of four-wave mixing signals from gaas multiple quantum wells. *JOSA B*, 13(5):1016–1025, 1996.

[122] W. J. Walecki, D. N. Fittinghoff, A. L. Smirl, and R. Trebino. Characterization of the polarization state of weak ultrashort coherent signals by dual-channel spectral interferometry. *Optics Letters*, 22(2):81–83, 1997.

[123] R. Boge, S. Heuser, M. Sabbar, M. Lucchini, L. Gallmann, C. Cirelli, and U. Keller. Revealing the time-dependent polarization of ultrashort pulses with sub-cycle resolution. *Optics Express*, 22(22):26967–26975, 2014.

[124] B. Alonso, W. Holgado, and Í. J. Sola. Compact in-line temporal measurement of laser pulses with amplitude swing. *Optics Express*, 28(10):15625–15640, 2020.

[125] C. Barbero, B. Alonso, and Í. J. Sola. Characterization of ultrashort vector pulses from a single amplitude swing measurement. *Optics Express*, 32(7):10862–10873, 2024.

[126] P. Schlup, O. Masihzadeh, L. Xu, R. Trebino, and R. A. Bartels. Tomographic retrieval of the polarization state of an ultrafast laser pulse. *Optics Letters*, 33(3):267–269, 2008.

[127] V. Leroux, T. Eichner, and A. R. Maier. Description of spatio-temporal couplings from heat-induced compressor grating deformation. *Optics Express*, 28(6):8257–8265, 2020.

[128] M. Miranda, M. Kotur, P. Rudawski, C. Guo, A. Harth, A. L'Huillier, and C. L. Arnold. Spatiotemporal characterization of ultrashort laser pulses using spatially resolved fourier transform spectrometry. *Optics Letters*, 39(17):5142–5145, 2014.

[129] G. Pariente, V. Gallet, A. Borot, O. Gobert, and F. Quéré. Space–time characterization of ultra-intense femtosecond laser beams. *Nature Photonics*, 10(8):547–553, 2016.

[130] A. Borot and F. Quéré. Spatio-spectral metrology at focus of ultrashort lasers: a phase-retrieval approach. *Optics Express*, 26(20):26444–26461, 2018.

[131] T. Witting, S. J. Weber, J. W. G. Tisch, and J. P. Marangos. Spatio-temporal characterization of mid-infrared laser pulses with spatially encoded spectral shearing interferometry. *Optics Express*, 20(27):27974–27980, 2012.

[132] S. Smartsev, A. Liberman, I. A. Andriyash, A. Cavagna, A. Flacco, C. Giaccaglia, J. Kaur, J. Monzac, S. Tata, A. Vernier, V. Malka, R. Lopez-Martens, and J. Faure. Simple few-shot method for spectrally resolving the wavefront of an ultrashort laser pulse. *Optics Letters*, 49(8):1900–1903, 2024.

[133] N. Ishii, K. Kaneshima, K. Kitano, T. Kanai, S. Watanabe, and J. Itatani. Carrier-envelope phase-dependent high harmonic generation in the water window using few-cycle infrared pulses. *Nature Communications*, 5(1):3331, 2014.

[134] E. Cormier and P. Lambropoulos. Effect of the initial phase of the field in ionization by ultrashort laser pulses. *The European Physical Journal D - Atomic, Molecular, Optical and Plasma Physics*, 2(1):15–20, 1998.

[135] E. Goulielmakis, M. Uiberacker, R. Kienberger, A. Baltuska, V. Yakovlev, A. Scrinzi, Th. Westerwalbesloh, U. Kleineberg, U. Heinzmann, M. Drescher, and F. Krausz. Direct measurement of light waves. *Science*, 305(5688):1267–1269, 2004.

[136] S. B. Park, K. Kim, W. Cho, S. I. Hwang, I. Ivanov, C. H. Nam, and K. T. Kim. Direct sampling of a light wave in air. *Optica*, 5(4):402–408, 2018.

[137] S. Keiber, S. Sederberg, A. Schwarz, M. Trubetskov, V. Pervak, F. Krausz, and N. Karpowicz. Electro-optic sampling of near-infrared waveforms. *Nature Photonics*, 10(3):159–162, 2016.

[138] D. Hoff, F. J. Furch, T. Witting, K. Rühle, D. Adolph, A. M. Sayler, M. J. J. Vrakking, G. G. Paulus, and C. P. Schulz. Continuous every-single-shot carrier-envelope phase measurement and control at 100 kHz. *Optics Letters*, 43(16):3850–3853, 2018.

[139] M. Kakehata, H. Takada, Y. Kobayashi, K. Torizuka, Y. Fujihira, T. Homma, and H. Takahashi. Single-shot measurement of carrier-envelope phase changes by spectral interferometry. *Optics Letters*, 26(18):1436–1438, 2001.

[140] H. Telle, G. Steinmeyer, A. Dunlop, J. Stenger, D. Sutter, and U. Keller. Carrier-envelope offset phase control: A novel concept for absolute optical frequency measurement and ultrashort pulse generation. *Applied Physics B*, 69(4):327–332, 1999.

[141] M. Kurucz, S. Tóth, R. Flender, L. Haizer, B. Kiss, B. Persielle, and E. Cormier. Single-shot cep drift measurement at arbitrary repetition rate based on dispersive fourier transform. *Optics Express*, 27(9):13387–13399, 2019.

[142] U. Andiel, G. D. Tsakiris, E. Cormier, and K. Witte. High-order harmonic amplitude modulation in two-colour phase-controlled frequency mixing. *Europhysics Letters*, 47(1):42, 1999.

[143] C. Figueira De Morisson Faria, D. B. Milošević, and G. G. Paulus. Phase-dependent effects in bichromatic high-order harmonic generation. *Physical Review A*, 61(6):063415, 2000.

[144] N. Ishii, A. Kosuge, T. Hayashi, T. Kanai, J. Itatani, S. Adachi, and S. Watanabe. Quantum path selection in high-harmonic generation by a phase-locked two-color field. *Optics Express*, 16(25):20876, 2008.

[145] D. Shafir, Y. Mairesse, D. M. Villeneuve, P. B. Corkum, and N. Dudovich. Atomic wavefunctions probed through strong-field light–matter interaction. *Nature Physics*, 5(6):412–416, 2009.

[146] I. J. Kim, C. M. Kim, H. T. Kim, G. H. Lee, Y. S. Lee, J. Y. Park, D. J. Cho, and C. H. Nam. Highly efficient high-harmonic generation in an orthogonally polarized two-color laser field. *Physical Review Letters*, 94(24):243901, 2005.

[147] T. T. Liu, T. Kanai, T. Sekikawa, and S. Watanabe. Significant enhancement of high-order harmonics below 10 nm in a two-color laser field. *Physical Review A*, 73(6):063823, 2006.

[148] R. A. Ganeev, H. Singhal, P. A. Naik, I. A. Kulagin, P. V. Redkin, J. A. Chakera, M. Tayyab, R. A. Khan, and P. D. Gupta. Enhancement of high-order harmonic generation using a two-color pump in plasma plumes. *Physical Review A*, 80(3):033845, 2009.

[149] L. Brugnera, F. Frank, D. J. Hoffmann, R. Torres, T. Siegel, J. G. Underwood, E. Springate, C. Froud, E. I. C. Turcu, J. W. G. Tisch, and J. P. Marangos. Enhancement of high harmonics generated by field steering of electrons in a two-color orthogonally polarized laser field. *Optics Letters*, 35(23):3994–3996, 2010.

[150] S. D. C. Roscam Abbing, F. Campi, A. Zeltsi, P. Smorenburg, and P. M. Kraus. Divergence and efficiency optimization in polarization-controlled two-color high-harmonic generation. *Scientific Reports*, 11(1):24253, 2021.

[151] K. M. Dorney, L. Rego, N. J. Brooks, J. San Román, C.-T. Liao, J. L. Ellis, D. Zusin, C. Gentry, Q. L. Nguyen, J. M. Shaw, A. Picón, L. Plaja, H. C.

Kapteyn, M. M. Murnane, and C. Hernández-García. Controlling the polarization and vortex charge of attosecond high-harmonic beams via simultaneous spin–orbit momentum conservation. *Nature Photonics*, 13(2):123–130, 2019.

[152] D. Gauthier, P. R. Ribič, G. Adhikary, A. Camper, C. Chappuis, R. Cucini, L. F. DiMauro, G. Dovillaire, F. Frassetto, R. Géneaux, P. Miotti, L. Poletto, B. Ressel, C. Spezzani, M. Stupar, T. Ruchon, and G. De Ninno. Tunable orbital angular momentum in high-harmonic generation. *Nature Communications*, 8(1):14971, 2017.

[153] E. Mansten, J. M. Dahlström, P. Johnsson, M. Swoboda, A. L'Huillier, and J. Mauritsson. Spectral shaping of attosecond pulses using two-colour laser fields. *New Journal of Physics*, 10(8):083041, 2008.

[154] P. Wei, J. Miao, Z. Zeng, C. Li, X. Ge, R. Li, and Z. Xu. Selective enhancement of a single harmonic emission in a driving laser field with subcycle waveform control. *Physical Review Letters*, 110(23):233903, 2013.

[155] P. Wei, Q. Tian, Z. Zeng, J. Jiang, J. Miao, Y. Zheng, X. Ge, C. Li, R. Li, and Z. Xu. Efficient selection of a single harmonic emission using a multi-color laser field with an aperture-iris diaphragm. *Laser Physics*, 24(8):085302, 2014.

[156] S. Mitra, S. Biswas, J. Schötz, E. Pisanty, B. Förg, G. A. Kavuri, C. Burger, W. Okell, M. Högner, I. Pupeza, V. Pervak, M. Lewenstein, P. Wnuk, and M. F. Kling. Suppression of individual peaks in two-colour high harmonic generation. *Journal of Physics B: Atomic, Molecular and Optical Physics*, 53(13):134004, 2020.

[157] J. Mauritsson, P. Johnsson, E. Gustafsson, A. L'Huillier, K. J. Schafer, and M. B. Gaarde. Attosecond pulse trains generated using two color laser fields. *Physical Review Letters*, 97(1):013001, 2006.

[158] C. Jin, G. Wang, A.-T. Le, and C. D. Lin. Route to optimal generation of soft X-ray high harmonics with synthesized two-color laser pulses. *Scientific Reports*, 4(1):7067, 2014.

[159] C. Jin, G. Wang, H. Wei, A.-T. Le, and C. D. Lin. Waveforms for optimal sub-kev high-order harmonics with synthesized two- or three-colour laser fields. *Nature Communications*, 5(1):4003, 2014.

[160] C. G. Found. Ionization potentials of argon, nitrogen, carbon monoxide, helium, hydrogen and mercury and iodine vapors. *Physical Review*, 16(1):41–53, 1920.

[161] O. Raz, O. Pedatzur, B. D. Bruner, and N. Dudovich. Spectral caustics in attosecond science. *Nature Photonics*, 6(3):170–173, 2012.

[162] M. V. Berry and C. Upstill. Catastrophe optics: Morphologies of caustics and their diffraction patterns. 1980.

[163] Yu. A. Kravtsov and Yu. I. Orlov. *Caustics, Catastrophes and Wave Fields*. 1993.

[164] K. Schiessl, E. Persson, A. Scrinzi, and J. Burgdörfer. Enhancement of high-order harmonic generation by a two-color field: Influence of propagation effects. *Physical Review A*, 74(5):053412, 2006.

[165] Y. Chen, B. Li, X. Li, X. Tang, C. Zhang, and C. Jin. Effect of laser focus in two-color synthesized waveform on generation of soft X-ray high harmonics. *Chinese Physics B*, 32(1):014203, 2023.

[166] S. Stremoukhov. Role of gas pressure in quasi-phase matching in high harmonics driven by two-color laser field. *Atoms*, 11(7):103, 2023.

[167] H. Stark, C. Grebing, J. Buldt, A. Klenke, and J. Limpert. Divided-pulse nonlinear compression in a multipass cell. *Journal of Physics: Photonics*, 4(3):035001, 2022.

[168] M. Kaumanns, D. Kormin, T. Nubbemeyer, V. Pervak, and S. Karsch. Spectral broadening of 112 mJ, 1.3 ps pulses at 5 kHz in a LG_{10} multipass cell with compressibility to 37 fs. *Optics Letters*, 46(5):929, 2021.

[169] R. Klas. *Efficiency scaling of high harmonic generation using ultrashort fiber lasers*. PhD thesis, 2021.

[170] A. Dubrouil, Y. Mairesse, B. Fabre, D. Descamps, S. Petit, E. Mével, and E. Constant. Controlling high harmonics generation by spatial shaping of high-energy femtosecond beam. *Optics Letters*, 36(13):2486, 2011.

[171] D. J. Treacher, D. T. Lloyd, K. O'Keeffe, F. Wiegandt, and S. M. Hooker. Increasing the brightness of harmonic XUV radiation with spatially-tailored driver beams. *Journal of Optics*, 23(1):015502, 2021.

[172] D. Hoff, S. Mikaelsson, C. Guo, A.-K. Raab, A. L'Huillier, C. Arnold, and M. Gisselbrecht. Direct CEP stabilization of a high-repetition rate, few-cycle OPCPA chain with a single feedback loop, employing a stereo-ATI. In *Conference on Lasers and Electro-Optics*, 2022.

[173] D. J. Kane and R. Trebino. Single-shot measurement of the intensity and phase of an arbitrary ultrashort pulse by using frequency-resolved optical gating. *Optics Letters*, 18(10):823–825, 1993.

[174] D. Fabris, W. Holgado, F. Silva, T. Witting, J. W. G. Tisch, and H. Crespo. Single-shot implementation of dispersion-scan for the characterization of ultrashort laser pulses. *Optics Express*, 23(25):32803–32808, 2015.

[175] T. Zahavy, A. Dikopoltsev, D. Moss, G. I. Haham, O. Cohen, S. Mannor, and M. Segev. Deep learning reconstruction of ultrashort pulses. *Optica*, 5(5):666–673, 2018.

Acknowledgements

During the last four years I have learned a lot. But not only about MPCs and HHG, but also about what it means to do a PhD in such a nice environment. In addition to interesting research projects I also had a lot of fun and so I want to thank a few people.

Anne, thank you for the support, the encouragement to always aim high in all sorts of matter, all your honest and valuable feedback (especially for telling me when "enough" data were taken) and for always making time for me even during your busiest schedules in the last year. Cord, thanks for transferring a lot of excitement for optics onto me, for all the fun discussions and comments, and for always listening. Anne-Lise, thanks for being such a great guide for navigating a PhD and academia in general and especially for the amount of time you invested whenever there was a paper, a presentation, or a thesis to discuss.

Thanks to the whole 0.2 MHz lab for my first 1.5 PhD years. Chen, thanks for all the lab, workshop, and programming skills and tricks that I learned from you, for all of the coffee and water breaks, and for all the shenanigans surrounding finding and loosing the focus and wizards. Ivan, thanks for the adventures to FTF and the always high probabilité of a high qualité discussion about work-related and work-unrelated topics. Sara, thanks for explaining me so much over and over again when I just started my PhD. Daniel, thanks for making me a very proud master thesis supervisor, and of course, thanks for all the cookies! Dominik, thanks for learning a lot about laser stability and plumbing from you! Lucas, thanks for coming all the way from France to us to do your Bachelor thesis, it was great having you! Jan, even though we never had spatial overlap in Lund, thanks for all the remote help and advice regarding vacuum chambers!

When we started activities in the d-lab, I was a bit skeptical at first where this journey will lead, but this lab very quickly grew onto me. Johan, thanks for trusting me with your lab and letting me be creative. The suction-vacuum-chamber-lid-holders are now heavily in use. Emma, thank you for introducing me to bubbly water and

so many good stuffs, your magnificent fluffy beasts and all of the fun we had in and outside the lab. Marvin, thanks for the hiking adventures and I still have to think of you every time I see a lawn mower robot. Serhii, thanks for all the history facts and Eurovision discussions. Melvin, thanks for being so relatable sometimes, for always being the first one as soon as fun idea comes up, for keeping up some cleanness standards regarding programming (but also thanks for leaving the feedbacker untouched :)) and for sharing the joys and the pains of the interferometer. Victor, thanks for enhancing the Frenchness in this office! Yuman, thanks for all the laughter we shared on the way to lunch. Saga, thanks for all the great trips to DESY, Munich and Stockholm together! Gaspard, thanks for coming back to Lund! Mekan, it was great having you around!

Huge thanks also go to my fellow travel companions. Marius, thanks for broadening my taste in music in all life situations and for driving that car in the Philippines. David, thanks for enduring my cravings for all kinds of hipster beverages. Robin, thanks for all our discussions about chairs under water. Stefanos, thanks for always having a plan where to eat! Nedjma, Mattias and Venus, thanks for the great trip to Erice! Elisa, thanks for the fun times in Jeju! Miguel, I count the minigolf as "travel". David G, I also count the lunch breaks as "travel" as they usually went to strange topics but I enjoyed every minute of it! Johannes, thank you for taking me to feed the ducks, this was a very wholesome trip during a stressful week. Bibi, thanks for all the excursions one or two floors up/sideways!

I am also very grateful for all the collaborations with other places during the last four years, and I want to especially thank Marcus, Christoph, Arthur, Supriya, Esmerando, Nikita, Gunnar, Peter, Sylvianne, Miguel, Michi and Jonas.

Jörgen, Anne PJ, Maria, Åke, Emilie, Desiree, thank you all for handling the administration smoothly whenever I came to you with questions.

This PhD (and the road to it) would not have been possible without the support of my friends and family. Mama, Papa, Amelie, Gini, danke für all eure Unterstützung in den letzten 27 Jahren.

Felix, danke für alles.

Author contributions

Paper I: Multi-gigawatt peak power post-compression in a bulk multi-pass cell at a high repetition rate

In this paper, a compact bulk multi-pass cell experimental setup is presented. This setup allows post-compression of 300 fs pulses at 370 MW peak power from a Yb-rod amplifier to 31 fs, achieving 2.5 GW. A thorough characterization of the input and output pulses is performed, indicating that bulk multi-pass cells can be used to reach the multi-gigawatt regime without sacrificing beam quality.

I participated in the design of the setup. I took the lead role in building the setup, performing the measurements, analyzing the data and discussing the results, as well as writing the manuscript.

Paper II: Measurement of ultrashort laser pulses with a time-dependent polarization state using the d-scan technique

This paper presents an extension of the established dispersion-scan technique to not only recover the spectral phase, but also the time-dependent polarization state of an ultrashort pulse. The polarization d-scan was demonstrated for a polarization gate created with two waveplates at the output of a 6 fs long pulse of an OPCPA.

I supervised the master thesis that led to this publication. I took part in planning the experiments and calculations, participated in the measurements, data analysis and discussion, as well as manuscript writing.

Paper III: Single-shot, high-repetition rate carrier-envelope-phase detection of ultrashort laser pulses

This paper shows the carrier-envelope phase detection by optical Fourier transform in single-shot at 200 kHz.

I participated in the measurements and discussions. I helped to formulate the theoretical derivation of the method, participated in writing the supplemental document, and provided feedback to the main manuscript.

Paper IV: Highly versatile, two-color setup for high-order harmonic generation using spatial light modulators

This paper presents a waveform synthesizer for two-color HHG, optimized for best parameter control of the fundamental from a commercial Yb laser and its second harmonic. The setup employs spatial light modulators for both colors to shape the foci as well as to achieve sub-cyle relative phase control.

I took a leading role in the conceptualization of the experiment, building the setup, performing the measurements, analyzing the data, discussion of the results, and writing the manuscript.

Paper V: XUV yield optimization of two-color high-order harmonic generation in gases

In this paper the optimization of the flux for a specific extreme ultraviolet spectral range in two-color HHG is investigated. The relation between the optimum two-color phase and ratio, the total intensity, and the best flux for an energy range in the XUV spectrum is derived and experimentally confirmed.

I took a leading role in the conceptualization of the experiment, building the setup, performing the measurements, analyzing the data, discussion of the results, and writing the manuscript.

Paper VI: Compact, folded multi-pass cells for energy scaling of post-compression

In this paper a method for energy scaling for multi-pass cells is introduced. This method consists of folding the beam inside the multi-pass cell with a pair of plane mirrors multiple times, allowing for a compact experimental setup. A full spatio-

temporal characterization of the pulses is performed to check the validity and confirm the robustness of this technique.

I took a leading role in preparing, measuring and analyzing the spatio-temporal characterization measurements. I took part in discussion of these results and provided feedback to the main manuscript.